NASA-CR-195699

JOINT INSTITUTE FOR AERONAUTICS AND ACOUSTICS

IN-34-CR
876
124P

National Aeronautics and
Space Administration
Ames Research Center

JIAA TR - 111

Stanford University

A Method for the Modelling of Porous and Solid Wind Tunnel Walls in Computational Fluid Dynamics Codes

By

Thomas John Beutner

Stanford University
Department of Aeronautics and Astronautics
Stanford, CA 94305

December 1993

(NASA-CR-195699) A METHOD FOR THE MODELLING OF POROUS AND SOLID WIND TUNNEL WALLS IN COMPUTATIONAL FLUID DYNAMICS CODES (Stanford Univ.) 124 p

N94-28724

Unclas

G3/34 0000876

Acknowledgements

This research has been supported by a grant (NCC 255) from NASA Ames Research Center. Support has also been provided by the U.S. Air Force Palace Knight Program.

Abstract

Porous wall wind tunnels have been used for several decades and have proven effective in reducing wall interference effects in both low speed and transonic testing. They allow for testing through Mach 1, reduce blockage effects and reduce shock wave reflections in the test section. Their usefulness in developing computational fluid dynamics (CFD) codes has been limited, however, by the difficulties associated with modelling the effect of a porous wall in CFD codes. Previous approaches to modelling porous wall effects have depended either upon a simplified linear boundary condition, which has proven inadequate, or upon detailed measurements of the normal velocity near the wall, which require extensive wind tunnel time.

The current work was initiated in an effort to find a simple, accurate method of modelling a porous wall boundary condition in CFD codes. The development of such a method would allow data from porous wall wind tunnels to be used more readily in validating CFD codes. This would be beneficial when transonic validations are desired, or when large models are used to achieve high Reynolds numbers in testing.

A computational and experimental study was undertaken to investigate a new method of modelling solid and porous wall boundary conditions in CFD codes. The method utilized experimental measurements at the walls to develop a flow field solution based on the method of singularities. This flow field solution was then imposed as a pressure boundary condition in a CFD simulation of the internal flow field. The effectiveness of this method in describing the effect of porosity changes on the wall was investigated. Also, the effectiveness of this method when only sparse experimental measurements were available has been investigated. The current work demonstrated this approach for low speed flows and compared the results with experimental data obtained from a heavily instrumented variable porosity test section.

The approach developed was simple, computationally inexpensive, and did not require extensive or intrusive measurements of the boundary conditions during the wind tunnel test. It may be applied to both solid and porous wall wind tunnel tests.

Table of Contents

List of Figures

List of Tables

Nomenclature

c	airfoil chord
C_p	pressure coefficient
$C_{p_{Plenum}}$	plenum pressure coefficient
h	wind tunnel test section height
m	line source strength
M	Mach number
n	outward normal coordinate direction
p	pressure
p_∞	freestream pressure
P	porosity parameter
P_L	porosity of lower wall
P_S	porosity of side wall
P_U	porosity of upper wall
U_∞	freestream velocity
u, v	two-dimensional Cartesian velocity components; u is streamwise component, v is vertical component
u,v,w	three-dimensional Cartesian velocity components; u is streamwise component, v is spanwise component, w is vertical component
W	tunnel width complex velocity function
V_o	empty tunnel normal velocity at walls
x, y	two-dimensional Cartesian coordinates, origin at airfoil leading edge (α=0), x is the streamwise coordinate, y is the vertical coordinate
x, y, z	three-dimensional Cartesian coordinates, origin at wing root leading edge (α=0), x is the streamwise coordinate, y is the spanwise coordinate, z is the vertical coordinate

x_o, y_o	origin of Cartesian coordinates
y_o	semispan of three-dimensional singularity
α	angle of attack
β	$\sqrt{1 - M^2}$
$\tilde{\beta}$	artificial compressibility parameter
ϕ	perturbation velocity potential
ϕ_S	potential due to a line source
ϕ_V	potential due to a horseshoe vortex
ϕ_γ	potential due to a point vortex
ϕ_μ	potential due to a point x-doublet
ϕ_σ	potential due to a point source
ϕ_ω	potential due to a point y-doublet
γ	two-dimensional vortex singularity strength
Γ	horseshoe vortex strength
μ	two-dimensional x-doublet singularity strength
σ	two-dimensional source singularity strength
ω	two-dimensional y-doublet singularity strength

Chapter 1

Introduction

1.1 Background

Ventilated wall wind tunnels have been in use for several decades and have been useful in reducing wall interference effects at subsonic and transonic speeds and allowing for testing through Mach 1. A series of improvements have been made to the earliest ventilated wind tunnels leading to modern porous wall test sections. The usefulness of porous wall wind tunnels for computational fluid dynamics (CFD) validation efforts has been limited, however, by difficulties associated with modelling the porous wall boundary condition.

It has long been recognized that the corrections to wind tunnel data for open and closed test sections were of opposite signs [1]. Furthermore, in transonic testing, shock waves which impinge on a solid boundary are reflected as shock waves, whereas shocks which impinge on a free air boundary in an open jet test section are reflected as expansion waves. Theodorsen suggested that a wind tunnel might be constructed which would reduce wind tunnel wall interference by using a partially open boundary condition in which one, two or three walls would be removed from a solid wall test section [2]. Wright and Ward tested one of the first successful ventilated wall wind tunnels which used several streamwise slots in the tunnel walls [3]. They found that blockage interference was reduced with this wind tunnel. In addition, they found that ventilated walls alleviated choking problems at transonic speeds and permitted testing through

Mach 1. These two effects have led to ventilated wall test sections being used for both low speed and transonic work [4]. The work by Wright and Ward led to other ventilated wind tunnels, also using streamwise slots to ventilate the test section walls. It was soon realized, however, that streamwise slots allowed for the reflection of shock and expansion waves from the walls. These reflected waves could impinge on the model and result in data which was uncorrectable [5].

Porous wall tunnels alleviated this problem by significantly reducing the shock reflections from the walls [6]. The porous wall was constructed with a pattern of small, discrete holes in the wall. The differential resistance wall was a further refinement to the porous wall concept, using holes with axes inclined to the normal. The differential resistance wall was found to provide cancellation of both shock and expansion waves and allowed for inflow and outflow resistance of the wall to be balanced [1].

1.2 Motivation for Modelling the Porous Wall Boundary Condition

As high speed computers have increased the flexibility and capability of computational modelling of flow fields, a new emphasis has been placed on obtaining wind tunnel data which may be used to calibrate and validate computational fluid dynamics (CFD) codes [7]. Increasingly, there has been a trend toward modelling entire wind tunnel flow fields, including support struts and wind tunnel walls [8, 9]. This has led to an increased use of solid wall wind tunnels in transonic testing. The simplicity of modelling a solid wall boundary condition has made their use attractive despite the disadvantages of substantial wall interference [10].

Porous wall wind tunnels have long been used for both low speed and transonic wind tunnel testing because of their desirable effect of reducing wind tunnel wall interference. With mounting evidence of the importance of Reynolds number on flap gap sizing and maximum lift predictions [11, 12], the need for performing high Reynolds number tests to validate CFD codes which will be used in the design process is of growing importance. While a solid wall wind tunnel may be used for such tests, wall interference can become a limiting factor on the size of models.

In general, for test sections of identical dimensions, a porous wall wind tunnel will allow testing of larger models at transonic speeds without shock reflections from the tunnel walls impinging on the model. In addition, porous walls may eliminate shock boundary layer interactions on the walls and reduce such interactions on the model by eliminating reflected shocks from the walls. Thus, the use of porous wall data in CFD validation may reduce the grid refinement required near the wind tunnel walls while providing a more realistic assessment of the applicability of a turbulence model to free air calculations. Ultimately, the goal of many CFD validation efforts is to develop CFD codes which are capable of predicting free air performance. These codes may be useful for design purposes even if they are not sophisticated enough to resolve multiple shock boundary layer interactions which may be associated with shock reflections from solid wall wind tunnels.

Some attempts have been made to model discrete slots in CFD codes either by modelling the slots in an approximate manner or by solving coupled equations to describe the boundary condition [13, 14]. However, porous wall wind tunnels have been shown to be superior to slotted walls at cancelling shock wave reflections [6]. Porous walls pose a problem in CFD validations, however, since the modelling of the wall boundary is more difficult for a porous wall wind tunnel.

The intricacies of the porous wall make it prohibitive to depict the actual wall geometry in a viscous CFD grid. Since the porous wall wind tunnel may have several thousand holes on the walls, modelling the individual holes and the viscous effects associated with each hole in a CFD grid is not possible given the current limitations on computer speed and memory. Thus, the effect of the porous walls must be dealt with either by correcting the test data to free air conditions, or by modelling the porous wall by appropriate means in the CFD code.

1.3 Previous Approaches to Modelling Porous Walls

Numerous approaches for correcting porous wall data to free air conditions have been proposed. These methods use a variety of approaches, based on model pressure and force measurements [15], wall boundary pressure or velocity measurements, or pressure rail measurements [4, 16]. These methods generally produce a global correction to the velocity and angle of attack, based on classical reflection techniques [1]. The test data is then taken to be equivalent to data from a test in free air at the corrected angle of attack and velocity. Additional corrections to drag and moment coefficients and Mach number are sometimes included [1]. This results in a useful comparison of bulk flow measurements, such as lift and drag coefficients. However, these methods are of limited use in performing CFD validations and calibrations because they have the effect of altering the entire flow field. When performing CFD validations, it is desirable to compare as much of the flow field as possible [7].

Other approaches have sought to develop a boundary condition which may be used at the porous wall boundary in the CFD code. These methods have depended on either a simple, universal boundary condition, [1, 6] or on detailed measurements of the boundary conditions during the wind tunnel test which are then imposed as boundary conditions in the CFD code [17-21].

A universal boundary condition has proven difficult to determine experimentally, and to implement computationally. The porosity parameter contained in such a boundary condition can only be determined by extensive dedicated testing. In addition, this parameter may be different for otherwise identical top and bottom walls, and it may depend on Mach number, stagnation pressure, model size and orientation [22]. Additionally, such a boundary condition may be destabilizing in CFD codes and can actually prevent convergence [23, 24].

Most current efforts in ventilated wall interference research have been directed toward making detailed measurements of velocity or pressure in the wind tunnel and using these to develop a boundary condition in CFD codes. The approach used by King and Johnson in modelling a slotted wall boundary condition was to use a rail suspended midway between the model and the tunnel wall to make pressure measurements at every point in the flow corresponding to a boundary point in the CFD code [17]. Later, to allow for additional grid refinement, a spline fit was made to this data as a means of interpolating pressure measurements [18]. This approach required extensive measurements of the pressure on planes away from the wall and has not been extended to three dimensions.

Jacocks used detailed measurements of static pressure, normal velocity adjacent to the wall and boundary layer thickness at the wall to develop an equivalent inviscid normal velocity profile based on boundary layer integration along the wall [19]. Crites and Rueger extended this method for limited three-dimensional problems by using extensive pressure measurements on the walls and extensive calibrations of the tunnel walls to estimate the normal velocity through the porous wall and, again, develop an equivalent inviscid normal velocity profile. This profile was then used as a boundary condition in numerical solvers for the purpose of developing incremental corrections to wind tunnel data [20, 21]. These approaches required detailed measurements of the wall boundary conditions and large amounts of dedicated test time for calibration at each plenum pressure, Mach number and Reynolds number, making them costly in practice. In most practical cases, the extensive measurements and calibrations required at each test condition have limited these techniques to two-dimensional flows.

1.4 Current Approach

The approach presented here represents an attempt to describe the effects of a porous wall in a CFD code based on sparse measurements of the flow field in the wind tunnel. The usefulness of this theory has been demonstrated by carrying out wind tunnel experiments in a heavily instrumented, low speed ($M \cong .07$) research wind tunnel and performing CFD simulations of the experiments. This test section utilized variable porosity walls and allowed for extensive pressure and velocity measurements to be made near the boundaries of the test section.

The theoretical approach to describing the porous wall boundary utilized the classical porous wall boundary condition as a means of interpolating and extrapolating boundary conditions measured during wind tunnel tests. A solution for the flow near the walls, based on the method of singularities, was developed using pressure measurements made on the walls during wind tunnel tests. The singularity expressions used in this method satisfied the classical porous wall boundary condition. The method of singularities solution was then used to specify the pressure at CFD boundary point locations.

The current work extended the classical method of singularities by including higher order singularities. The current work also differs from classical approaches in that it attempted to model the boundary condition in the CFD code, rather than applying corrections to the data based on measurements of the boundary condition. Furthermore, unlike some limited previous attempts at modelling the boundary condition, the current work utilized experimental pressure measurements on the walls and used classical porous wall theory to extend the measurements. This approach did not require extensive calibrations of the wind tunnel walls, and used static pressure measurements on the walls, which may be obtained rapidly during wind tunnel tests.

In two dimensions, this approach was developed using analytic expressions for the singularity strengths. In three dimensions, a numerical solution was required to determine the pressure profiles induced by singularities in the presence of the porous wall boundary condition. Once obtained, however, these numerical solutions may be used for multiple tests.

The current work consisted primarily of two-dimensional, low speed studies. Experimental work was conducted in the Stanford Low Speed Wind Tunnel and computational studies were performed using an incompressible flow solver. Although the Mach number range of the research tunnel used for this work was very low, some consideration was given to the implementation of this method for higher speed flows. Limited consideration was also given to the extension of this method to three-dimensional flows.

Chapter 2

Porous Wall Theory

2.1 Introduction

One of the major advantages of porous wall wind tunnels is their ability to reduce or eliminate shock wave reflections in transonic testing. In addition, they have the effect of reducing wall interference for low speed flows, making them useful for cases where substantial wall interference is expected in low speed testing [25]. Classical approaches to correcting data from porous wall wind tunnels are slowly being replaced by efforts aimed at modelling the porous wall boundary condition in CFD codes.

2.2 Development of Classical Porous Wall Boundary Condition in Two Dimensions

It has widely been assumed that the flow through the porous walls is basically viscous in nature. This has led to a simple theory, based on an analogy to pipe flow, for describing the porous wall boundary condition [1, 6]. This boundary condition assumes that the airfoil perturbations are sufficiently small near the walls so that linearization applies up to high subsonic Mach numbers near the walls. An implicit restriction of this theory is that the flow at the walls must be subsonic. In practice, however, flow near the walls has been found to be subcritical at freestream Mach numbers up to .9, lift coefficients as high as 1.5 and a height to chord ratio of 4 [26].

Classical porous wall theory [1] typically uses a point source, point vortex, and point source and vortex doublets to describe the free-air flow past a lifting airfoil, as given in Equation 2.1.

$$\phi_F = \phi_\sigma + \phi_\gamma + \phi_\mu + \phi_\omega \tag{2.1}$$

where:

$$\phi_\sigma = \frac{\sigma}{2\pi\beta} \ln\sqrt{x^2 + (\beta y)^2} \tag{2.2}$$

$$\phi_\gamma = -\frac{\gamma}{2\pi} \operatorname{a\,tan}\frac{\beta y}{x} \tag{2.3}$$

$$\phi_\mu = \frac{\mu}{2\pi\beta} \frac{x}{x^2 + (\beta y)^2} \tag{2.4}$$

$$\phi_\omega = \frac{\omega}{2\pi} \frac{\beta y}{x^2 + (\beta y)^2} \tag{2.5}$$

Note that Equations 2.4 and 2.5 may be interpreted as first derivatives with respect to x of Equations 2.2 and 2.3, respectively.

The potential ϕ_F is a solution of the linearized potential equation:

$$\beta^2 \frac{\partial^2 \phi_F}{\partial x^2} + \frac{\partial^2 \phi_F}{\partial y^2} = 0 \tag{2.6}$$

except at the origin ($x = y = 0$), where ϕ_F is singular. In addition,

$$\frac{\partial \phi_F}{\partial x}, \frac{\partial \phi_F}{\partial y} \to 0 \text{ as } r = \sqrt{x^2 + (\beta y)^2} \to \infty \tag{2.7}$$

An interference potential, ϕ_W, which accounts for the interference caused by the presence of the walls must be solved for. Again, in the region between the walls, $\left(-\frac{h}{2} < y < \frac{h}{2}\right)$, ϕ_W must also satisfy the linearized potential equation:

$$\beta^2 \frac{\partial^2 \phi_W}{\partial x^2} + \frac{\partial^2 \phi_W}{\partial y^2} = 0 \tag{2.8}$$

The free air potential and interference potential together form the potential function ϕ:

$$\phi = \phi_F + \phi_W \tag{2.9}$$

which is required to satisfy the following boundary conditions:

$$P_U \frac{\partial \phi}{\partial x} + \frac{\partial \phi}{\partial y} = 0 \quad \text{at } y = \frac{h}{2} \tag{2.10}$$

$$P_L \frac{\partial \phi}{\partial x} - \frac{\partial \phi}{\partial y} = 0 \quad \text{at } y = -\frac{h}{2} \tag{2.11}$$

The basis for these boundary conditions is easily seen. The x-axis is aligned with the freestream flow in the wind tunnel so that $\frac{\partial \phi}{\partial y} = v$, and $\frac{\partial \phi}{\partial x} = u$. According to linearized small perturbation theory, u should be proportional to the difference between free stream and local pressure. If the plenum is maintained at freestream static pressure, this will also be the pressure difference across the wall. Based on an analogy to pipe flow, the velocity normal to the wall, v, should be proportional to the pressure difference existing across the wall. The constant of proportionality is the porosity parameter, P_U for the upper wall and P_L for the lower wall. Different porosity parameters may be used for the upper and lower walls since the flow through the two walls is different in character. In the case of the upper wall, there is a suction over most of the wall resulting in flow into the test section. This flow comes from the plenum where the flow is essentially at rest. For the lower wall, there is an increased pressure, resulting in flow out of the test section. This flow has considerable streamwise momentum. The result is that flow through the lower wall often separates within the holes in the wall [1, 20]. Thus, identical upper and lower walls may offer differing resistance to flow through the walls. In part, this may be compensated for by inclining the holes in the wall at an angle with respect to the normal direction. The different porosity parameters specified on each wall offer another means of accounting for this difference.

Analytic expressions for the velocities induced by simple singularities in the presence of the boundary conditions of Equations 2.10 and 2.11 have been developed [1, 27] and are summarized here.

The wind tunnel coordinates are nondimensionalized as,

$$X = \frac{x}{\beta h} \qquad Y = \frac{y}{h} \tag{2.12}$$

and the complex position function Z is defined as,

$$Z = X + iY \tag{2.13}$$

and the complex velocity notation is defined as,

$$W_F = \frac{\partial \phi_F}{\partial X} - i\frac{\partial \phi_F}{\partial Y} \tag{2.14}$$

$$W_W = \frac{\partial \phi_W}{\partial X} - i\frac{\partial \phi_W}{\partial Y} \tag{2.15}$$

$$W = W_W + W_F = \frac{\partial \phi}{\partial X} - i\frac{\partial \phi}{\partial Y} \tag{2.16}$$

With the form of the free-air potential due to a singularity known, it remains to determine the form of the complex velocity function W_W.

The complex velocity funtion W_W may be found by the method of images. The approach of Reference 1, which is followed here, determines the interference potential arising from a singularity placed between two infinite boundaries described by Equations 2.10 and 2.11. As this approach may be found in detail in the literature [1, 27], only the result will be shown here.

Considering the potential flow due to singularities in the presence of an infinite porous wall boundary condition as described by Equations 2.10 and 2.11, it may be shown that the complex velocity functions for a source, W_σ, and a vortex, W_γ, are:

$$W_\sigma = \frac{\sigma}{\beta}\left[\,(B+E) + \chi(P_U)\chi(P_L)\,\right] \tag{2.17}$$

$$W_\gamma = i\gamma(B - E) \tag{2.18}$$

where:

$$B = \frac{1}{2}\,\frac{e^{\pi\frac{t_U+t_L}{2}(Z-Z_0)}}{e^{\pi(Z-Z_0)}-1} \qquad 0<\frac{t_U+t_L}{2}<1 \tag{2.19}$$

$$E = -\frac{1}{2}\,\frac{e^{\pi\frac{t_U+t_L}{2}(Z-\overline{Z}_0)}}{e^{\pi(Z-\overline{Z}_0)}+1}\,e^{i\pi\frac{t_U-t_L}{2}} \qquad 0<\frac{t_U+t_L}{2}<1 \tag{2.20}$$

$$\chi(P_U)\chi(P_L) = \begin{cases} 1 & P_U = P_L = 0 \\ 0 & \text{Otherwise} \end{cases} \tag{2.21}$$

$$t_U = \frac{2}{\pi}\operatorname{A}\tan\left(\frac{P_U}{\beta}\right) \quad \text{and} \quad t_L = \frac{2}{\pi}\operatorname{A}\tan\left(\frac{P_L}{\beta}\right) \qquad 0 \le t_{U,L} < 1 \tag{2.22}$$

Velocity Functions for source and vortex doublets in the presence of infinite porous walls may be obtained by differentiation of the above formulas:

$$W_\mu = \frac{\mu}{\beta^2\ h}\,\frac{d}{dZ}\,(B+E) \tag{2.23}$$

$$W_\omega = \frac{\omega\ i}{\beta\ h}\,\frac{d}{dZ}\,(B-E) \tag{2.24}$$

Higher derivatives of the source and vortex may also be taken if additional singularities are desired. In this work, up to the fourth derivatives of the source and vortex were retained in the singularity expansions.

It is noteworthy that the velocities induced by a source in this formulation are discontinuous at P=0 (see Equations 2.17 and 2.21). Classical wind tunnel interference corrections model the wall interference using infinite strip theory. This approach develops corrections based on linear theory solutions for simple singularities in the presence of two infinite walls. When these walls are solid, the mass introduced by the source must exit either upstream ($x = -\infty$) or downstream ($x = +\infty$.) Generally, a bias is introduced into the velocity functions in order to force the velocity disturbance to go to zero at $x = -\infty$ (see Equation 2.21), but the influence of the source far downstream remains non-zero. However, for a porous wall, no matter how small the porosity, the mass contribution from the source may leak out through the walls. Thus, for an infinite porous wall, the velocity contribution from a source will go to zero at both $x = -\infty$ and $x = +\infty$. This discontinuity is well known [28]. The use of infinite strip theory introduces finite test section errors [29], but it is still common in practice as an engineering approximation. The effects of the discontinuity at P=0 caused by the infinite strip theory will be considered further in Chapter 5. The velocity profile on the wind tunnel inflow plane and the presence of a breather section at the outflow plane also introduce finite test section effects. In this work, singularity solutions were developed using infinite strip theory. Finite test section effects associated with the inflow and outflow plane were minimized by specifying boundary conditions based on experimental measurements on these planes. A velocity profile, based on five-hole probe measurements was specified on the inflow plane and a constant pressure was specified at the breather location.

2.3 Methods of Describing the Effect of a Porous Wall in CFD Codes

Classical porous wall theory has been widely used to apply corrections to the measured wind tunnel data based on the interference potential ϕ_W. The use of such corrections is undesirable for CFD validations, however, because they alter the entire flow field in order to impose a correction which is valid at only one point. Recent efforts in CFD validations have attempted to model wall boundary conditions directly in the computations. For a solid wall wind tunnel test, this may be accomplished by specifying either a slip (inviscid) boundary condition at the edge of the boundary layer, or a no-slip (viscous) boundary condition at the location of the walls. For a porous wall, however, the complexity of the wall geometry does not allow for the wall to be modelled exactly given the current limitations on computer memory and speed.

Some attempts have been made to use the boundary conditions of Equations 2.10 and 2.11 directly in CFD calculations. This approach is questionable for three reasons. First, there is not a good theoretical approach for determining the value of the porosity parameter contained in these equations and so the porosity parameter must be determined from experimental data [1]. Second, there is experimental evidence that the linear relationship between perturbation velocities implied by Equations 2.10 and 2.11 do not apply over the entire wall [19]. Third, and most important, the application of Equations 2.10 and 2.11 as boundary conditions in CFD codes is destabilizing and can actually prevent convergence [23, 24]. Still, classical porous wall theory does provide some insight into the nature of the flow near a porous wall.

Some attempts have also been made to model a porous wall boundary condition by specifying a normal velocity profile on the walls. The normal velocity profile developed in these approaches is an equivalent inviscid normal velocity profile based on an integral boundary layer analysis. This analysis requires a knowledge of the normal velocity at the wall surface. These approaches have been successful in describing the effects of a porous wall, but their application has been limited by the extreme requirements for wind tunnel calibrations and measurements during tests. These approaches require either detailed normal velocity measurements near the wall during a test or detailed pressure measurements on the wall coupled with extensive calibrations of the wind tunnel walls in order to determine the relationship between pressure differences across the wall and velocities induced through the wall [19, 20, 21]. The calibrations must be performed at every Mach number and Reynolds number which will be used during testing and they require an adjustable pressure plenum. Either implementation of this approach requires extensive wind tunnel tests for the purpose of determining boundary conditions. Furthermore, the integral methods used depend upon very detailed measurements during the test, limiting the facilities in which they may be used. While some attempts have been made to apply these procedures to simple three-dimensional cases, their usefulness is limited by test facility requirements.

2.4 Theoretical Approach of the Present Work

The approach used for modelling the porous wall boundary condition in this research was to make use of classical porous wall theory as a means of interpolating and extrapolating limited experimental measurements of the pressure on the porous walls.

In this work, the classical porous wall boundary condition of Equations 2.10 and 2.11 was used to develop pressure profiles on the walls using the method of singularities. The singularity solutions were developed as discussed in Section 2.2. Singularity strengths were determined based on least squares matching of velocity profiles inferred from pressure measurements made on the walls. The resulting method of singularities solution was then used to specify a pressure boundary condition in the CFD code. Thus, flow field corrections were eliminated in preference to a means of specifying experimental boundary conditions in the CFD simulation. Furthermore, by using singularity solutions based on the classical porous wall boundary condition, experimental data could be interpolated and extrapolated over the length of the walls.

Classical two-dimensional porous wall theory typically uses four singularities (a source, a vortex, a source doublet and a vortex doublet) to develop corrections to the flow field. The current approach extended classical theory by using as many as ten singularities. These singularities included a source, a vortex, and first, second, third and fourth derivatives of the source and vortex in the streamwise direction. Furthermore, in the current apporach, no corrections were applied to the wind tunnel data. Instead, the pressure profile existing on the walls during the experiments was modelled in the CFD code. In addition, classical porous wall boundary conditions were used only to develop the singularity solutions, and were not applied directly in the CFD code. In this work, the porosity parameter was found by minimizing the root-mean-square errors in matching pressure coefficient measurements on the walls.

2.5 Extension to Three Dimensions

Extension of this approach to three dimensions requires a panel method, or other numerical solver, to determine three-dimensional singularity solutions in the presence of a porous wall boundary condition. Again, as in the two-dimensional case, simple singularities and their derivatives may be used. In this work, a line source of span $2y_0$,

$$\phi_S = \frac{m}{4\pi} \ln\left[\frac{\beta(y-y_0)+\sqrt{x^2+\beta^2(y-y_0)^2+(\beta z)^2}}{\beta(y+y_0)+\sqrt{x^2+\beta^2(y+y_0)^2+(\beta z)^2}}\right] \tag{2.25}$$

and horseshoe vortex of span $2y_0$,

$$\begin{aligned}\phi_v = \frac{\Gamma}{4\pi}\Bigg[&\mathrm{A}\tan\left(\frac{(y+y_0)}{z}\right) - \mathrm{A}\tan\left(\frac{(y-y_0)}{z}\right)\\ &+\mathrm{A}\tan\left(\frac{x(y+y_0)}{z\left(x^2+\beta^2(y+y_0)^2+\beta^2z^2\right)^{1/2}}\right) - \mathrm{A}\tan\left(\frac{x(y-y_0)}{z\left(x^2+\beta^2(y-y_0)^2+\beta^2z^2\right)^{1/2}}\right)\Bigg]\end{aligned} \tag{2.26}$$

along with the first, second and third derivatives with respect to x of the line source and horseshoe vortex, the first, second and third derivatives with respect to y_0 of the line source and horseshoe vortex, and a first derivative with respect to z of the horseshoe vortex were used to develop the method of singularities solution. A uniform freestream term was also included in each case as a means of biasing the source term. In Equations 2.25 and 2.26 above, x is the Cartesian coordinate in the streamwise direction, y is the Cartesian coordinate in the spanwise direction, and z is the Cartesian coordinate in the vertical direction. The singularities are located at $x = 0$, $z = 0$, and centered about $y = 0$. They have a span of $2y_0$.

The panel method used constant strength doublet panels to model the wind tunnel walls [30]. The walls were modelled over 24 chord lengths. Geometric stretching of the panels in the streamwise direction was used to allow for better resolution of the solution near the location of the model. A total of 384 panels were used to model each of the four walls. Inflow and outflow planes were not panelled. This approach, which models only a finite portion of the walls rather than treating them as infinite, results in continuous behaviour at P = 0. Figure 1 shows the arrangement of panels on the walls. In Figure 1, as in Equations 2.25 and 2.26, the singularities are located at x = 0, z = 0 and centered at y = 0. The span of the singularities was equal to the wing span. A simple shift in the coordinate system may be used to place the singularities at any streamwise location desired. For the calculation of singularity strengths based on least squares matches to experimental data, the singularities were shifted to the quarter-chord location on the wing.

For three-dimensional testing, the boundary conditions analogous to Equations 2.10 and 2.11 are:

$$P_U \frac{\partial\phi}{\partial x} + \frac{\partial\phi}{\partial z} = 0 \qquad \text{at} \qquad z = \frac{h}{2} \tag{2.27}$$

$$P_L \frac{\partial\phi}{\partial x} - \frac{\partial\phi}{\partial z} = 0 \qquad \text{at} \qquad z = -\frac{h}{2} \tag{2.28}$$

$$P_S \frac{\partial\phi}{\partial x} + \frac{\partial\phi}{\partial y} = 0 \qquad \text{at} \qquad y=W \tag{2.29}$$

In the case of full-span testing, an additional boundary condition of the form of Equation 2.29 may be imposed on the remaining wall. In the case of half-span testing, as in this work, the remaining side wall is a plane of symmetry. The boundary conditions of Equations 2.27-2.29 were enforced at control points located at the center of each panel. Bicubic spline fits were used to interpolate solutions between control points on the panels.

Chapter 3

Two-Dimensional Governing Equations and Navier-Stokes Solver

3.1 Introduction

For numerical simulation of the wind tunnel tests performed in the Stanford Low Speed Wind Tunnel, an incompressible Navier-Stokes solver (INS2D) was used [31]. Although methods of describing porous walls in CFD codes are of primary interest for transonic codes, an incompressible code was used in this case because of the very low Mach number of the tests conducted in this research tunnel. The method described in this and the previous chapter may also be used with transonic flow solvers [32].

3.2 Governing Equations

The equations presented here have been nondimensionalized as follows:

$$\tilde{u}_i = \frac{u_i}{u_{ref}} \qquad \tilde{x}_i = \frac{x_i}{x_{ref}} \qquad \tilde{t} = \frac{t u_{ref}}{x_{ref}} \qquad \tilde{p} = \frac{p - p_{ref}}{\rho u_{ref}^2}$$

$$\tilde{\tau}_{ij} = \frac{\tau_{ij}}{\rho u_{ref}^2} \qquad \tilde{\nu} = \frac{\nu}{x_{ref} u_{ref}} = Re^{-1} \tag{3.1}$$

where the ~ superscript denotes nondimensional quantities. Hereafter, the ~ superscript will be dropped for convenience.

In the above equations, $u_i = u$ or v, the Cartesian velocity components for $i = 1, 2$, respectively and $x_i = x$ or y, the Cartesian spatial coordinates for $i = 1, 2$, respectively. The pressure, density and kinematic viscosity are denoted by p, ρ, and ν, respectively. The subscript $_{ref}$ denotes reference quantities; u_{ref} is the measured freestream velocity upstream of the model, x_{ref} is taken as the airfoil chord.

The Navier-Stokes equations for incompressible, two-dimensional, constant density flow may then be written in conservative form as follows:

$$\frac{\partial u}{\partial x}+\frac{\partial v}{\partial y}=0 \qquad (3.2)$$

$$\frac{\partial \bar{u}}{\partial t}+\frac{\partial}{\partial x}(e-e_v)+\frac{\partial}{\partial y}(f-f_v)=0 \qquad (3.3)$$

where:

$$\bar{u}=\begin{bmatrix} u \\ v \end{bmatrix} \qquad (3.4)$$

$$e=\begin{bmatrix} u^2+p \\ uv \end{bmatrix} \quad f=\begin{bmatrix} vu \\ v^2+p \end{bmatrix} \qquad (3.5)$$

$$e_v=\begin{bmatrix} \tau_{xx} \\ \tau_{xy} \end{bmatrix} \quad f_v=\begin{bmatrix} \tau_{yx} \\ \tau_{yy} \end{bmatrix} \qquad (3.6)$$

For turbulent flows, these equations represent Reynolds averaged quantities. The Boussinesq approximation is used for the Reynolds stress. The viscous stress tensor may then be written as:

$$\tau_{ij}=(\nu+\nu_t)\left(\frac{\partial u_i}{\partial x_j}+\frac{\partial u_j}{\partial x_i}\right) \qquad (3.7)$$

where ν_t is the turbulent eddy viscosity.

As the thrust of this work is the development of a methodology for describing porous wall boundary conditions in CFD codes, the details of the CFD code and turbulence modelling will not be discussed here. A brief description of the CFD code is included in the following sections. Additional details about the CFD code may be seen in References 31 and 33. The results shown from the INS2D code used a Baldwin-Barth turbulence model. The Baldwin-Barth turbulence model is in wide use in a variety of

CFD codes currently. Additional details about this turbulence model may be seen in Reference 34.

3.3 Numerical Solver

The INS2D code uses a primitive variable formulation of the incompressible Navier-Stokes equations. In the primitive variable formulation, the equations are written with pressure and velocity as the dependent variables.

The equations are transformed into generalized coordinates using the transformations:

$$\begin{aligned} \xi &= \xi(x, y, t) \\ \eta &= \eta(x, y, t) \end{aligned} \tag{3.8}$$

The system of equations then becomes:

$$\frac{\partial}{\partial \xi}\left(\frac{U}{J}\right) + \frac{\partial}{\partial \eta}\left(\frac{V}{J}\right) = 0 \tag{3.9}$$

$$\frac{\partial \hat{u}}{\partial t} = - \frac{\partial}{\partial \xi}(\hat{e} - \hat{e}_v) - \frac{\partial}{\partial \eta}(\hat{f} - \hat{f}_v) \tag{3.10}$$

where J is the Jacobian of the transformation and:

$$\hat{u} = \frac{1}{J}\begin{bmatrix} u \\ v \end{bmatrix} \tag{3.11}$$

$$\hat{e} = \frac{1}{J}\begin{bmatrix} \xi_x p + uU + \xi_t u \\ \xi_y p + vU + \xi_t v \end{bmatrix} \qquad \hat{f} = \frac{1}{J}\begin{bmatrix} \eta_x p + uV + \eta_t u \\ \eta_y p + vV + \eta_t v \end{bmatrix} \tag{3.12}$$

The contravariant velocity components, U and V are given by:

$$U = \xi_x u + \xi_y v \qquad V = \eta_x u + \eta_y v \tag{3.13}$$

The metrics of the transformation are represented with subscript notation as, for example:

$$\xi_x = \frac{\partial \xi}{\partial x}$$

The INS2D code uses an artificial compressibility approach for solving the incompressible Navier-Stokes Equations [31, 35]. In this approach, a time derivative of pressure is added to the continuity equation (Equation 3.9) and an artificial compressibility factor, $\tilde{\beta}$, is introduced:

$$\frac{\partial p}{\partial \tau} = -\tilde{\beta}(\nabla \cdot \hat{u}) \tag{3.14}$$

This results in a hyperbolic system of equations. This system may then be marched to a steady-state solution in pseudo-time. The right hand side of Equation 3.10 and the divergence of the velocity field approach zero as the solution approaches steady-state.

This hyperbolic system of equations also has artificial pressure waves which are finite in speed. Therefore, compressible flow algorithms may be used for solving the system of equations. The INS2D code uses third order accurate, locally upwind differencing of the convective fluxes and second order accurate central differencing of the viscous terms. The upwind differencing is biased by the signs of the eigenvalues of the local flux Jacobian, following the method of Roe [36]. The set of numerical equations is solved using a Gauss-Seidel type line relaxation scheme.

All computations were performed on the CRAY Y-MP computer at NASA Ames Research Center. Solutions typically converged in approximately 1500 iterations, requiring approximately 30 minutes of CPU time on the CRAY Y-MP computer. Convergence histories for cases using slip wall boundary conditions were nearly identical to those for cases using a specified pressure boundary condition.

Additional details concerning this algorithm and its numerical implementation may be found in Reference 31.

3.4 Boundary Conditions

The method of artificial compressibility used in the INS2D code allows for boundary conditions to be specified using the method of characteristics, similar to compressible flow solvers. In the case of the artificial compressibility scheme, however, the method of characteristics is merely a mathematical construct which allows for waves to exit at the boundaries of the computational domain without reflection.

There are three characteristic lines associated with three eigenvalues of the system of equations: u, u+c, u-c, where c is the artificial speed of sound in this method. At an inflow boundary, there is one characteristic line carrying information from the interior of the solution to the boundary. At an outflow boundary there are two characteristic lines carrying information from the interior of the solution to the boundary.

The approach used in this work was to treat both the outflow plane and top and bottom walls as outflow boundaries. Although not strictly correct for a wall boundary which allows both inflow and outflow, this approach is consistent with that used by other researchers [17-21]. The problems associated with making velocity measurements near a wind tunnel wall usually result in only one flow variable being specified as a wall boundary condition in wind tunnel simulations. Additionally, an abrupt change from inflow to outflow boundary conditions on the wall usually results in discontinuities in the solution.

The outflow boundary condition, as implemented in the INS2D code, can most easily be understood by consideration of a limiting case in which the method is applied to a uniform, orthogonal grid. In this case, for an outflow boundary, the method reduces to:

$$v_n = -\frac{p_n}{\left(v + \sqrt{v^2 + \tilde{\beta}}\right)} \tag{3.14}$$

$$u_n = p_n \left(1 - \frac{v}{\left(v + \sqrt{v^2 + \tilde{\beta}}\right)}\right)\left(\frac{u}{v^2 + \tilde{\beta}}\right) \tag{3.15}$$

where the n-subscript denotes differentiation in the direction normal to the boundary. For other cases, the metrics of the transformation and local rotations also affect the equations.

With p specified at the boundaries, and for cases where the artificial compressibility parameter $\tilde{\beta} >> u, v$, as was the case in this work, this method results in an extrapolation of interior velocities to the boundary. It does, however, still allow for small variations in pressure and velocity normal to the surface to avoid wave reflections. It therefore allows for faster convergence than a simple extrapolation scheme.

3.5 Two-Dimensional Grid Generation

Grids were developed which conformed to boundaries on which experimental data was available. The inflow plane of the grid corresponded to the inflow plane on which five-hole probe data was taken. Top and bottom boundaries of the grid corresponded to the nominal (0-degree inclination) top and bottom wall locations. The outflow plane corresponded to the breather section location. These grids were used for all slip wall computations and for all cases in which pressure was specified as a boundary condition. A special grid was developed for the viscous solid wall case. For that case, the top and bottom boundaries of the grid corresponded to the inclined wall locations.

All grids used with the INS2D code were developed using GRIDGEN software [37]. Surface definitions were based on spline fits to approximately 2000 measurements of the model geometry. The very high resolution of measured model geometry allowed for excellent geometry definition in the grids as well as resolution of model defects associated with the attachment of the model flap and spoiler. Orthogonality was maintained at the airfoil surface by using exponential blending of grid lines near the surface. The Thompson Middlecoff elliptical solver was used within the GRIDGEN software to develop the grids. This solver maintains boundary distributions of grid points in the interior of the grid and allows for easy refinement of the grid in boundary layers over the airfoil. Spacing was controlled so that approximately 15 to 20 grid points were located within the boundary layer on the airfoil. All of the grids developed were C-grids. Normal grid dimensions were 250 x 70, although a test case was run using a 350 x 105 grid to examine the effect of grid refinement. An example of these grids may be seen in Figure 2.

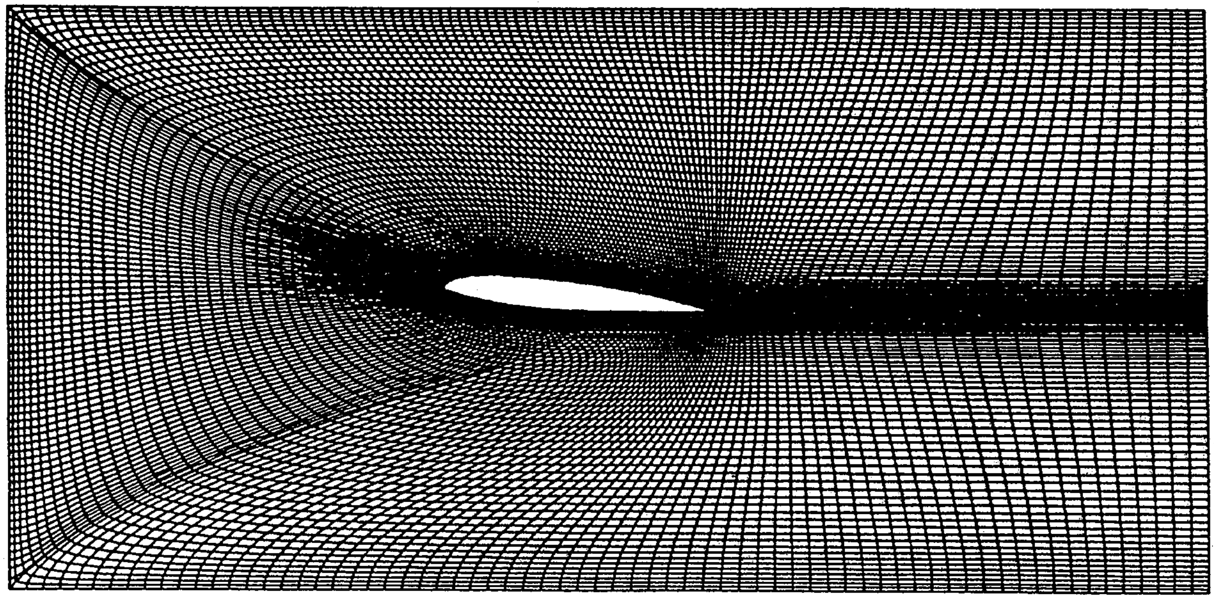

Figure 2. Grid used for two-dimensional CFD simulations for $\alpha = 5$ degrees.

Chapter 4

Experimental Apparatus

4.1 Wind Tunnel Test Section

A specially constructed test section was built for use in the Stanford Low Speed Wind Tunnel. This test section was heavily instrumented with static pressure tappings on the walls and with five hole probe access on the inflow and outflow planes and on planes near the top and bottom walls. The test section was designed to allow for two-dimensional testing and three-dimensional half-span testing. For two-dimensional testing the top and bottom walls were porous and both side walls were solid. For three-dimensional half span testing, the model was mounted to a solid wall and the remaining three walls were porous.

The test section was .457 m x .457 m and the porous portion of the test section was .76 m long. The porous walls were constructed using a layered design to allow the open area ratio to be varied. The layer of the wall nearest the flow was a slotted layer with .00254 m streamwise slots located at .0254 m intervals. The middle layer of the wall consisted of inserts which had .0229 m by .00254 m rectangular holes located at .0254 m intervals. These holes were inclined to the normal at 15 degrees, giving the porous wall a differential resistance to inflow and outflow. The outer layer of the wall was also slotted similar to the inner layer and could be slid laterally to vary the open area ratio of the wall. Open area ratios of the walls could be varied from a solid wall condition to an open area ratio of 9-percent. An atmospheric plenum was used for all porous wall tests. An exploded view of this wall design may be seen in Figure 3.

An atmospheric breather section was also used in all tests and was located at the end of the test section. The nominal freestream velocity for all tests was 24. m/sec and the nominal Mach number for all tests was M = .07. The nominal Reynolds number based on chord was Re = 3.2×10^5 for the airfoil tests and 2.4×10^5 for the three-dimensional wing tests. The test section top and bottom walls were adjustable and were inclined normal to the freestream to compensate for boundary displacement layer growth through the test section. Displacement layer thickness was measured by a boundary layer rake located near the end of the porous portion of the test section. Displacement layer thicknesses were measured on both the top and bottom walls with the model in place. The rake was removed during normal tunnel operation. A schematic of the wind tunnel may be seen in Figure 4, and a photograph of the test section may be seen in Figure 5.

4.2 Wind Tunnel Models

The two-dimensional model used in these tests was a Boeing Advanced Transport Airfoil. A cross section of this airfoil may be seen in Figure 6. The model had a flap and a spoiler which were in the retracted position for these tests. The airfoil chord was .203 m and the maximum thickness ratio was 11.3 percent. Measurements of the model were made with a Leitz Precision Measuring Machine with an accuracy of 2.54×10^{-6} m, or approximately .00125 percent of the airfoil chord. Approximately 2000 measurements were made to define the airfoil cross section. Grit was applied to the airfoil between 2.5 and 5.0 percent of the chord [38, 39]. Nominal grit diameter was .03175 cm. Oil flow studies were undertaken to ensure the two-dimensionality of the flow field and to ensure that the grit applied to the model successfully triggered transition on the airfoil.

The three-dimensional model used in these tests was an unswept half-span wing with an aspect ratio of 1.5, a span of .229 m and a chord of .152 m. The wing had a constant NACA 0018 airfoil cross section. The wing tip was a half body of revolution with diameter equal to the local thickness of the wing. Grit was applied to the wing between 2.5 and 5.0 percent of the chord. Nominal grit diameter was .03175 cm. Oil flow studies were undertaken to ensure that the grit successfully triggered transition on the wing.

4.3 Test Section Instrumentation

The test section was instrumented with static pressure tappings on the porous walls and five-hole probe access near the top and bottom walls and on the inflow and outflow planes. The tunnel was instrumented with 78 static pressure tappings on the centerlines of the upper and lower walls and a total of 482 static pressure tappings on the upper and lower walls. An additional 121 pressure tappings were located on the porous side wall. Pressure tappings were also located on both models. The five-hole probe was used to determine flow inclinations and velocity perturbations on the inflow and outflow planes as well as planes near the top and bottom walls.

Static pressure data was acquired by three Scanivalves which were calibrated on each run. Together, these Scanivalves were capable of making 576 pressure mesurements on each run. Nominal freestream velocity was determined by static pressure measurements taken in the inlet contraction bell. These measurements were sufficiently far upstream so that interference from the model was negligible. The velocity measurements were calibrated in empty tunnel runs.

4.4 Wind Tunnel Flow Quality

Empty tunnel flow quality surveys were conducted and may be seen for solid wall and porous wall cases in Figures 7 and 8, respectively. A velocity variation of approximately 4 percent may be seen in these surveys at the inflow plane location. This effect appears to be local to the inflow plane of the test section, and is much less pronounced near the model location. Instrumentation access holes restricted the range of positions at which measurements could be made. In these cases, as in the data which is shown later, the nominal free stream velocity is based on static pressure measurements made in the contraction section of the wind tunnel.

4.5 Error Analysis

All pressure measurements were obtained with instrumentation calibrated against a secondary standard traceable to the National Bureau of Standards. Pressure measurements on the walls and airfoil were made with three Scanivalves, each having four 48-port barrels. Two ports on each barrel were used for a reference and calibration pressure. This allowed the pressure transducer in each barrel to be calibrated on each run. A settling time of approximately 1 second was allowed after each advancement of the Scanivalve barrel. A low pass (10 Hz) filter was used to filter data from the pressure transducers. Pressure readings were based on an average of 200 measurements taken at 1 kHz. Standard deviations were computed for these measurements and were typically 0.01-percent or less of the mean data values. A calibration pressure of 0.100 psi ($.689 \times 10^3$ N/m^2) was used for wall pressure measurements and a calibration pressure of 0.200 psi (1.378×10^3 N/m^2) was used for airfoil pressure measurements. Uncertainties in the calibration pressure measurements were $\pm 0.6 \times 10^{-3}$ psi (4.13 N/m^2), based on manufacturer supplied data. Additionally, discretization by the data acquisition board resulted in a minimum resolution error of $.1 \times 10^{-3}$ psi (.69 N/m^2) for the airfoil measurements and $.05 \times 10^{-3}$ psi (.34 N/m^2) for the wall measurements. Non-linearity of the pressure transducers was estimated at less than .2-percent based on a comparison of known pressure differences and transducer outputs. These errors combined to give an overall error of approximately .9-percent in Cp measurements on the airfoil and 1.2-percent in Cp measurements on the walls.

Five-hole probe pressure data was obtained by dedicated 1 psi Druck pressure transducers. These transducers were calibrated on each run using the secondary standard discussed above. Calculation of flow angularity without direct measurements of velocity perturbations led to results of unknown accuracy. The relationship between pressure coefficient measurements with a five-hole probe and flow angles is complex. Adding to uncertainties in pressure mesaurements were uncertainties regarding probe alignment. A qualitative assessment of the probe data could be made by comparing data taken from identical runs, or by observing the variations in repeated probe measurements made at the same point in the flow field. This qualitative assessment suggested that typical probe error was on the order of 0.5 degree.

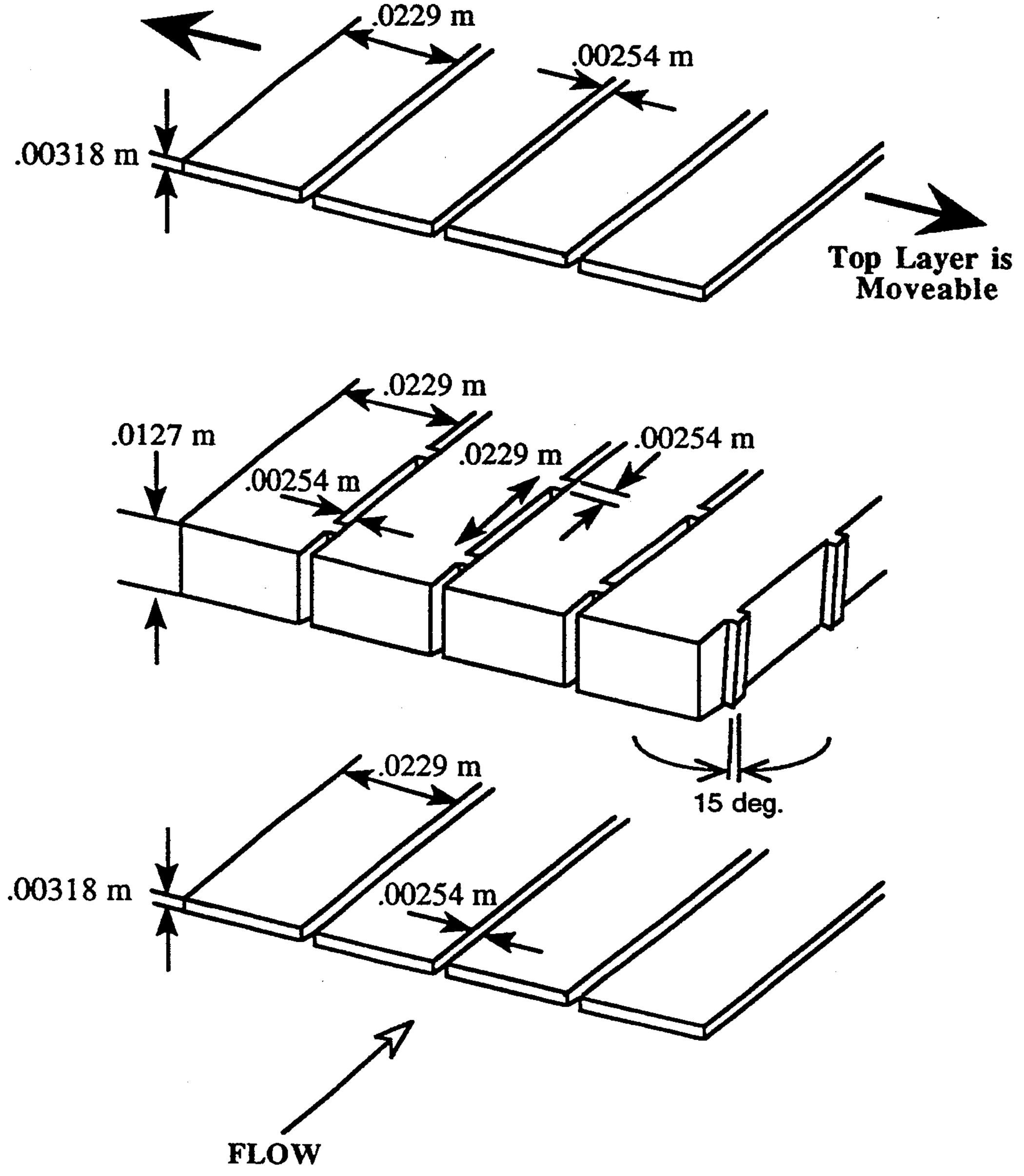

Figure 3. Exploded view of variable porosity wall.

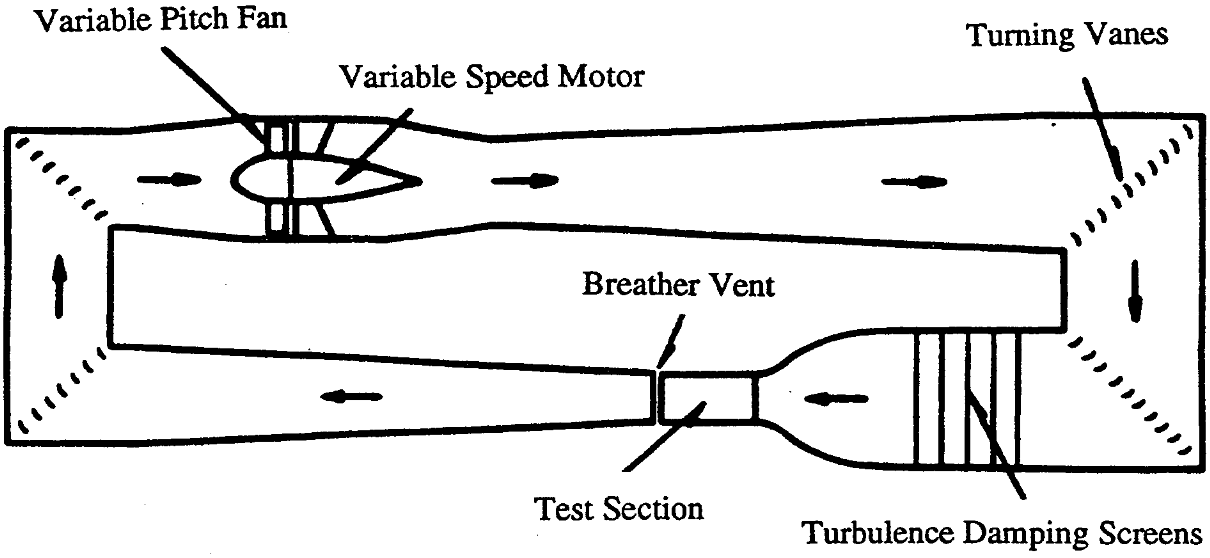

Figure 4. Schematic diagram of Stanford Low Speed Wind Tunnel.

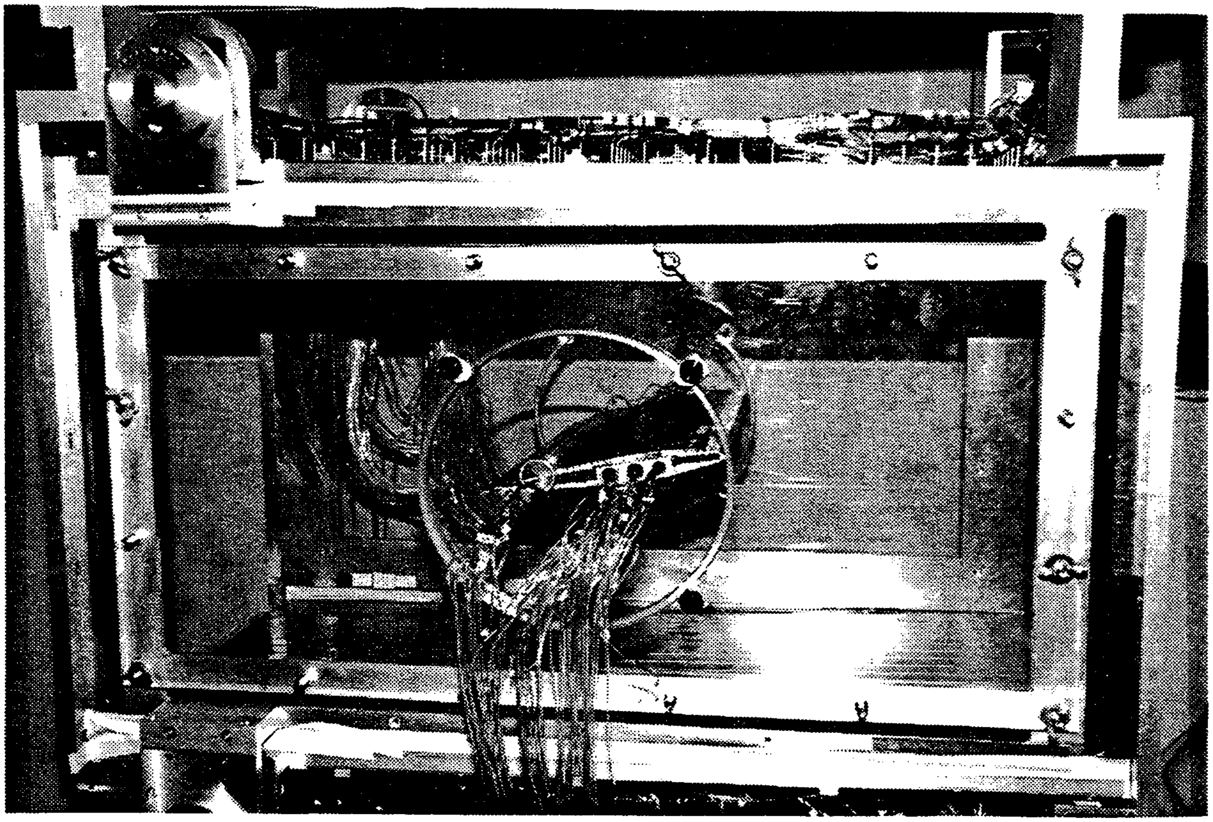

Figure 5. Variable porosity test section. Airfoil model is shown installed.

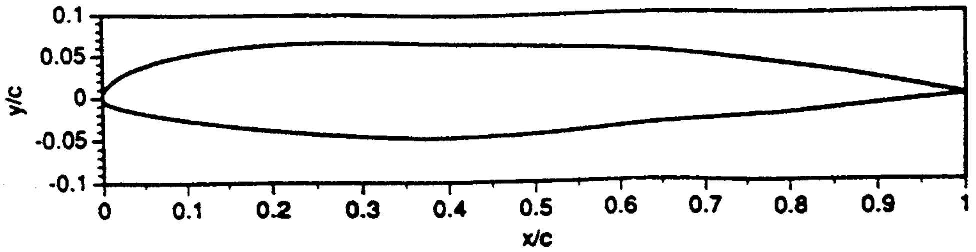

Figure 6. Boeing Advanced Transport airfoil cross section.

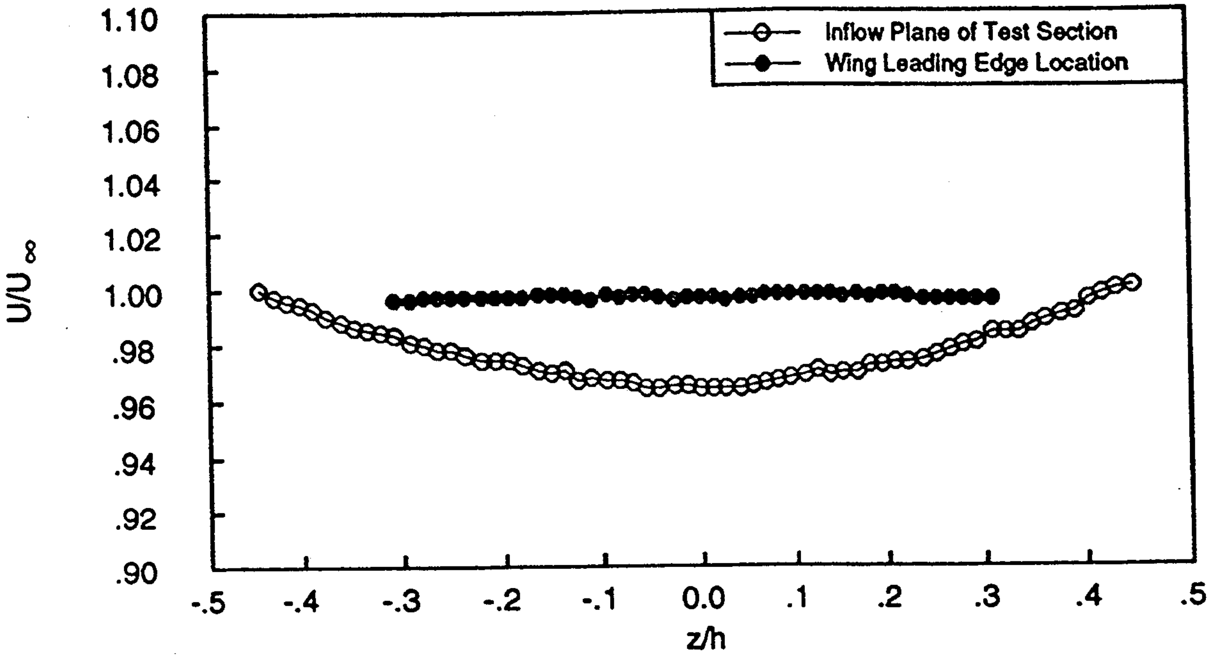

Figure 7. Empty tunnel, solid wall flow quality surveys at test section entrance and model location.

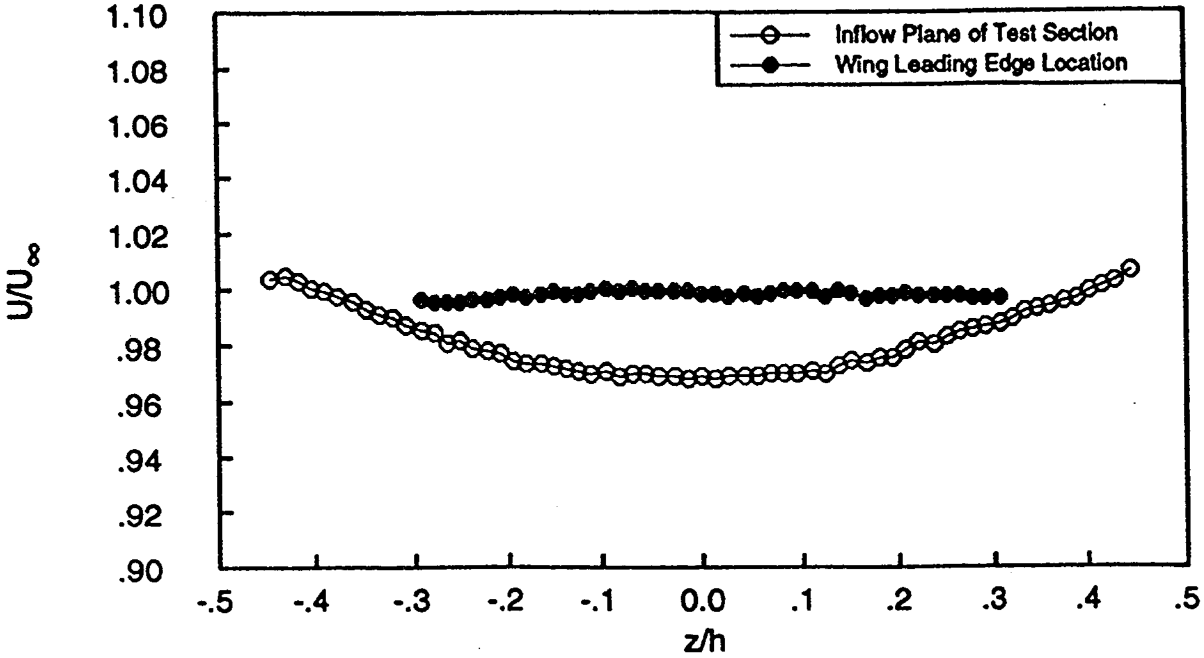

Figure 8. Empty tunnel, porous wall flow quality surveys at test section entrance and model location.

Chapter 5

Results

5.1 Two-Dimensional Case

Both computational and experimental studies were undertaken to evaluate the method of singularities for application to two-dimensional flows. Preliminary computational studies used a CFD solution to determine the number of measurements and the number of singularities required to develop an adequate description of the flow near the walls using the method of singularities. The experimental data was used to determine the suitability of this method to actual flow fields. Effects considered were: 1) the number of singularities and flow field measurements required to describe the flow near the walls, 2) the ability of this method to capture the effect of changes in the open area ratio of the walls, 3) the effects of uncertainties in the porosity parameter specified in the method of singularities, 4) the effects of singularity placement, 5) comparisons of alternate methods of describing a solid wall boundary, 6) the effects of grid refinement in the CFD code, 7) the effects of using sparse data to develop a wall pressure profile, and 8) flow inclinations near the boundary, as computed by the CFD code and measured by the five-hole probe.

5.1.1 Preliminary Computational Studies

As a means of evaluating the method of singularities, a CFD simulation using slip wall boundary conditions was developed. This simulation was then treated as a psuedo-experiment and data from the wall boundaries was used to develop a method of singularities solution. The use of a computational result instead of experimental data for this purpose allowed for a detailed comparison of pressure profiles on the walls and a comparison of the effects of using sparse data to develop the method of singularities solution. Figure 9 shows the pressure profiles on the walls as predicted by the CFD simulation using slip wall boundary conditions for an angle of attack of 5 degrees.

Figure 10 shows the root-mean-square errors resulting when various numbers of singularities and data points were used to develop the potential flow solutions. The data points were distributed as uniformly as grid spacing would allow over the top and bottom walls. Up to four derivatives of a source and vortex were retained in the method of singularities solutions. The root-mean-square errors shown in Figure 10 were based on a point-by-point comparison of the pressure predicted by the CFD simulation and the pressure predicted by the method of singularities at each grid point on the upper and lower walls. The root-mean-square errors have been normalized by the peak pressure coefficient on the walls. As may be seen in Figure 10, a relatively small number of singularities was adequate to describe the far field flow. In addition, a small number of measurement locations was sufficient to develop a potential flow solution. Additional data from the walls allowed for a better description of the pressure profile in the method of singularities, but beyond 25 data points the improvement was very small.

The use of additional singularities resulted in the need for additional data points in order to produce acceptable fits to the velocity profiles. It was found that the number of data points required to produce a good fit to the velocity profiles was approximately twice the number of singularities retained in the potential flow solution.

While these trends were observed for a variety of airfoil simulations [32, 40, 41], caution should be exercised when applying this method to different geometries. Some computational experimentation, of the type just described, may be required in order to develop confidence in this method for different geometries such as multi-element airfoils, blunt bodies, or configurations with very low height-to-chord ratios.

5.1.2 CFD Simulations of Experiments

The next step in evaluating this method was to use it to perform simulations of a series of wind tunnel tests. The tests were conducted in the variable porosity test section described in Chapter 4. The pressure profiles measured on the walls during the 5 degree angle of attack tests may be seen in Figure 11a. This figure shows data from both the solid wall tests and the porous wall tests with a 9-percent open area ratio. Also shown in Figure 11a are the potential flow solutions based on this data. These potential flow solutions were developed using the 77 measurements on the wind tunnel walls and a total of 10 singularities (a source, a vortex, and the first four derivatives in the streamwise direction of a source and vortex.) Figures 12a-17a show similar results for angles of attack of 6, 7, 8, 9, 10, and 11 degrees. As can be seen in these figures, the potential flow solutions showed excellent agreement with the experimental data.

The potential flow solutions shown in Figures 11a-17a were imposed as boundary conditions in the Navier-Stokes solver and the resulting pressure profiles obtained on the airfoil are shown in Figures 11b-17b. Also shown in Figures 11b-17b are the airfoil pressure profiles obtained in the wind tunnel tests. Experimental and computational results compared very well. The largest discrepancies were approximately 6-percent of the peak values. These discrepancies occurred at the location of the grit transition strip on the model. At locations away from the grit strip, however, agreement was much better with typical discrepancies of approximately 1-percent of peak values. A comparison of airfoil pressure profiles from the solid wall and porous wall tests showed that this method simulated the effect of a porous wall very well. As the porosity of the wall was varied, the trend in pressure profiles on the airfoil was duplicated in the CFD simulations by imposing the potential flow solution as a pressure boundary condition in the CFD solver.

Also of interest in Figures 11b-17b are the slight deviations seen in the pressure profiles on the airfoil between $x/c = 0.75$ and $x/c = 0.80$. These deviations may be seen on both the upper and lower surfaces and are present in both the experimental and CFD data. They are the result of small ridges on the airfoil model between the main airfoil and the retracted flap and spoiler.

The root-mean-square errors in matching experimental pressure coefficients on the walls using the method of singularities are summarized in Table 1. Also shown in Table 1 are the root-mean-square errors between measured pressures on the airfoil and pressures predicted by the CFD code with the method of singularities boundary condition imposed. In both cases, these root-mean-square errors are based on a point-by-point comparison at all locations where experimental data was available. The root-mean-square errors shown for wall and airfoil cases have been normalized by peak pressure coeffiecients measured on the wall and airfoil, respectively, in each test.

	Wall Measurements		**Airfoil Measurements**	
Angle of Attack (deg)	**Solid Wall**	**Porous Wall**	**Solid Wall**	**Porous Wall**
5	0.00777	0.01485	.02669	.03023
6	0.00732	0.01435	.02368	.02703
7	0.00743	0.01420	.02205	.02023
8	0.00722	0.01357	.01995	.01753
9	0.00705	0.01300	.02045	.01525
10	0.00739	0.01350	.02331	.01819
11	0.00756	0.01327	.02635	.02234

Table 1. Root-mean-square errors in matching pressure coefficients on the walls using the method of singularities, and in matching experimental pressure coefficients on the airfoil with the INS2D CFD code.

5.1.3 Effect of Changes in Porosity Parameter

In the results shown above, the porosity parameter used in the method of singularities was determined by minimizing the root-mean-square errors in matching the wall pressure profile. As a means of evaluating the sensitivity of this method to uncertainties in the porosity parameter specified in the method of singularities, a variety of porosity parameters were used to develop potential flow solutions in the method of singularities. Figure 18 shows root-mean-square errors in matching pressure coefficients on the walls as a function of the porosity parameter specified in the method of singularities for the 9-percent porous wall, 8-degree angle of attack case. The root-mean-square errors shown in this figure have been normalized by the peak pressure coefficient measured on the walls. These results are typical of the results at other angles of attack. It is noticeable that the curves shown are discontinuous at P = 0. The reasons for this discontinuity have already been discussed in Chapter 2. In all the cases examined, the optimum porosity parameter was found to be P = 0. For non-zero porosities, the optimum porosity depends on the number of singularities retained and the optimum tends to be very shallow. This again points out the danger of using Equations 2.10 and 2.11 directly as a boundary condition in CFD codes.

Figures 19 and 20 show a comparison of results obtained by specifying a porosity parameter of 0. and 1. in the method of singularities solution. These results are for the porous wall tests at an angle of attack of 8 degrees, and using 10 singularities in the method of singularities. Figure 19 shows the resulting pressure coefficient profiles on the walls, and Figure 20 shows the resulting pressure coefficient profiles predicted by the CFD code on the airfoil. As can be seen in Figure 19, the finite test section effects associated with the change in porosity are most noticeable near the inflow and outflow planes of the test section. The trend in pressure profiles was captured with either specified porosity. As can be seen in Figure 20, the discrepancies in the pressure profiles of Figure 19 have little effect on the airfoil pressure profiles. Overall, this method is relatively insensitive to uncertainties in the porosity parameter. By using a least-squares approach to determine singularity strengths, this method allows singularity strengths to vary as needed in order to provide an optimum fit to the experimental data for any specified value of porosity. This effect may be seen in Figure 21, which shows the singularity strengths in the method of singularities as a function of the porosity parameter specified on the walls. For clarity, only 6 singularity strengths are shown in this figure.

5.1.4 Effect of Changes in Singularity Placement

In the results discussed above, all singularities were placed at the quarter-chord, tunnel centerline location ($x/c = 0.25$, $y = 0.0$). Figure 22 shows the effect of varying the location of the singularities. Singularity locations were varied from $x/c = 0.0$ to $x/c = 1.0$. The resulting root-mean-square errors in matching the pressure profile on the walls for the solid wall, 8-degree angle of attack case are shown. Again, the root-mean-square errors have been normalized by the peak pressure coefficient on the wall. As can be seen, this method is relatively insensitive to the position of the singularities, provided that the singularities are placed ahead of the mid-chord point. An increase in the root-mean-square errors occurs as the singularities are placed further downstream, although even these errors are relatively small. As noted earlier, some caution should be exercised when applying these results. When using this method with geometries significantly different from those used here, such as multi-element models or extremely low height-to-chord ratios, it may be necessary to distribute singularities in order to adequately model the pressure profile on the walls.

5.1.5 Comparison of Alternate Boundary Conditions for Solid Wall Simulations

As a means of comparing this approach to other methods of specifying boundary conditions in CFD codes, CFD simulations were performed of the solid wall 8-degree angle of attack test using 3 alternate boundary conditions. These alternate boundary conditions were: 1) A slip-wall boundary condition ($v = 0$) applied at the nominal wall location, 2) A no-slip boundary condition ($u = v = 0$) applied at the physical wall location, and, 3) A free-air boundary condition ($u = u_\infty$, $v = v_\infty$, $p = p_\infty$) applied at a distant boundary with corrections applied to the airfoil angle of attack and the freestream velocity.

The grid used for the slip wall simulation was the same grid used to specify the pressure boundary condition. The outer boundary of this grid corresponded to the nominal wall location. As discussed earlier, the walls were inclined to adjust for the growth of the displacement layer through the test section.

Figure 23 shows the grid used for the no-slip wall simulation. This grid models the wall inclinations through the test section and uses additional refinement near the walls to resolve the wall boundary layer.

Figure 24 shows the grid used in the free-air simulations. For the free-air boundary condition, classical incidence and velocity corrections were applied to the wind tunnel data [42]. The CFD simulation was performed with the airfoil at the corrected angle of attack and the velocity corrections were applied in non-dimensionalizing the data. The outer boundary was located 30 chord lengths from the airfoil.

Figure 25 shows the pressure profiles on the airfoil resulting from these simulations, as well as the simulations using the pressure boundary condition from the method of singularities. Experimental data is also shown for reference. The specified pressure boundary condition, based on the method of singularities, produced the closest match to the experimental data. The slip wall and no-slip wall showed similar results which were also in close agreement with the experimental data. The free-air simulation showed significant discrepancies (approximately 18-percent of peak values) with experimental data at the pressure peak, although overall agreement was much closer. Overall agreement between these methods was close, although differences may clearly be seen in the area near the pressure peak on the airfoil. The overall agreement of these approaches demonstrated the consistency of this method with other means of specifying boundary conditions for solid wall tests. This agreement gave added confidence in this method when it was used for simulating porous wall boundary conditions.

5.1.6 Grid Refinement Effects

The effects of grid refinement were also considered for the solid wall data from the 8-degree angle of attack case. The grids used in the above results had already been refined to the point where additional grid refinement appeared to have little effect on the solution. For comparison purposes, however, an additional result was computed on a further refined grid using approximately twice the number of grid points as were used in the standard grids typical of Figure 2. Figure 26 shows a 350 x 105 grid which was used to simulate the 8-degree angle of attack, solid wall case. Figure 27 shows a comparison of the results obtained for this case on the 350 x 105 grid and the 250 x 70 grid which was used in the other simulations. As can be seen in this figure, differences between these results are minor. Some additional refinement was evidenced near the flap and spoiler ridges on the aft portion of the airfoil, but overall results indicated that the 250 x 70 grid was sufficiently refined so that remaining errors associated with grid refinement were minor.

5.1.7 Effects of Using Sparse Data

The effect of using sparse data to develop potential flow solutions was also investigated. Figure 28a shows 8 data points selected from the complete set of wind tunnel data for the solid wall test at 5 degrees angle of attack. A potential flow solution based on these 8 data points is also shown. In addition, the complete set of wind tunnel data and the potential flow solution based on the complete set of data is also shown for reference. For the sparse data (8 data point) solutions, only first derivatives of the source and vortex were retained in the method of singularities, resulting in a total of 4 singularities being used to develop the potential flow solution. Figures 29a-34a show similar results for solid wall tests at 6-11 degrees angle of attack and Figures 35a-41a show similar results using data from the 9-percent open area ratio porous wall tests. The potential flow solutions based on 8 data points show close agreement with the potential flow solutions based on 77 data points. Root-mean-square errors between experimental measurements and method of singularities solutions based on 8 data points are shown in Table 2. These root-mean-square errors are based on a point-by-point comparison of the entire set of 77 experimental measurements with the method of singularities solution based on 8 measurements. The root-mean-square errors are normalized by the peak pressure measured on the walls for each case. As expected, these errors were higher than the cases in which 77 data points were used to develop the solution (see Table 1), however the trend of the pressure profiles is still captured using very sparse data. This agreement indicates that this method was robust enough to allow for a good description of the boundary conditions on the walls even when only very sparse data was available from the wind tunnel walls.

	Wall Measurements		**Airfoil Measurements**	
Angle of Attack (deg)	**Solid Wall**	**Porous Wall**	**Solid Wall**	**Porous Wall**
5	0.01847	0.03960	.02576	.02978
6	0.01720	0.04033	.02294	.03163
7	0.01786	0.03706	.02077	.02341
8	0.01628	0.03369	.01994	.01986
9	0.01689	0.03420	.01894	.01397
10	0.01678	0.03330	.02136	.01478
11	0.01703	0.03303	.02485	.01773

Table 2. Root-mean-square errors in matching pressure coefficients on the walls using the method of singularities based on 8 experimental measurements, and in matching experimental pressure coefficients on the airfoil with the INS2D CFD code.

The pressure profiles shown in Figures 28a-41a were imposed as boundary conditions in the CFD code and the resulting pressure profiles on the airfoil are shown in Figures 28b-41b. For reference, the airfoil pressure profiles which resulted by imposing the boundary conditions of Figures 11a-17a in the CFD code are also shown in Figures 28b-41b. This allows a comparison of the effect on the airfoil of using sparse data to develop the wall boundary conditions. As can be seen in these figures, the method of singularities provided a means of describing boundary conditions which was sufficiently robust so that little effect was seen in the airfoil pressure coefficient profiles from significantly reducing the number of measurements used to develop the boundary conditions. Root-mean-square errors between experimental data on the airfoil and the CFD results using boundary conditions based on 8 data points are also summarized in Table 2. Again, these errors have been normalized by the peak pressure measured on the airfoil in each case. These errors are comparable to those for the cases in which 77 data points were used to develop the boundary condition (see Table 1), and indicate that this method may produce close agreement between computed and experimental measurements on the airfoil even when only very sparse data is available to develop boundary conditions.

5.1.8 Flow Inclinations Near the Boundaries

Five-hole probe measurements were made on a plane near the boundaries, as described in Chapter 4. These measurments were used to develop a qualitative assessment of the flow inclinations near the walls.

Figures 42 and 43 show the normal velocities measured near the walls during porous wall tests of the airfoil at angles of attack of 5 and 8 degrees, respectively. In these figures, the normal velocity is plotted against the streamwise location. Velocity profiles are shown for both the top and bottom walls, and all velocity measurements are normalized by freestream velocity. Also shown in these figures are the computed normal velocities from the CFD code. These normal velocities are taken from a plane in the CFD result corresponding to the five-hole probe measurement plane. These CFD results were obtained by specifying the pressure boundary conditions of Figures 11 and 14 in the CFD code. The difficulties of making experimental flow inclination measurements with the five-hole probe may be seen in Figure 43 which shows discrepencies between data obtained from two consecutive runs. These uncertainties make any quantitative comparison of computed and measured results questionable. A qualitative comparison of computed and measured results shows that the CFD code with a pressure boundary condition is capturing the trend of the normal velocities near the walls over most of the boundary.

5.2 Three-Dimensional Case

Limited consideration was also given to three-dimensional applications of this method. No CFD simulations were performed for the three-dimensional data. However, the method of singularities was used to develop potential flow solutions based on the data measured on the walls. The effects of using different numbers and arrangements of measurements were considered, as well as the effects of using different numbers of singularities.

5.2.1 Method of Singularities Comparison to Experimental Data

Figures 44a, 44b, 45a, 45b, and 46 show the pressure profiles on the upper, lower and side walls from the three-dimensional solid wall tests of the half-span wing at an angle of attack of 20 degrees. Also shown in these figures are the pressure profiles developed by the method of singularities using 342 data points and 16 singularities to match the data. Figures 47-49 show similar results for the 9-percent open area ratio porous wall tests.

As can be seen in these figures, the agreement of the method of singularities fit to the experimental data is better in two dimensions than in three dimensions. This is in part due to the finite test section effects near the inflow plane and outflow plane. The abrupt change in boundary conditions associated with the breather section and inlet of the wind tunnel test section caused flow anomalies which the method of singularities could not adequately model. Only data from the central region of the test section is shown in Figures 44-49. The root-mean-square errors based on a comparison of experimental pressure profiles and those predicted from the method of singularities are 5.1-percent of the peak pressure coefficient for the solid wall case and 7.6-percent of the peak pressure coefficient for the porous wall case. Over the central region of the test section, the method of singularities captured the general trend in pressure profiles on all three walls.

5.2.2 Effects of Sparse Data and Reduced Numbers of Singularities

The effects of using reduced numbers of singularities and sparse data in the three dimensional method of singularities were also investigated. Figures 50a-c show the position of the 342 pressure tappings on the walls which were used to develop the method of singularities solutions shown in Figures 44-49. Figures 51a-c show 223 measurements arranged along the centerlines of each wall and three vertical or spanwise lines on each wall. These data points were also used to develop a method of singularities solution. The resulting solution was then evaluated based on a point-by-point comparison to the complete set of 342 experimental measurements. Figures 52a-c shows 136 measurements arranged along the centerlines of each wall and a single vertical or spanwise line on each wall. Figures 53a-c shows a total of 38 sparse data locations taken from the data in Figure 51a-c. The measurements indicated in Figures 51, 52 and 53 were also used to develop method of singularities solutions which were evaluated based on point-by-point comparisons to the complete set of 342 measurements.

Figures 54 and 55 show the root-mean-square errors resulting from a point-by-point comparison of the entire data set and the method of singularities solutions based on the data at the positions shown in Figures 50-53. Results are shown in these two figures for the solid and porous wall, respectively. Figures 54 and 55 also show the effects of using various numbers of singularities to develop these solutions. The results shown are based on 3, 7, 11, and 16 singularities being retained in the solution. Table 3 shows the order in which terms were included in the singularity solutions. All root-mean-square errors shown in Figures 54 and 55 have been normalized by the peak pressure coefficients measured on the walls.

Number of Singularities	Singularities Used
3 Singularity Case	Uniform freestream, Line Source, Horseshoe Vortex
7 Singularity Case	Uniform freestream, Line Source, Horseshoe Vortex First Derivatives of Source and Vortex in x-direction First Derivatives of Source and Vortex with respect to y_0
11 Singularity Case	Uniform freestream, Line Source, Horseshoe Vortex First Derivatives of Source and Vortex in x-direction First Derivatives of Source and Vortex with respect to y_0 Second Derivatives of Source and Vortex in x-direction Second Derivatives of Source and Vortex with respect to y_0
16 Singularity Case	Uniform freestream, Line Source, Horseshoe Vortex First Derivatives of Source and Vortex in x-direction First Derivatives of Source and Vortex with respect to y_0 Second Derivatives of Source and Vortex in x-direction Second Derivatives of Source and Vortex with respect to y_0 Third Derivatives of Source and Vortex in x-direction Third Derivatives of Source and Vortex with respect to y_0 First Derivative of Vortex in z-direction

Table 3. Singularities included in three dimensional method of singularities solutions.

The span of the line source, horseshoe vortex and their derivatives was equal to the span of the wing. Although not actually a singularity, the freestream term was retained in all cases to allow for the upstream contribution of the source term to be cancelled. As can be seen in Figures 54 and 55, the effect of adding additional measurements was to produce a better fit to the overall pressure profile on the walls. Additionally, as seen in the two-dimensional results, the addition of extra singularities in the potential flow solution required additional data points in order to provide an improved fit to the data. Overall lower root-mean-square errors were obtained for the cases of sparse data by using only 7 singularities instead of 11 or 16 singularities. As more data was used, however, the root-mean-square errors were reduced by using additional singularities to describe the flow field. These results suggest that approximately 10 data points should be used for each singularity retained in the method of singularities. As with the two dimensional results, however, caution should be exercised when applying these trends to different geometries. Some experimentation with numbers of singularities and data points may be required in order to develop confidence in this method for geometries and test conditions which are significantly different from those in this research.

Examples of the wall pressure profiles obtained by using reduced data to develop the method of singularities solution may be seen in Figures 56-61. Figures 56-58 show the pressure profiles on the top, bottom and side walls from the solid wall 20 degree angle of attack test and from the method of singularities using 7 singularities and 38 measurements at the positions shown in Figure 53. Figures 59-61 show similar results for the 9-percent open area ratio tests. As can be seen in these figures, even when only sparse data was available, the method of singularities captured the general trend in the pressure profiles over the central region of the test section.

5.2.3 Effects of Uncertainties in Porosity Parameter

The effect of the porosity parameter specified in this method was insignificant. As discussed earlier, the three-dimensional formulation of the method of singularities is continuous in its behavior at $P = 0$. Figure 62 shows the effect on root mean square errors of varying the porosity parameter from 0.0 to 1.0. These root-mean-square errors were based on a point by point comparison of the experimental measurements from the 20 degree angle of attack porous wall tests and the method of singularities solutions developed using porosities of 0.0, 0.5 and 1.0 in the panelling solutions. The complete set of 342 experimental measurements were used for these comparisons, and 16 singularities (see Table 3) were used to develop the method of singularities solutions. All root mean square errors were normalized by peak pressure coefficients measured during the test. Virtually no change was observed in the root-mean-square errors for these changes in the porosity parameter.

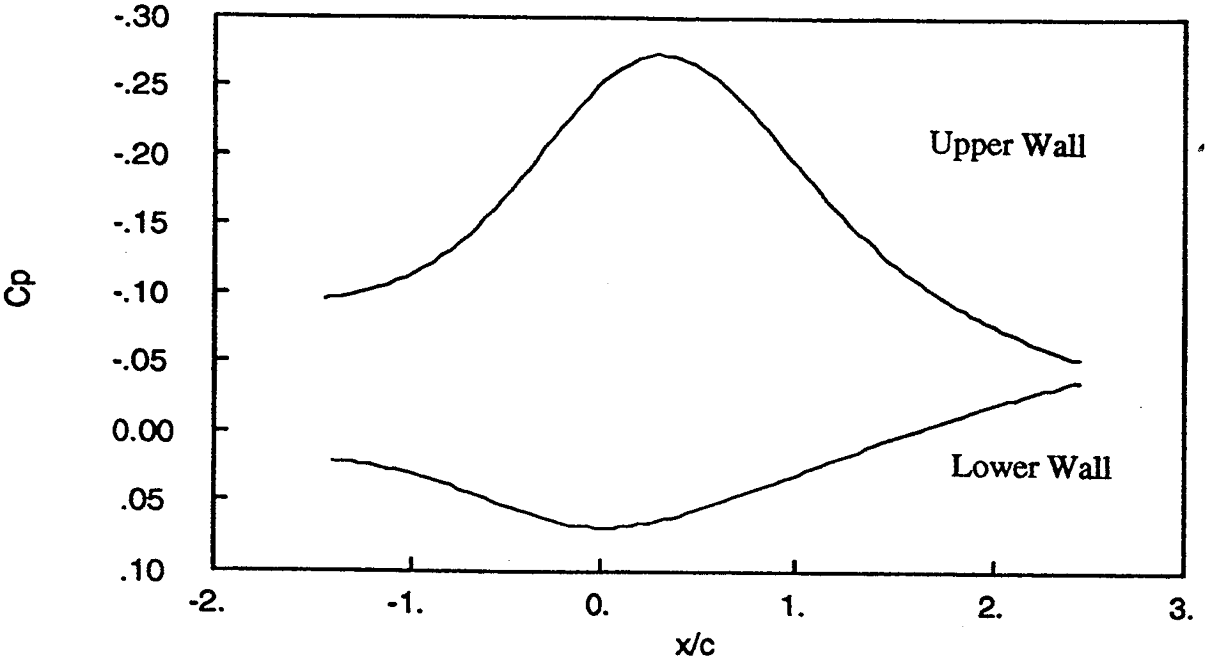

Figure 9. Velocity perturbation profiles on the top and bottom walls predicted by Navier-Stokes solver using a slip wall boundary condition.

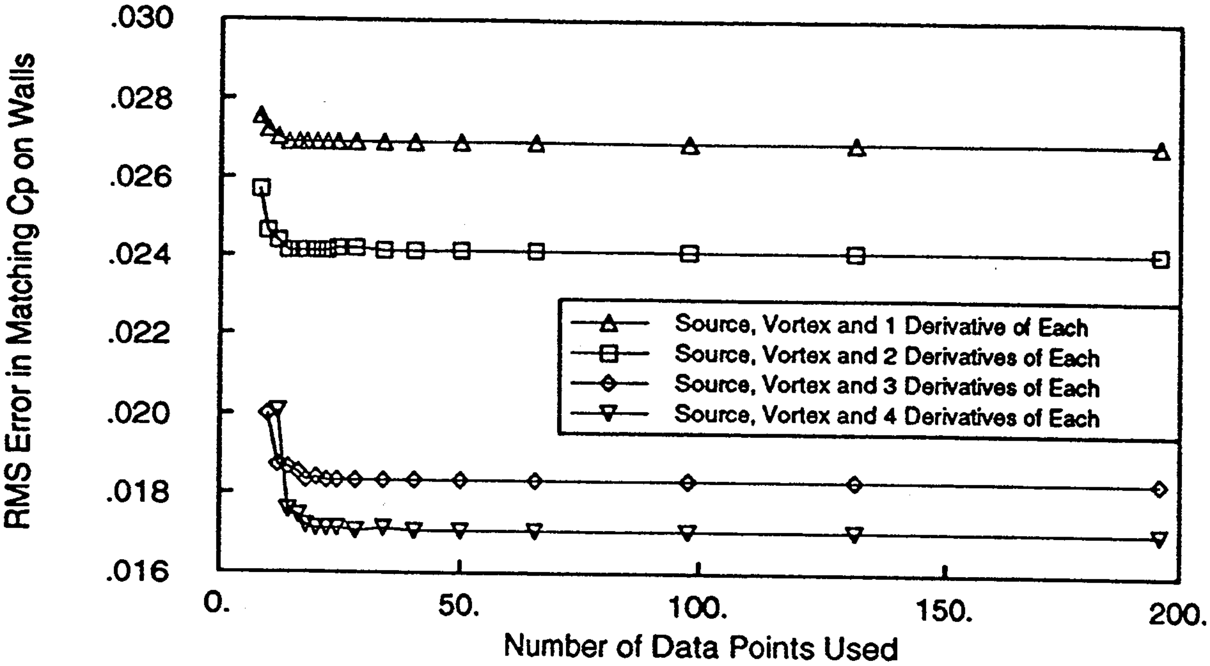

Figure 10. Root-mean-square errors as a function of the number of data points used to develop the method of singularities solution. Errors are normalized by peak pressure measured.

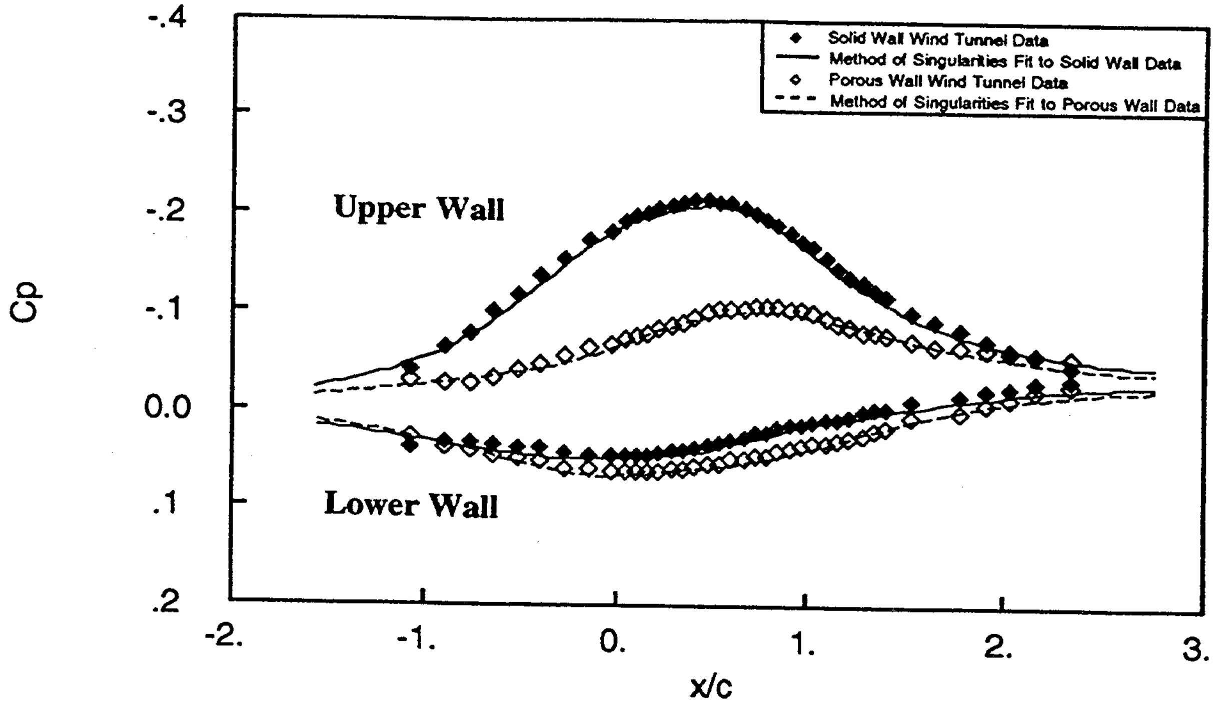

Figure 11a. Method of Singularities matches to pressure profiles on the wind tunnel walls for airfoil tests at $\alpha = 5$ degrees. $U_\infty = 24.$ m/s, Re = 3.2×10^5, h/c = 2.25.

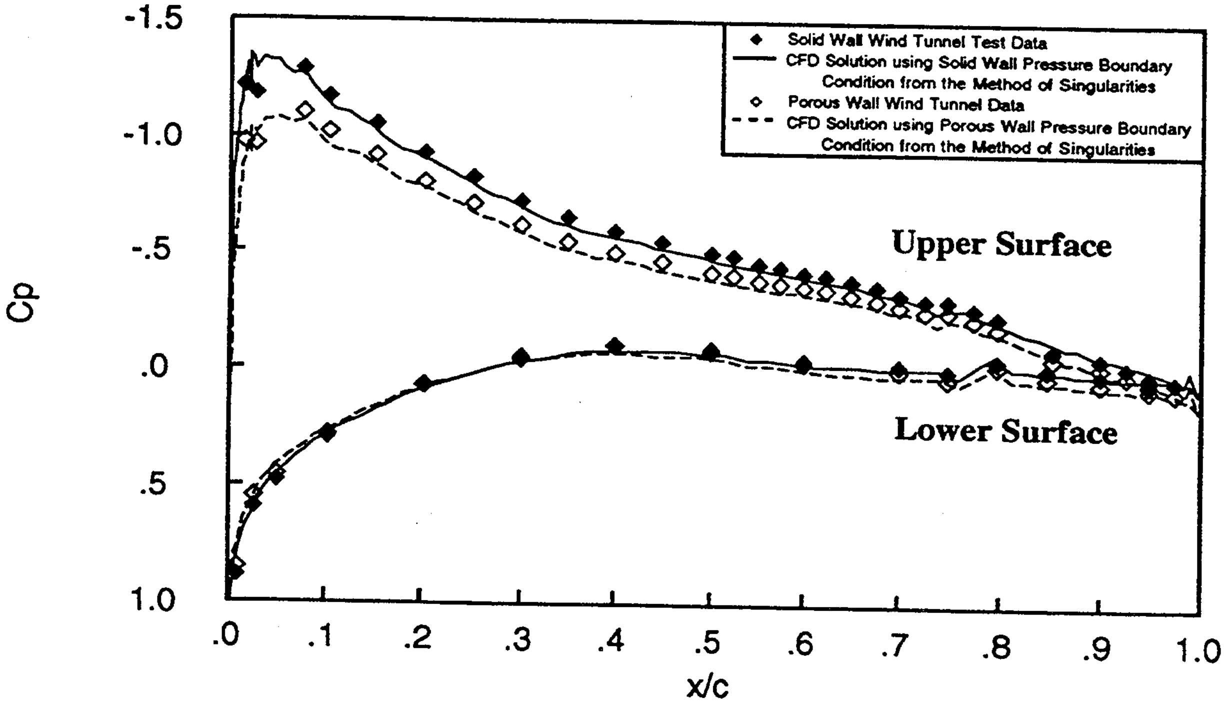

Figure 11b. Comparison of experimental and CFD pressure profiles on the airfoil for $\alpha = 5$ degrees. $U_\infty = 24.$ m/s, Re = 3.2×10^5, h/c = 2.25.

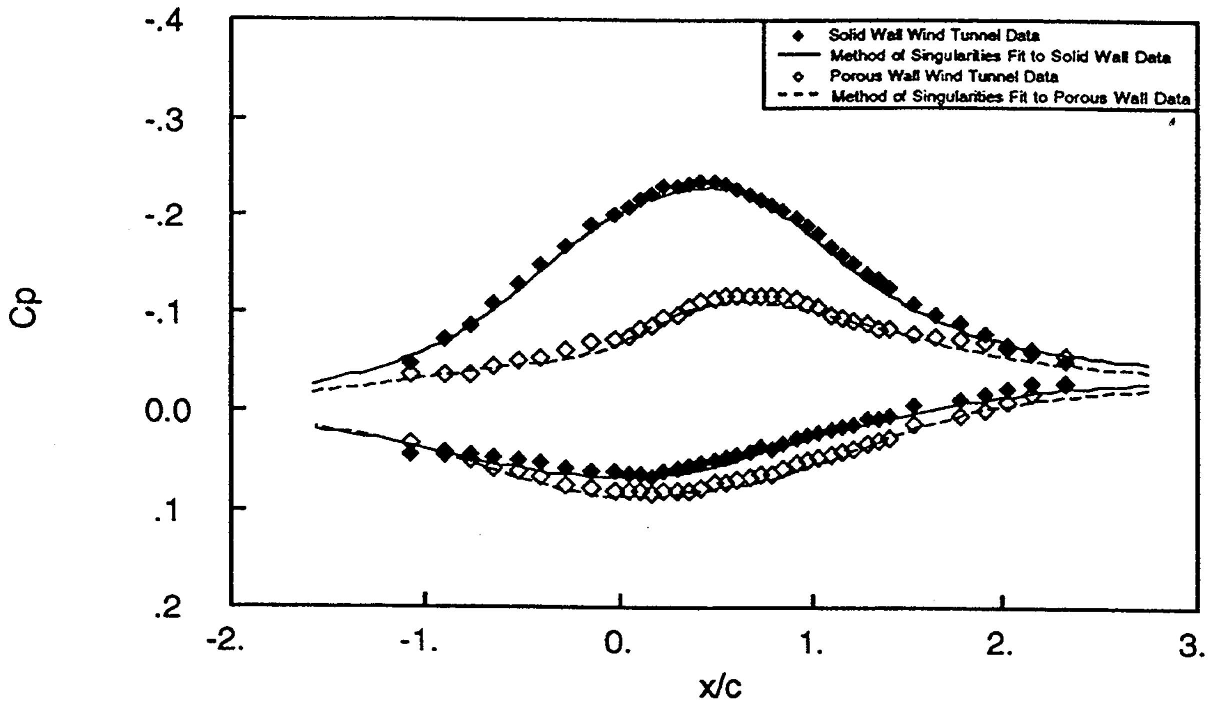

Figure 12a. Method of Singularities matches to pressure profiles on the wind tunnel walls for airfoil tests at $\alpha = 6$ degrees. $U_\infty = 24.$ m/s, $Re = 3.2 \times 10^5$, $h/c = 2.25$.

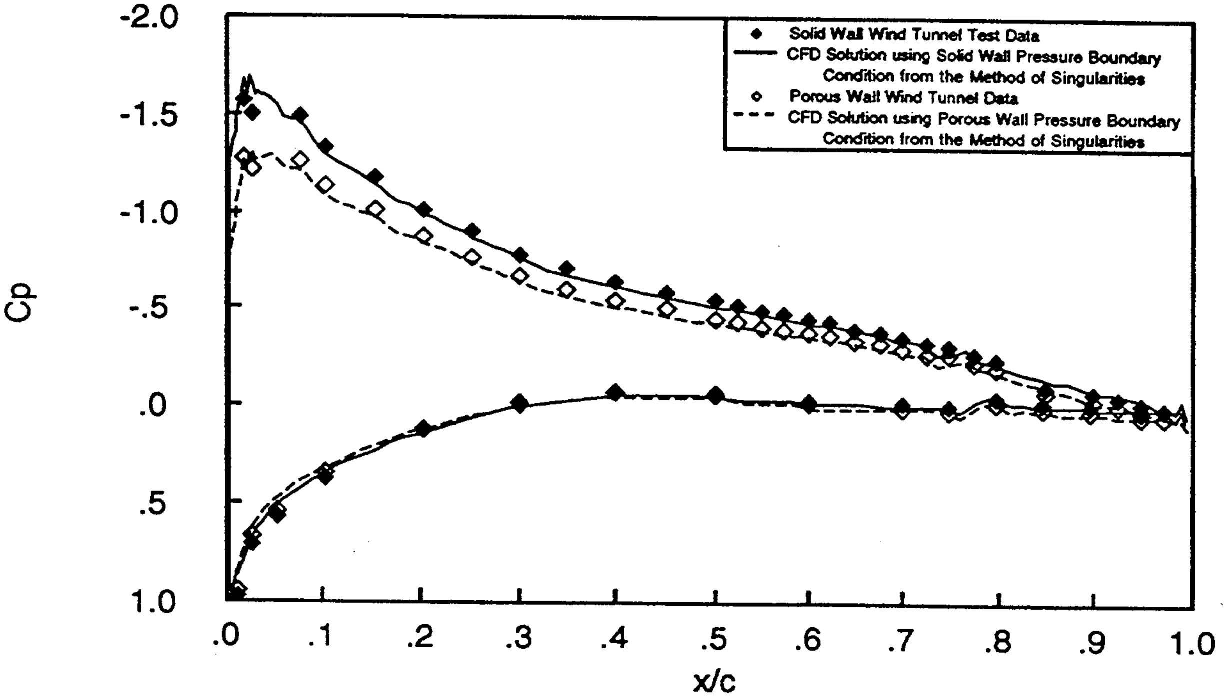

Figure 12b. Comparison of experimental and CFD pressure profiles on the airfoil for $\alpha = 6$ degrees. $U_\infty = 24.$ m/s, $Re = 3.2 \times 10^5$, $h/c = 2.25$.

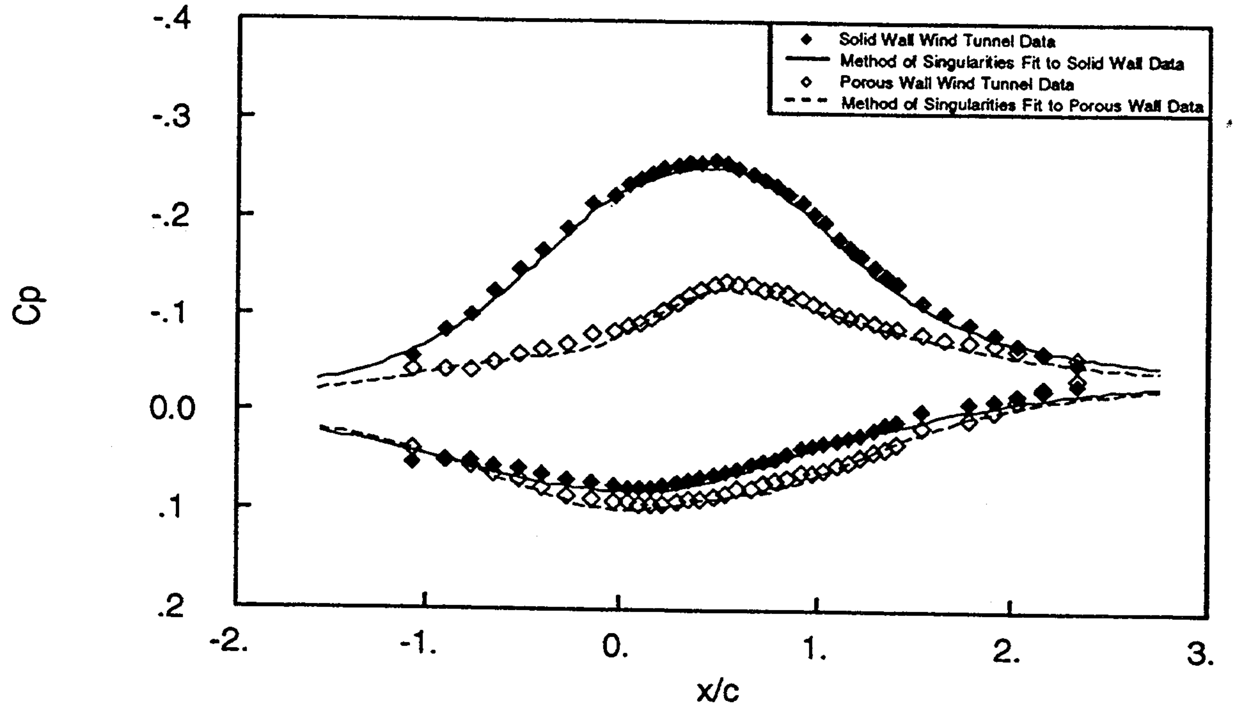

Figure 13a. Method of Singularities matches to pressure profiles on the wind tunnel walls for airfoil tests at $\alpha = 7$ degrees. $U_\infty = 24.$ m/s, $Re = 3.2 \times 10^5$, $h/c = 2.25$.

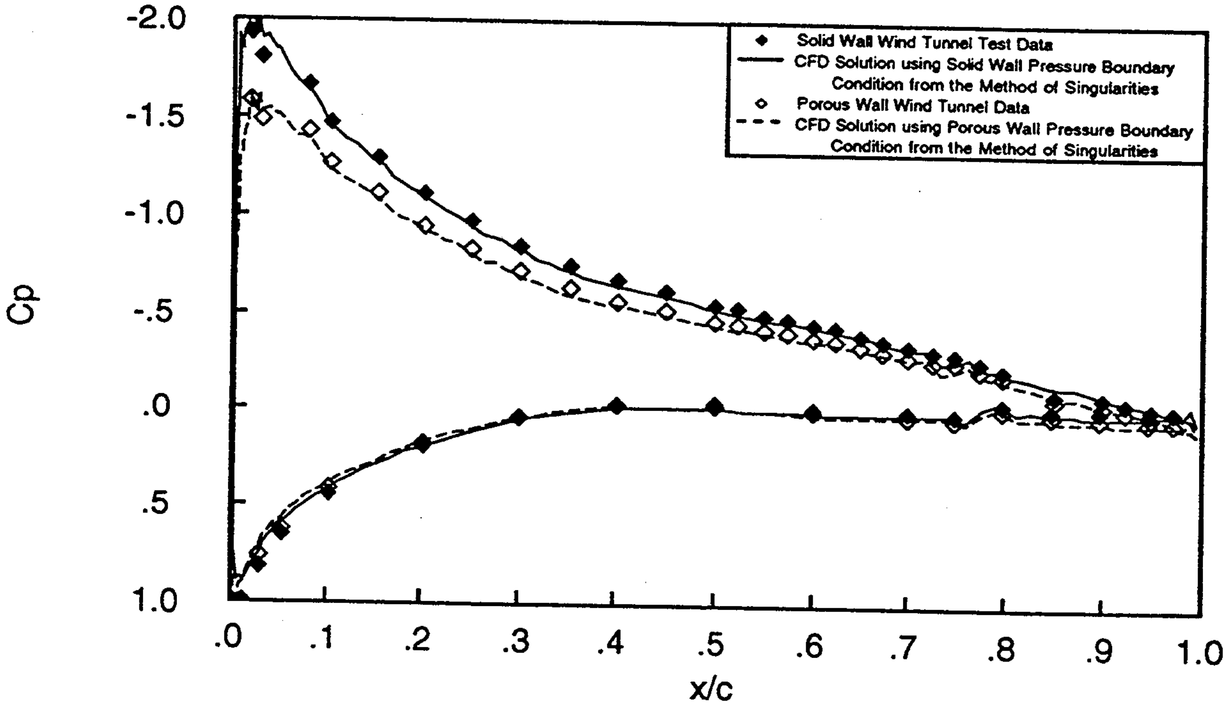

Figure 13b. Comparison of experimental and CFD pressure profiles on the airfoil for $\alpha = 7$ degrees. $U_\infty = 24.$ m/s, $Re = 3.2 \times 10^5$, $h/c = 2.25$.

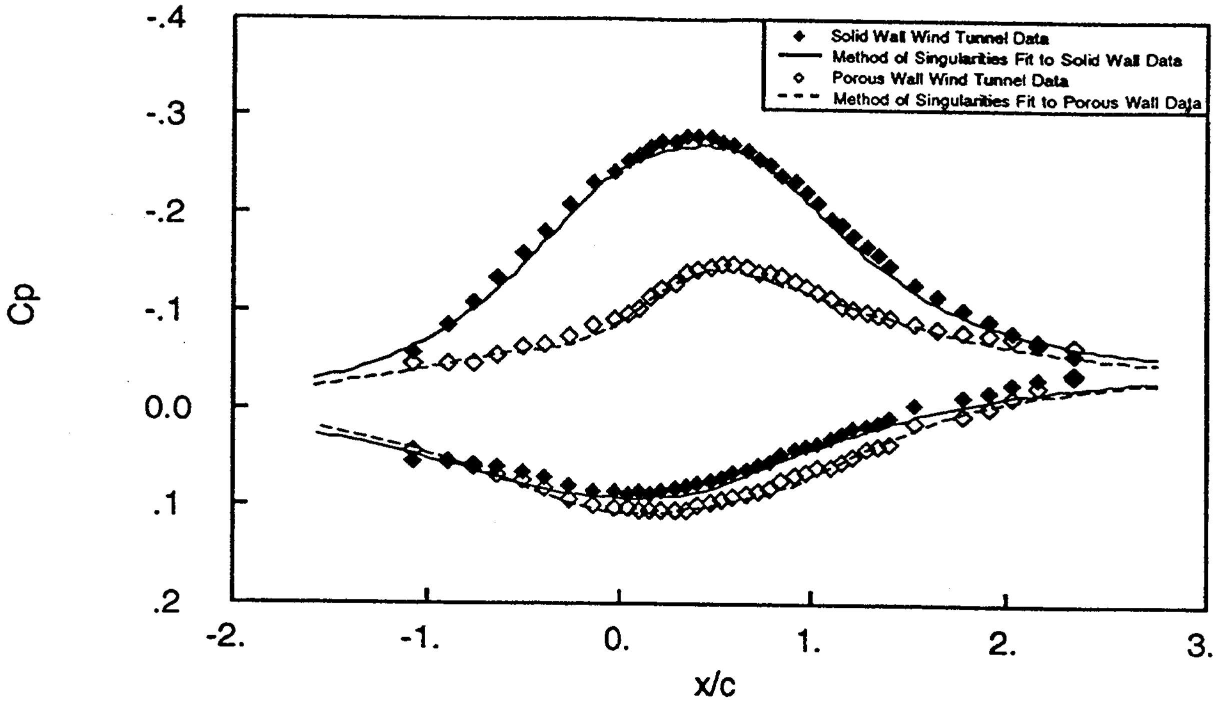

Figure 14a. Method of Singularities matches to pressure profiles on the wind tunnel walls for airfoil tests at $\alpha = 8$ degrees. $U_\infty = 24.$ m/s, Re = 3.2×10^5, h/c = 2.25.

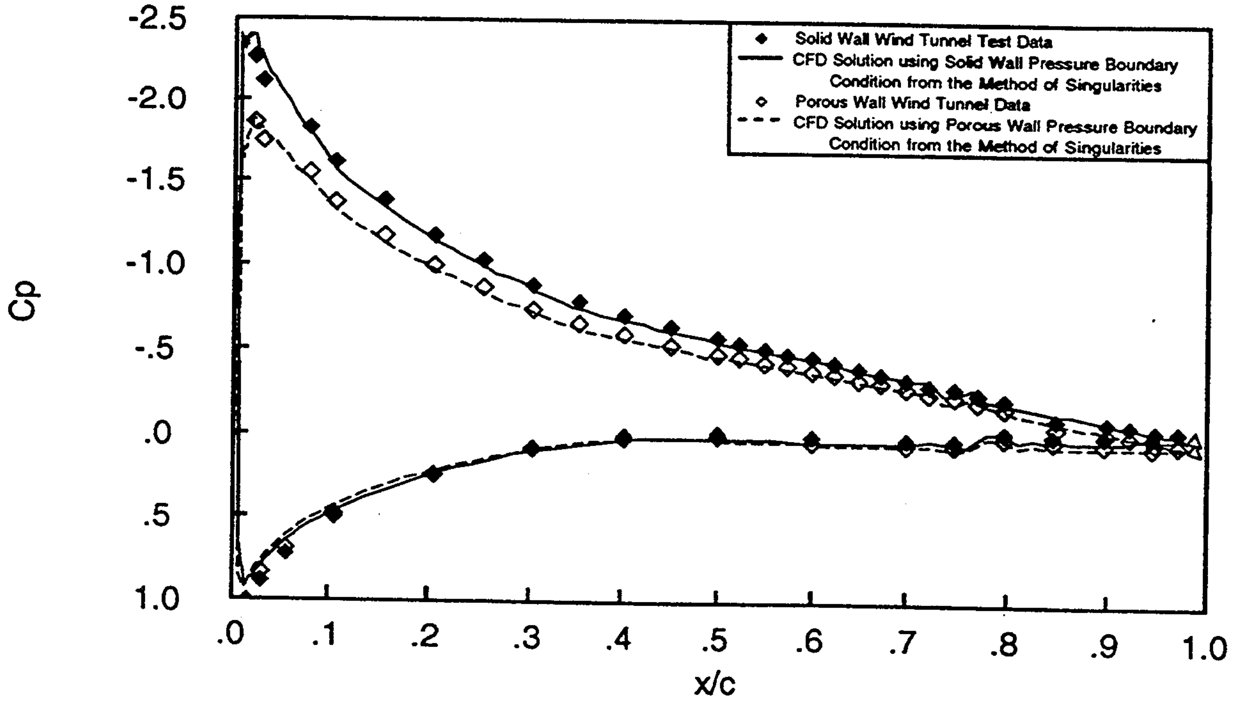

Figure 14b. Comparison of experimental and CFD pressure profiles on the airfoil for $\alpha = 8$ degrees. $U_\infty = 24.$ m/s, Re = 3.2×10^5, h/c = 2.25.

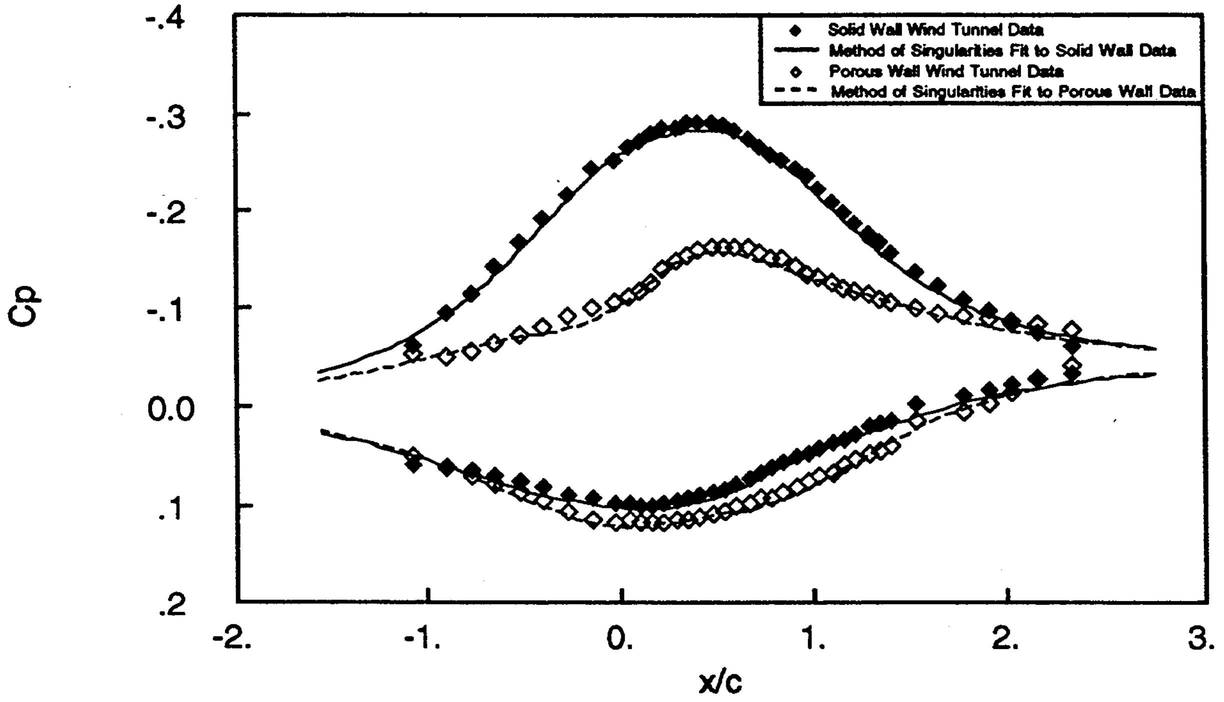

Figure 15a. Method of Singularities matches to pressure profiles on the wind tunnel walls for airfoil tests at $\alpha = 9$ degrees. $U_\infty = 24.$ m/s, $Re = 3.2 \times 10^5$, $h/c = 2.25$.

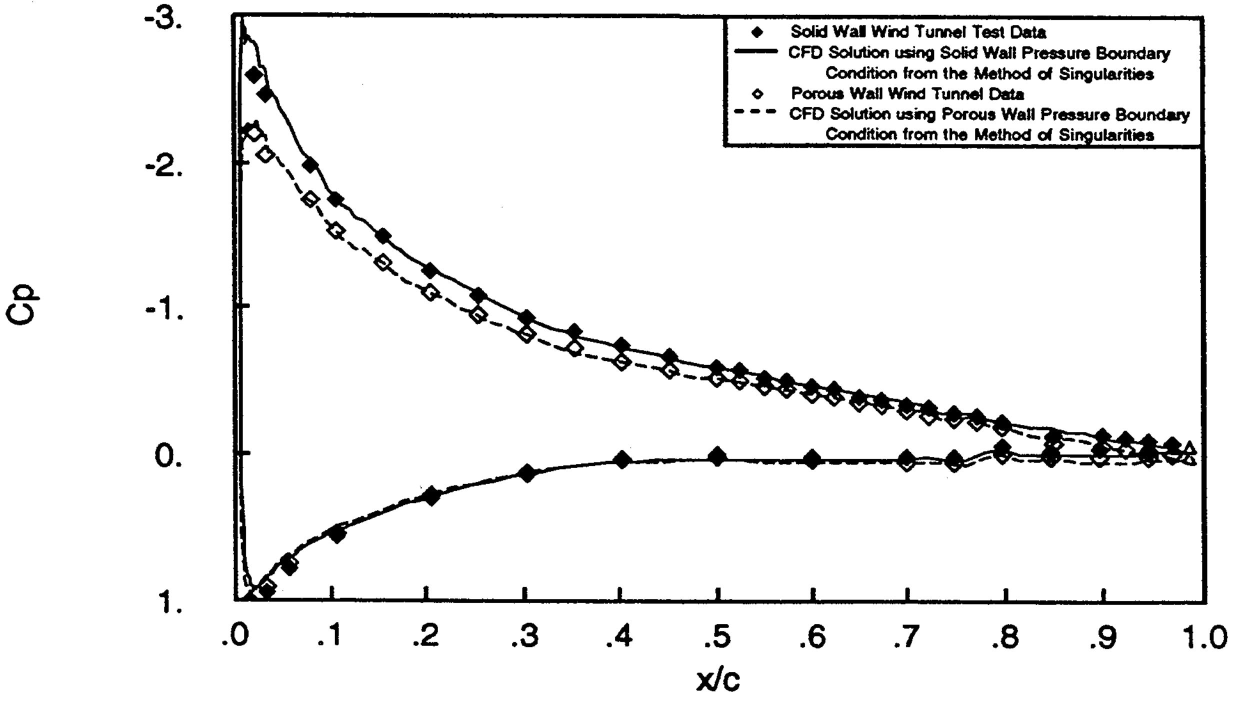

Figure 15b. Comparison of experimental and CFD pressure profiles on the airfoil for $\alpha = 9$ degrees. $U_\infty = 24.$ m/s, $Re = 3.2 \times 10^5$, $h/c = 2.25$.

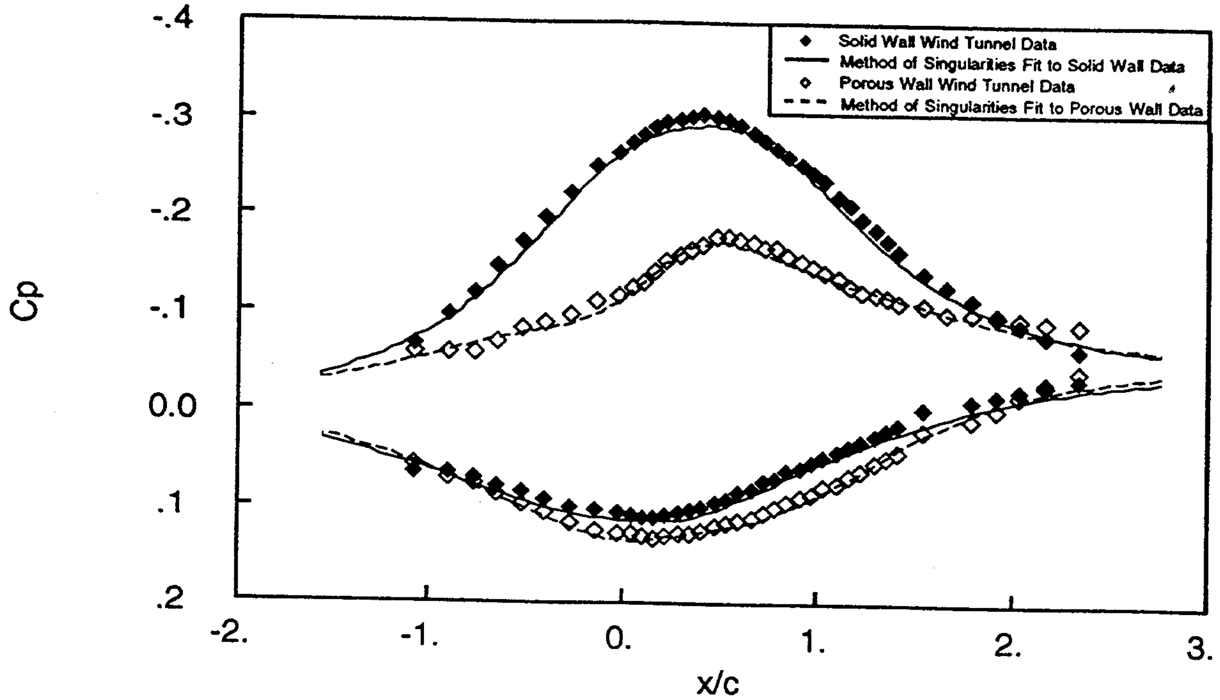

Figure 16a. Method of Singularities matches to pressure profiles on the wind tunnel walls for airfoil tests at $\alpha = 10$ degrees. $U_\infty = 24.$ m/s, $Re = 3.2 \times 10^5$, $h/c = 2.25$.

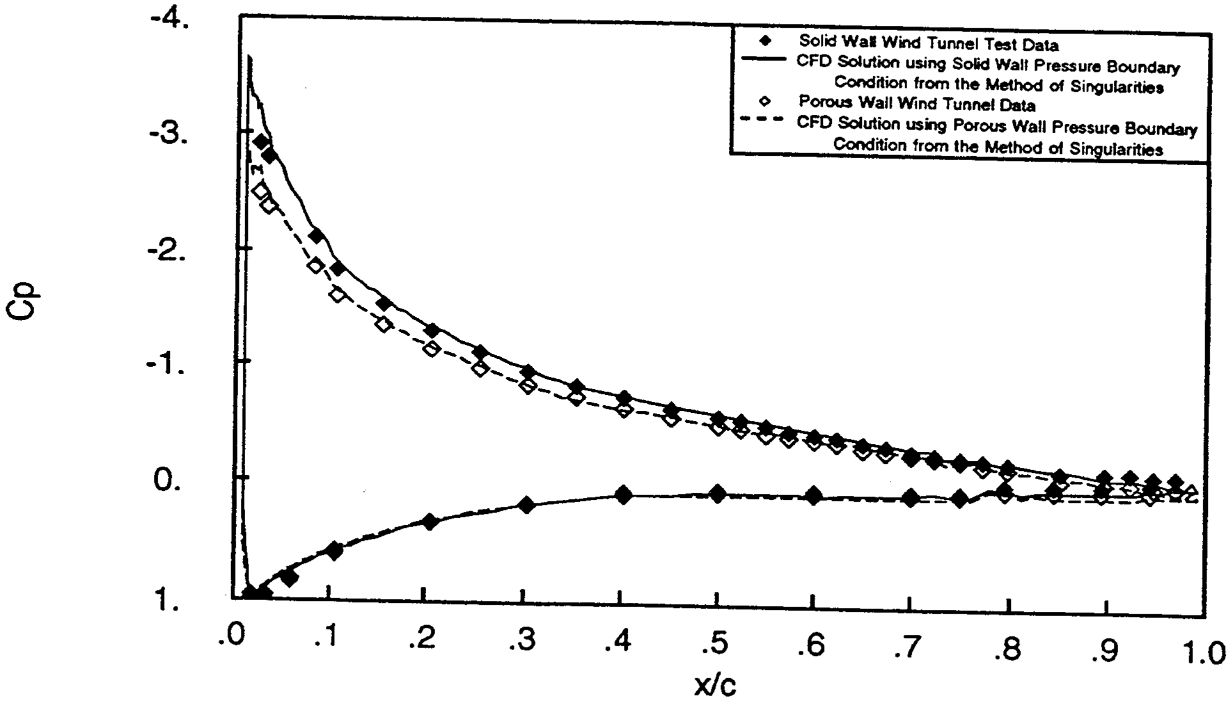

Figure 16b. Comparison of experimental and CFD pressure profiles on the airfoil for $\alpha = 10$ degrees. $U_\infty = 24.$ m/s, $Re = 3.2 \times 10^5$, $h/c = 2.25$.

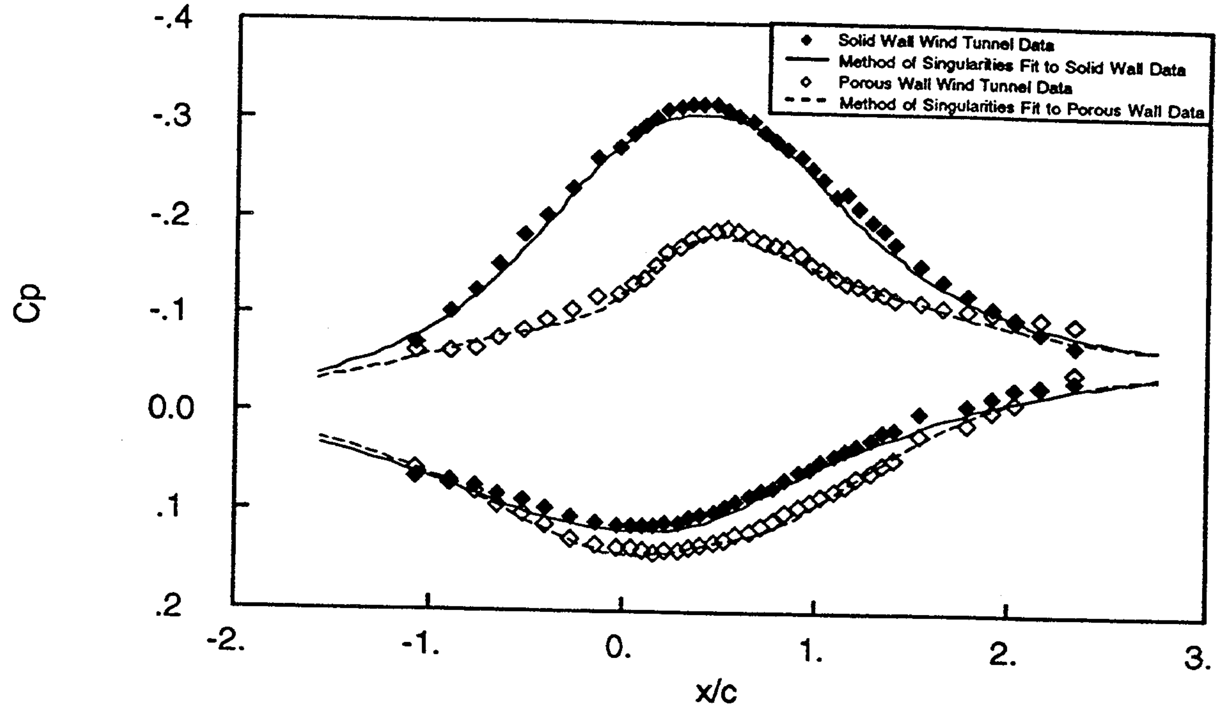

Figure 17a. Method of Singularities matches to pressure profiles on the wind tunnel walls for airfoil tests at α = 11 degrees. U_∞ = 24. m/s, Re = 3.2 x 10^5, h/c = 2.25.

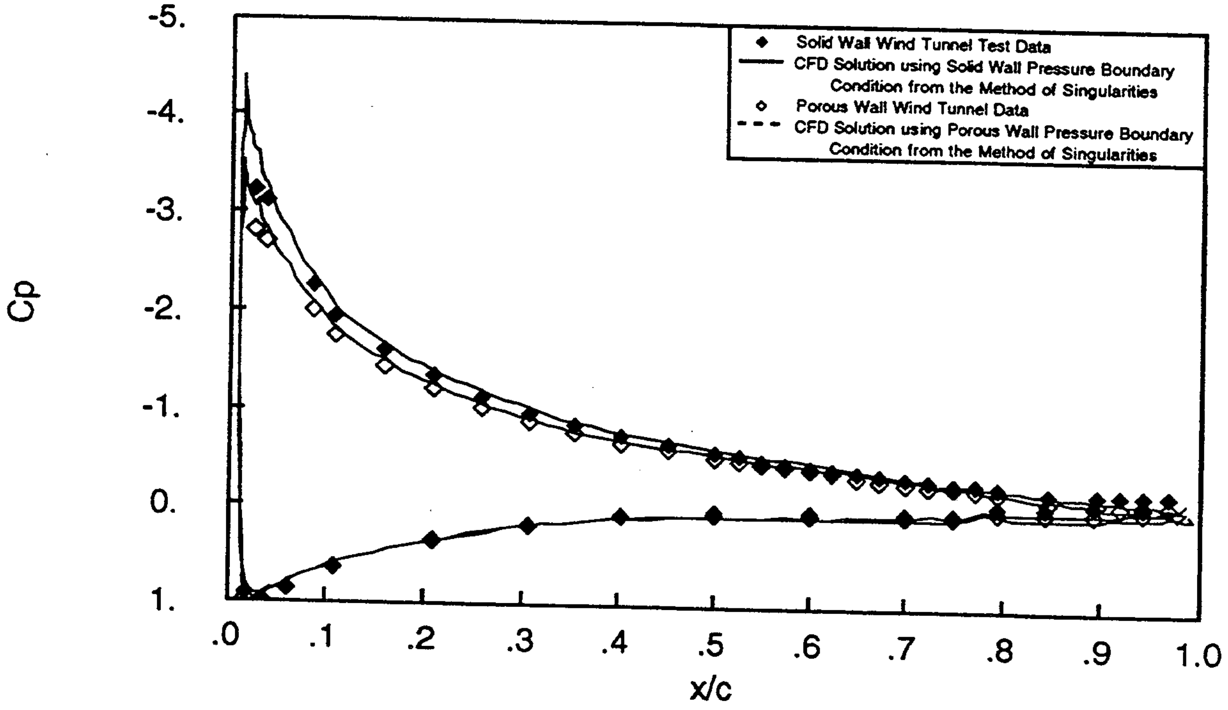

Figure 17b. Comparison of experimental and CFD pressure profiles on the airfoil for α = 11 degrees. U_∞ = 24. m/s, Re = 3.2 x 10^5, h/c = 2.25.

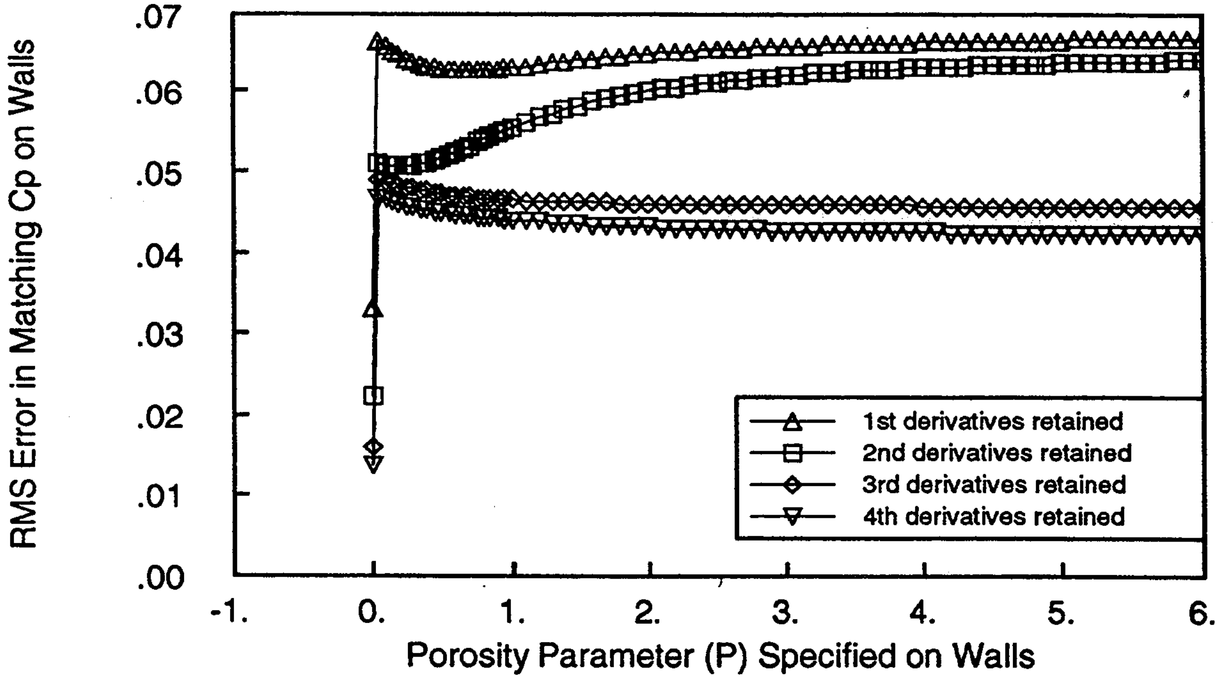

Figure 18. Root-mean-square errors as a function of porosity parameter specified in method of singularities solution. Experimental data from $\alpha = 8$ degrees, porous wall wind tunnel test.

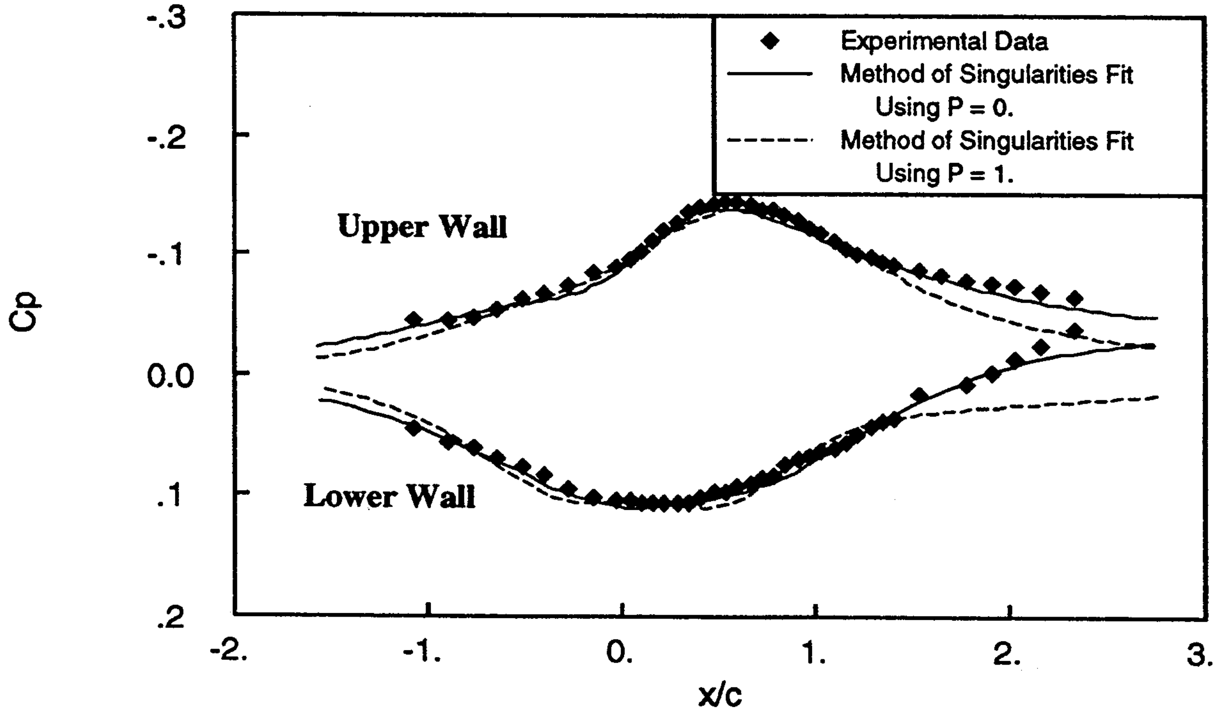

Figure 19. Method of singularities fits to experimental data using a porosity parameter of P = 0. and P = 1. Experimental data from the porous wall wind tunnel test at $\alpha = 8$ degrees.

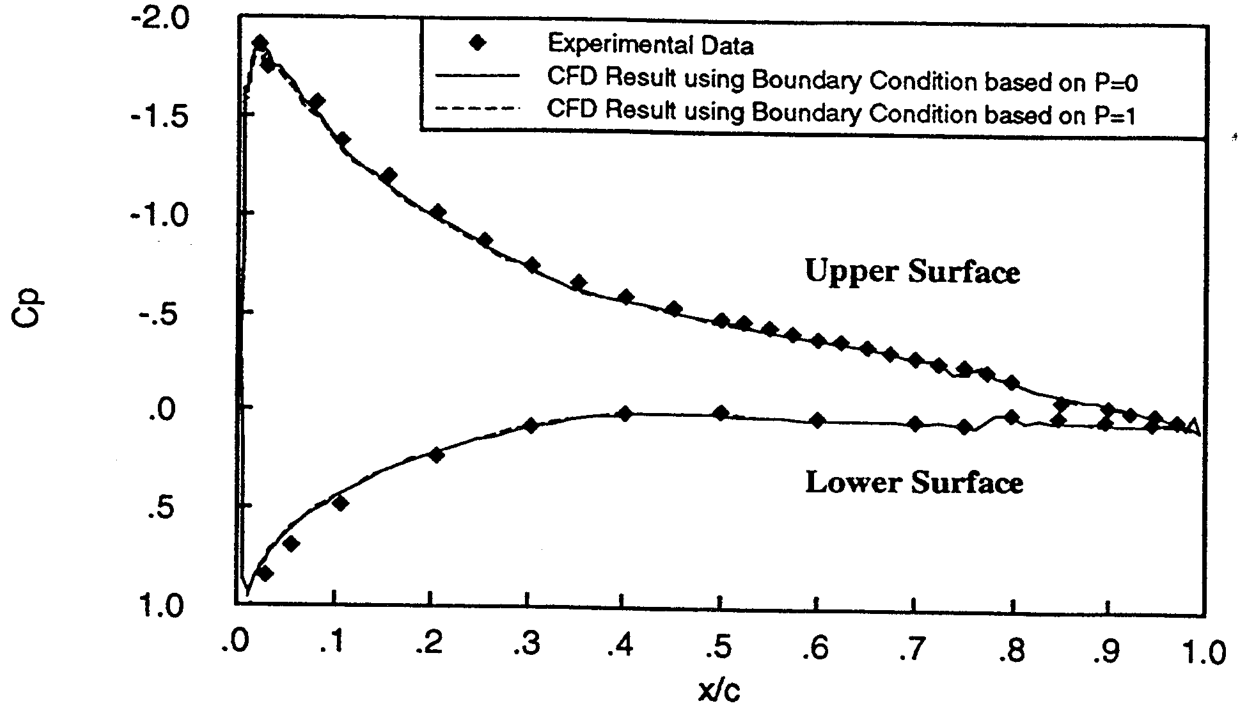

Figure 20. Effect of using boundary conditions based on porosity parameters of P = 0. and P = 1. on computed airfoil pressure profiles for α = 8 degrees. Boundary conditions used are shown in Figure 19.

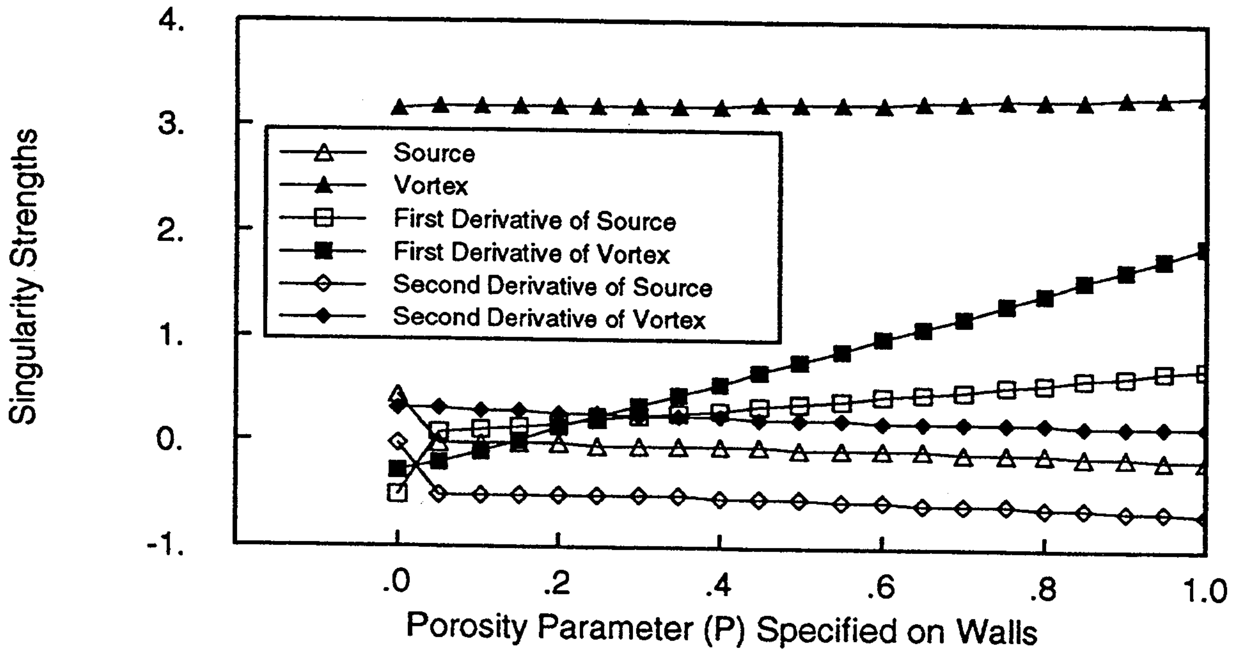

Figure 21. Effect on singularity strengths of changes in porosity parameter specified in method of singularities. Method of singularities solutions were based on α = 8 degrees, porous wall wind tunnel test.

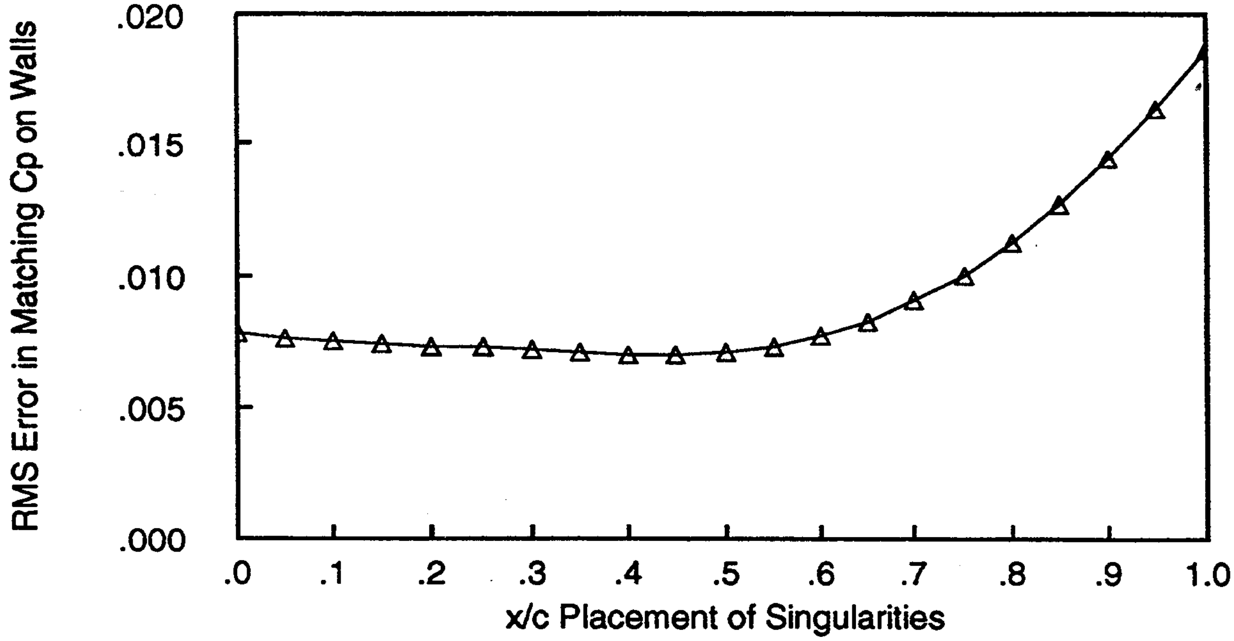

Figure 22. Effect of changes in the position of singularities on the root-mean-square errors in matching pressure profiles for the $\alpha = 8$ degrees, solid wall wind tunnel test.

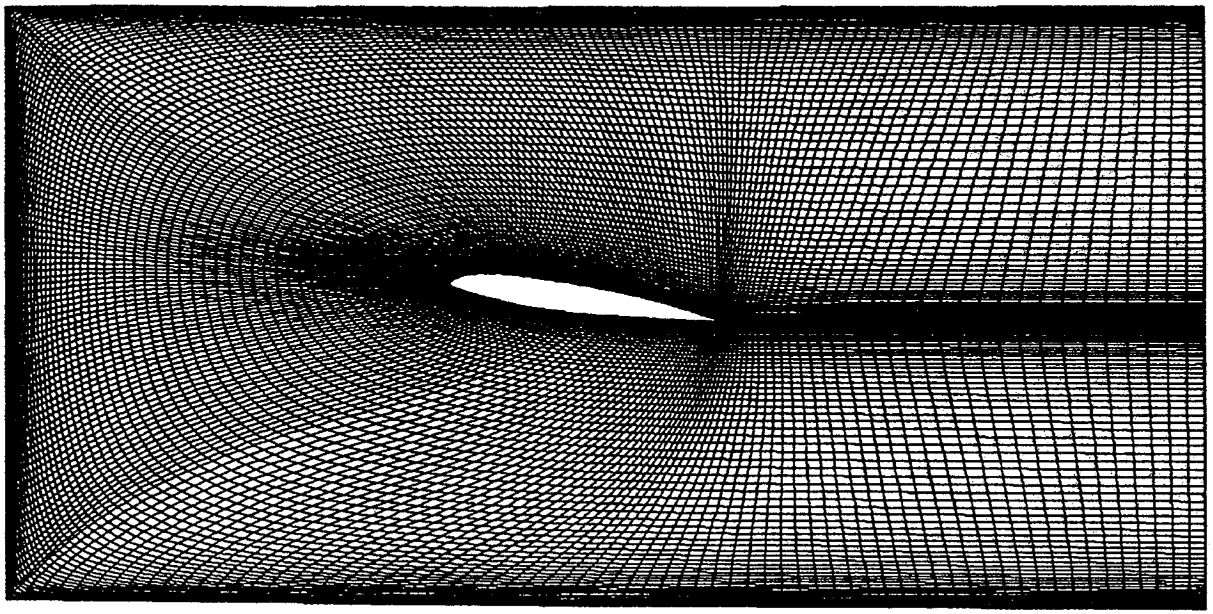

Figure 23. Grid used in the $\alpha = 8$ degrees simulation using viscous wall boundary conditions.

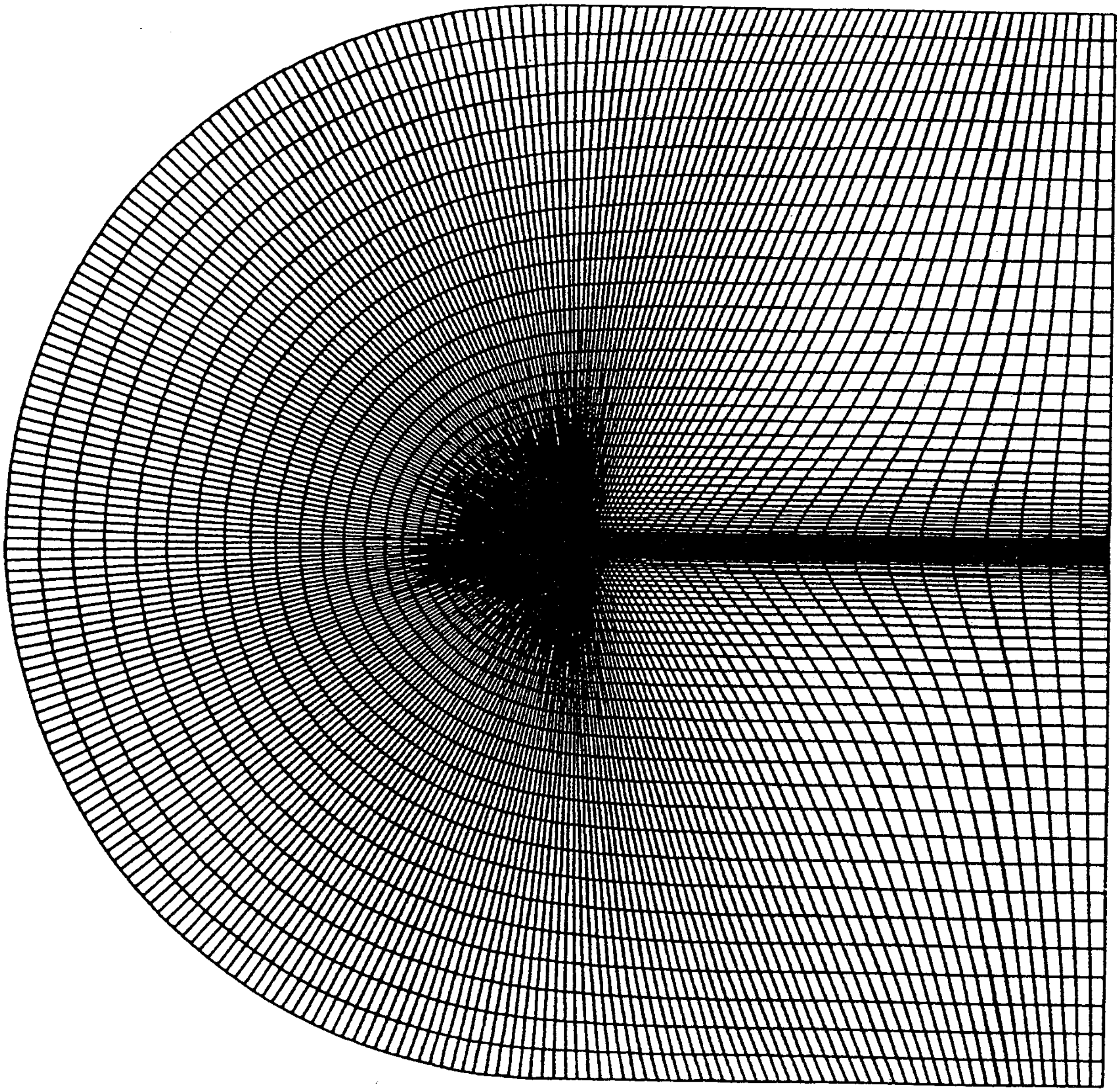

Figure 24. Grid used in the free-air simulations.

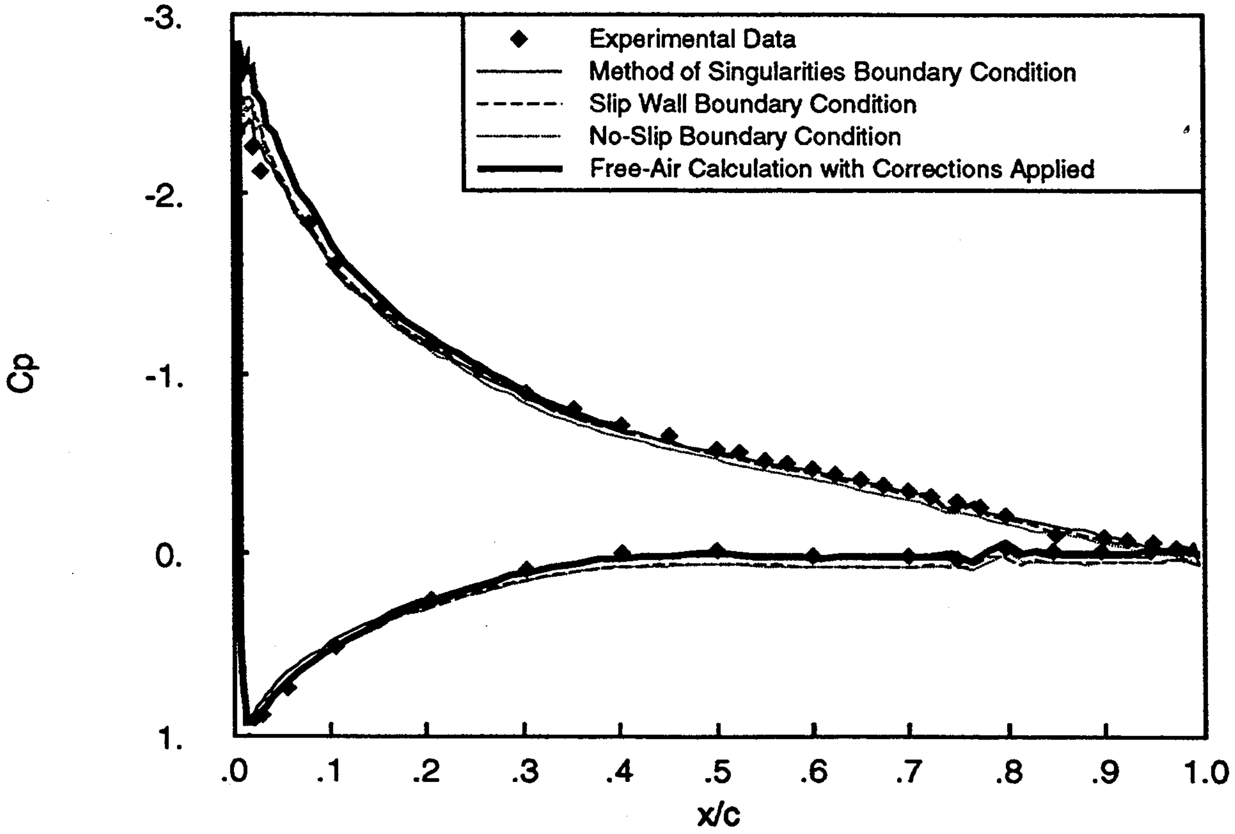

Figure 25. Pressure profiles on the airfoil from CFD calculations using specified pressure, no slip wall, viscous wall and free-air boundary conditions.

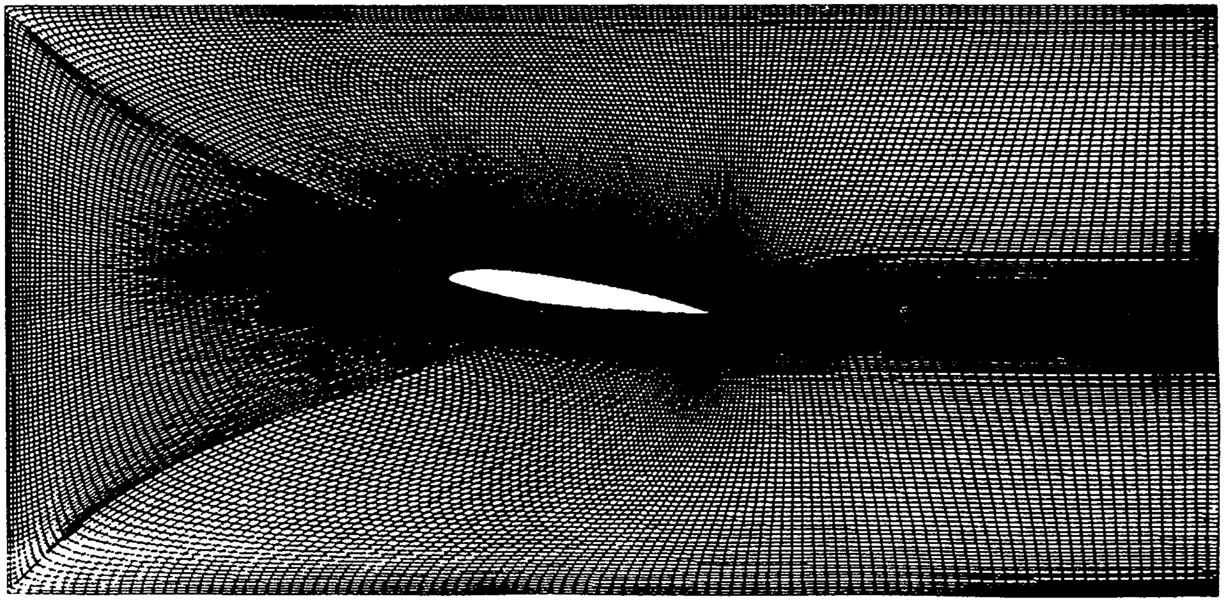

Figure 26. Refined grid for $\alpha = 8$ degrees test case. Grid dimensions are 350 x 105.

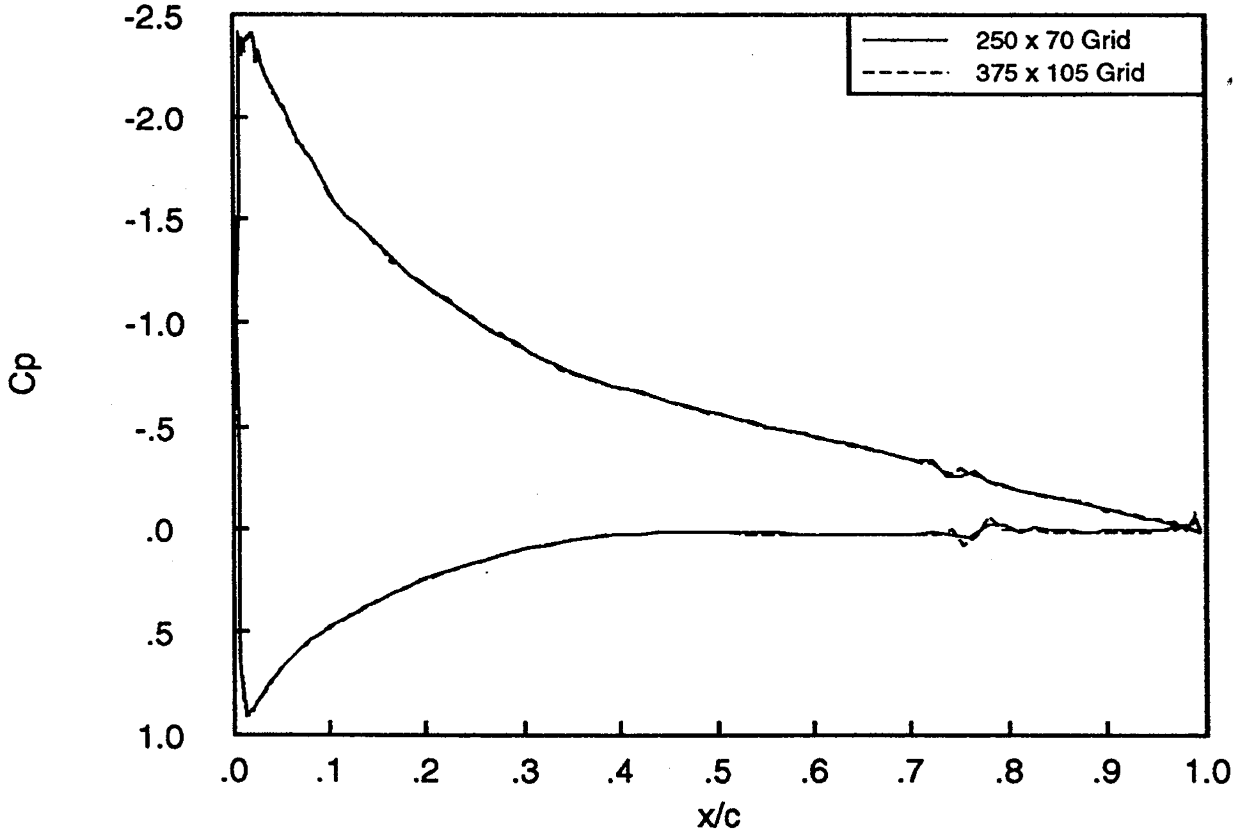

Figure 27. Comparison of results from 250 x 70 grid and 350 x 105 grid. Results are for solid wall test at $\alpha = 8$ degrees.

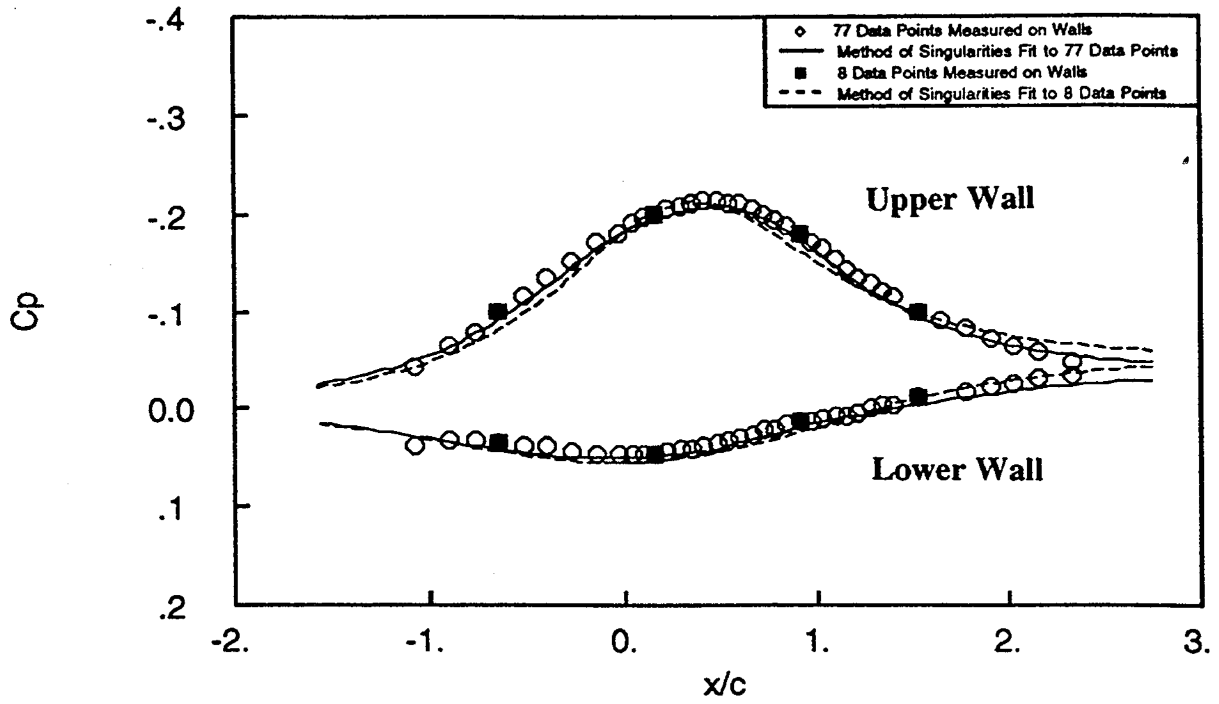

Figure 28a. Comparison of method of singularities fit to complete set of data and sparse data on the walls for solid wall test at $\alpha = 5$ degrees.

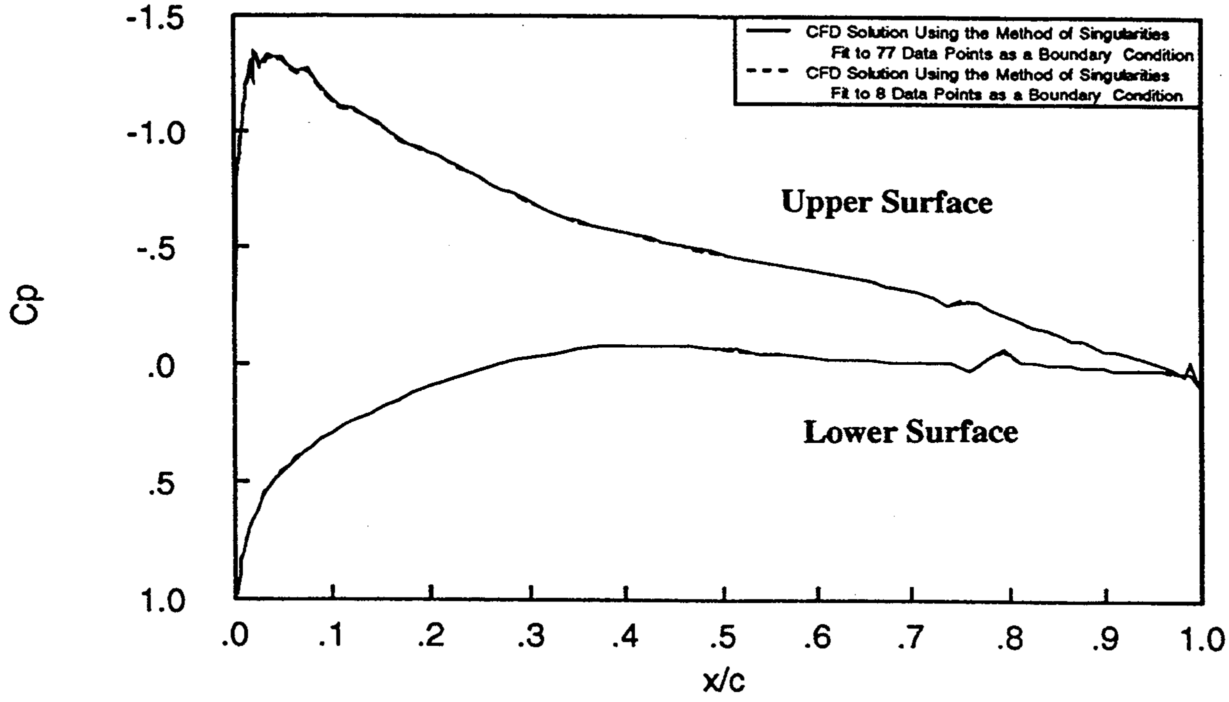

Figure 28b. Comparison of CFD airfoil pressure profiles obtained using the boundary conditions developed from sparse and fine data, shown in Figure 28a.

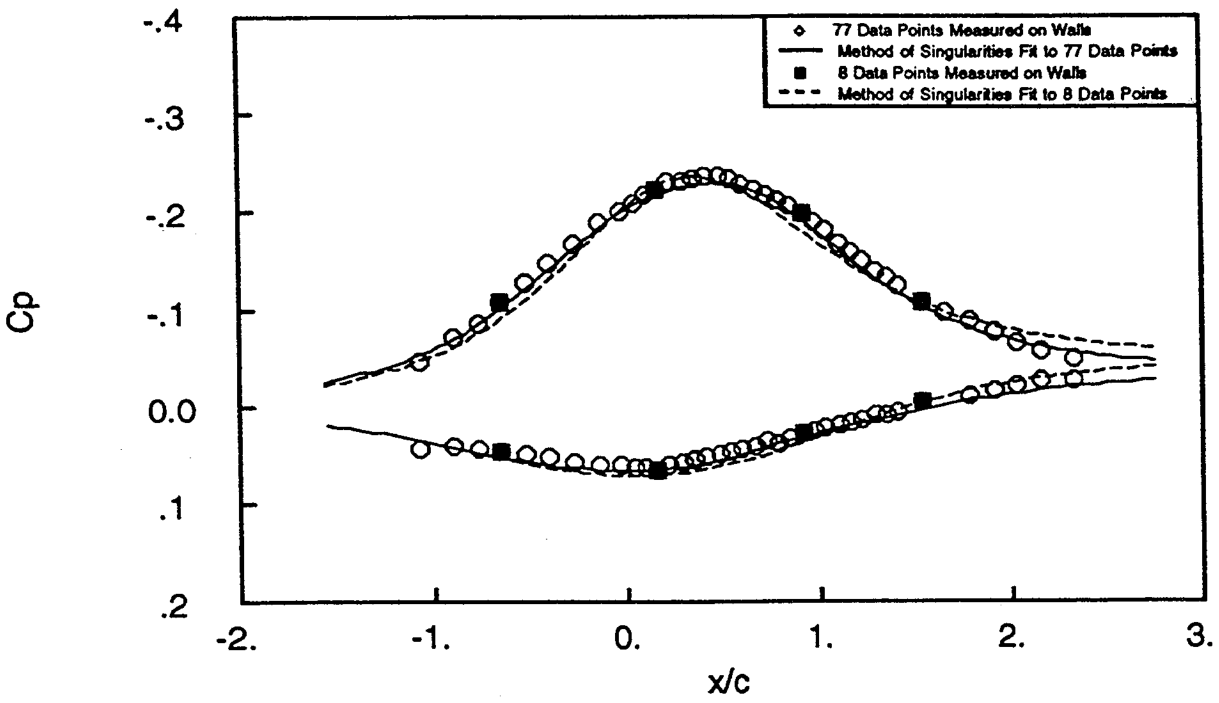

Figure 29a. Comparison of method of singularities fit to complete set of data and sparse data on the walls for solid wall test at $\alpha = 6$ degrees.

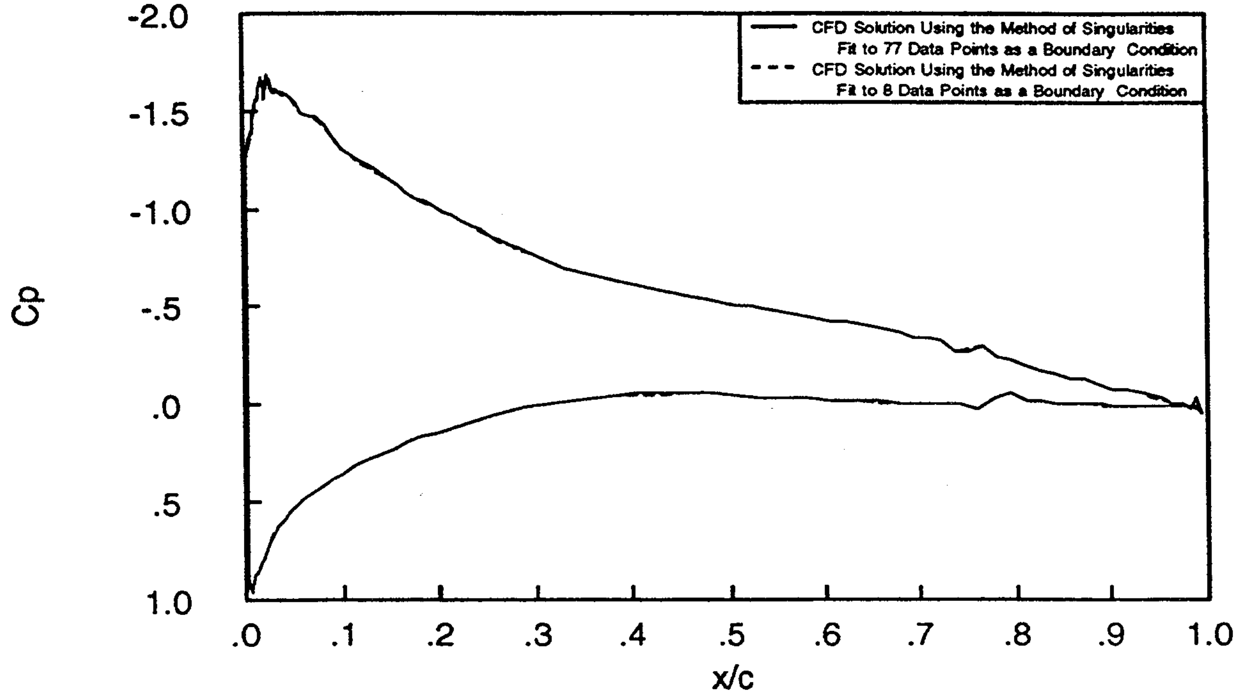

Figure 29b. Comparison of CFD airfoil pressure profiles obtained using the boundary conditions developed from sparse and fine data, shown in Figure 29a.

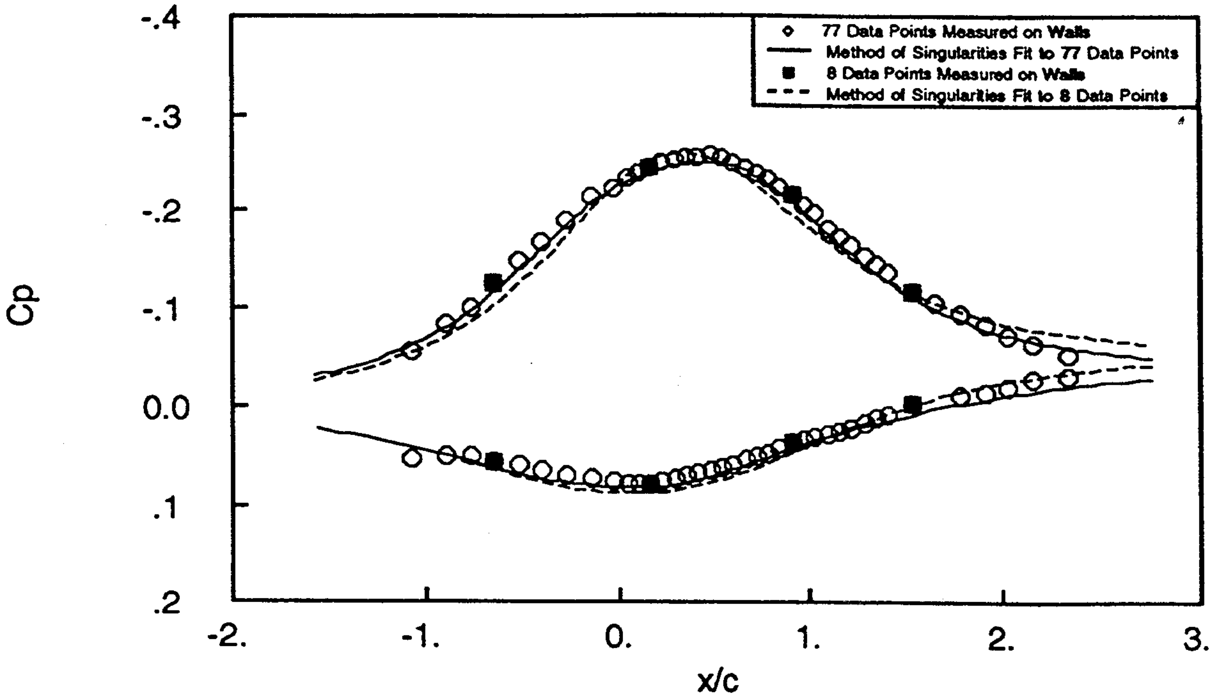

Figure 30a. Comparison of method of singularities fit to complete set of data and sparse data on the walls for solid wall test at $\alpha = 7$ degrees.

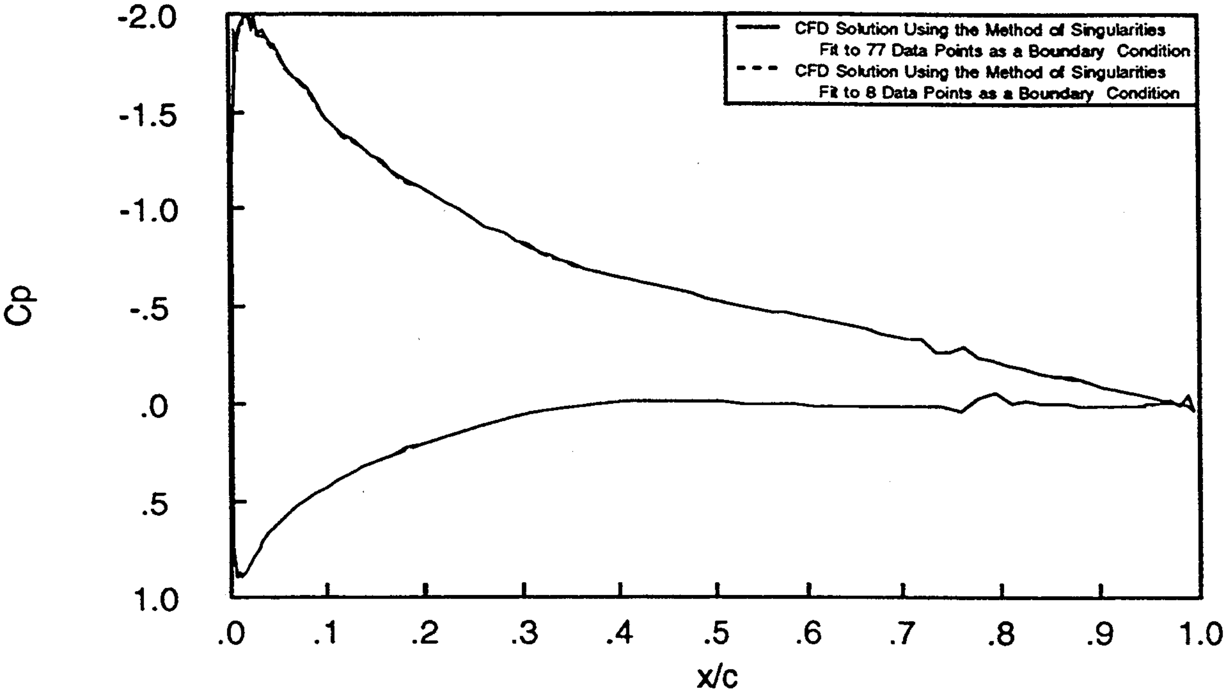

Figure 30b. Comparison of CFD airfoil pressure profiles obtained using the boundary conditions developed from sparse and fine data, shown in Figure 30a.

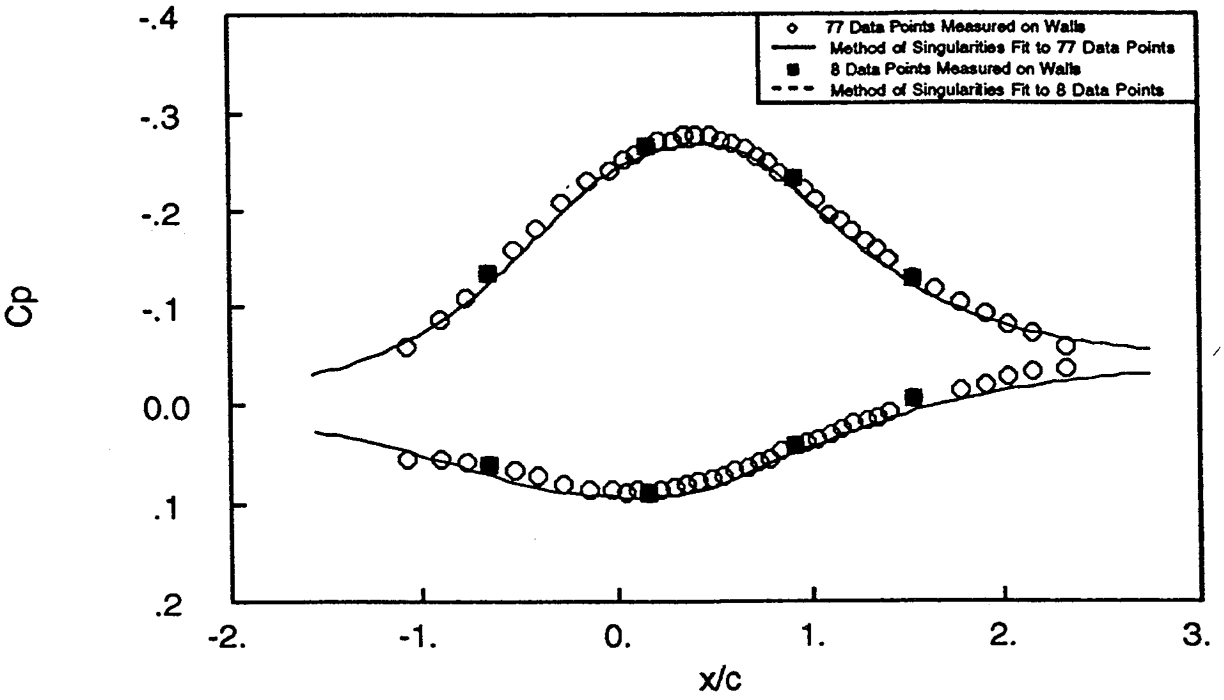

Figure 31a. Comparison of method of singularities fit to complete set of data and sparse data on the walls for solid wall test at $\alpha = 8$ degrees.

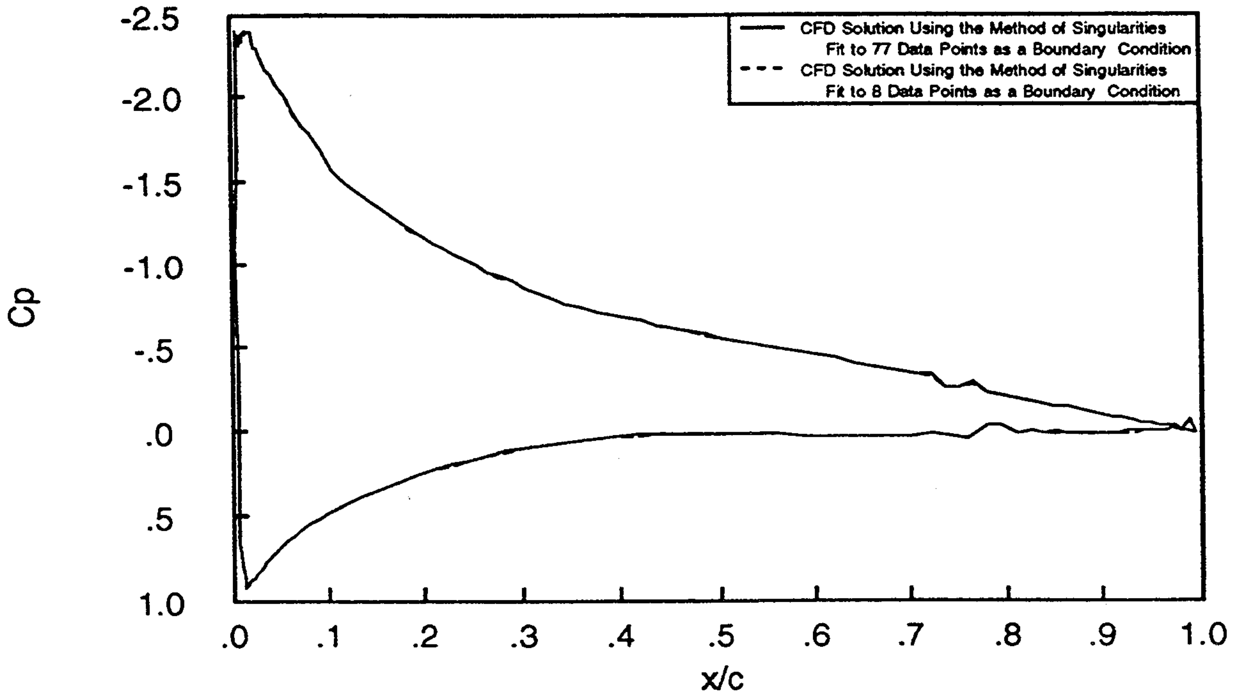

Figure 31b. Comparison of CFD airfoil pressure profiles obtained using the boundary conditions developed from sparse and fine data, shown in Figure 31a.

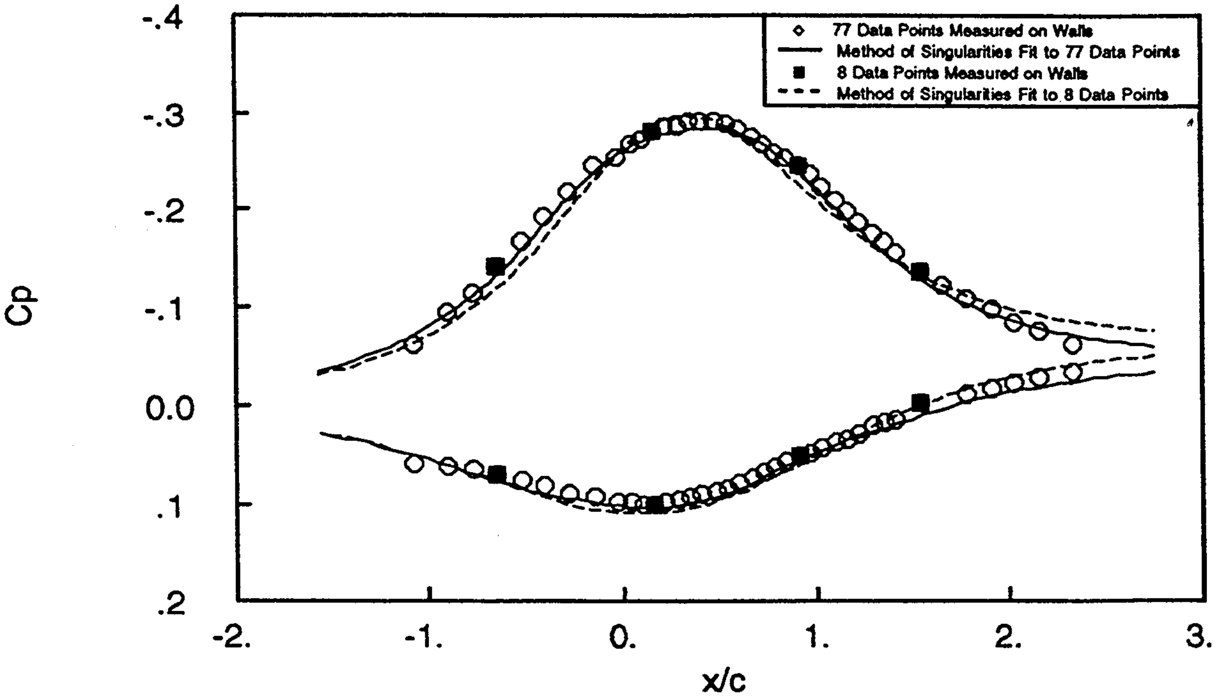

Figure 32a. Comparison of method of singularities fit to complete set of data and sparse data on the walls for solid wall test at $\alpha = 9$ degrees.

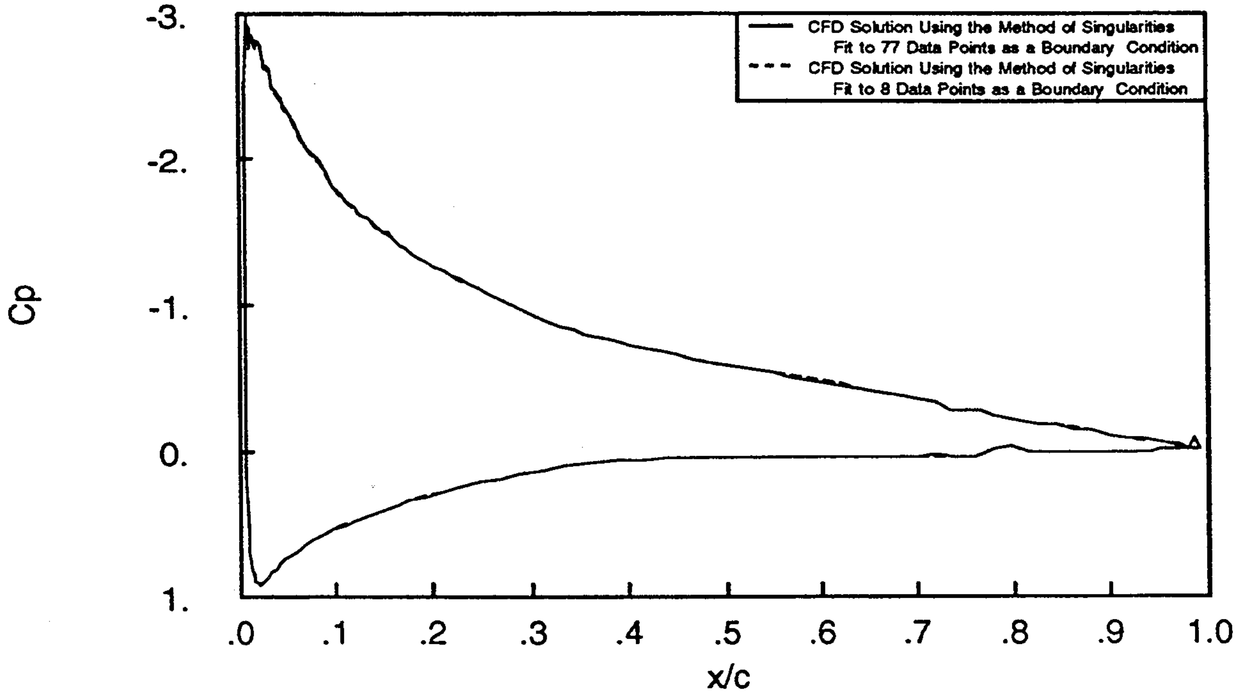

Figure 32b. Comparison of CFD airfoil pressure profiles obtained using the boundary conditions developed from sparse and fine data, shown in Figure 32a.

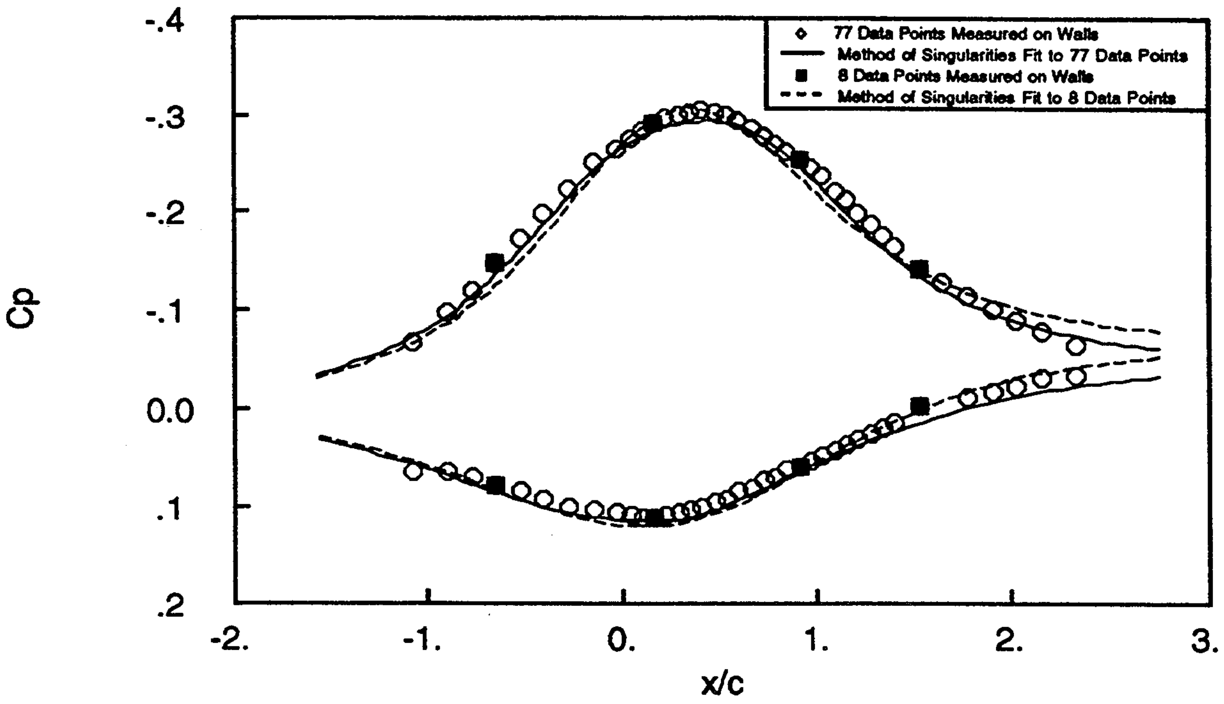

Figure 33a. Comparison of method of singularities fit to complete set of data and sparse data on the walls for solid wall test at $\alpha = 10$ degrees.

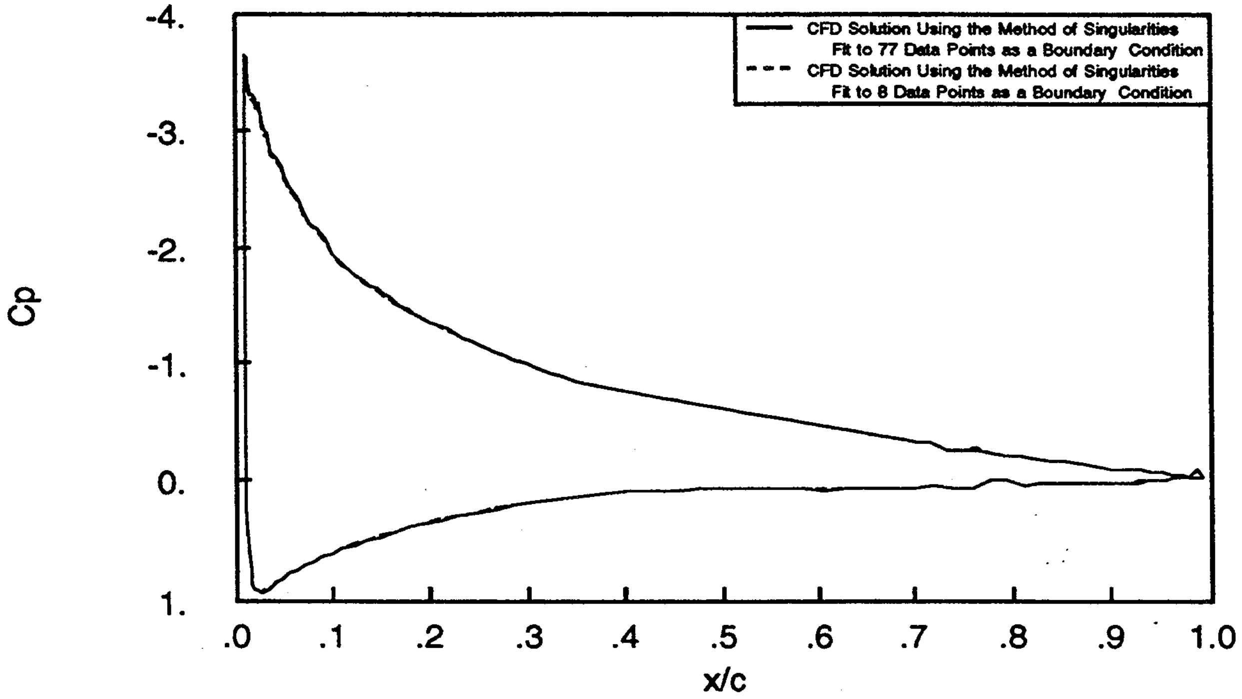

Figure 33b. Comparison of CFD airfoil pressure profiles obtained using the boundary conditions developed from sparse and fine data, shown in Figure 33a.

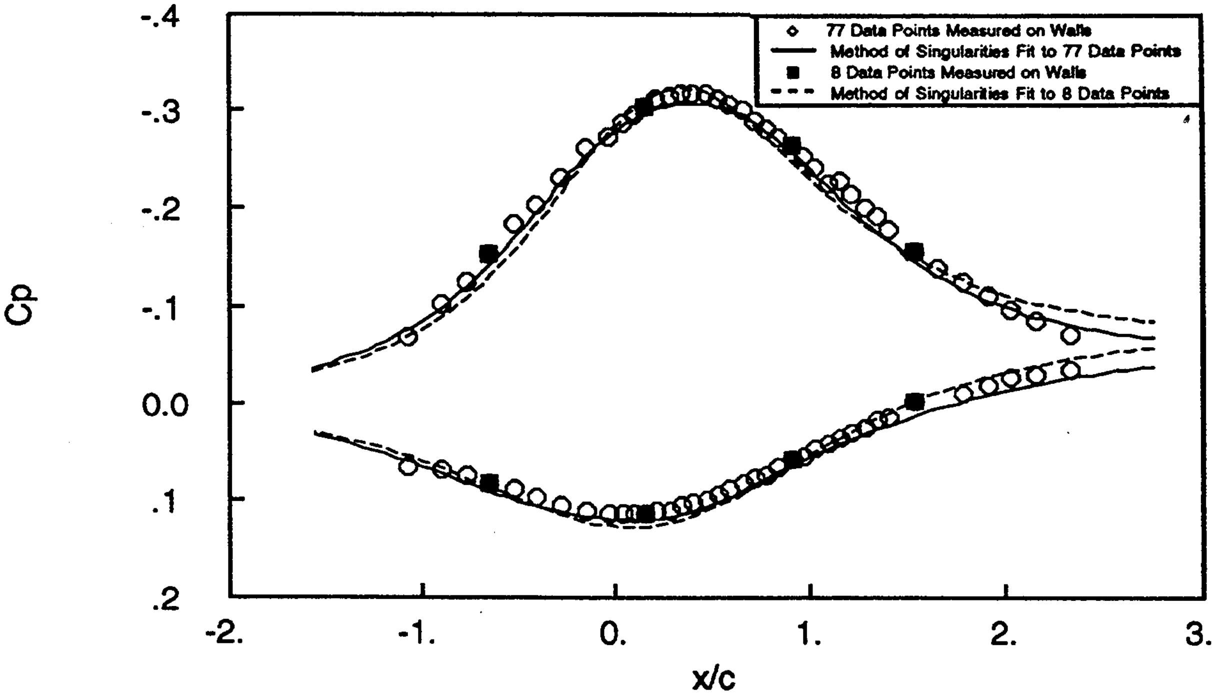

Figure 34a. Comparison of method of singularities fit to complete set of data and sparse data on the walls for solid wall test at α = 11 degrees.

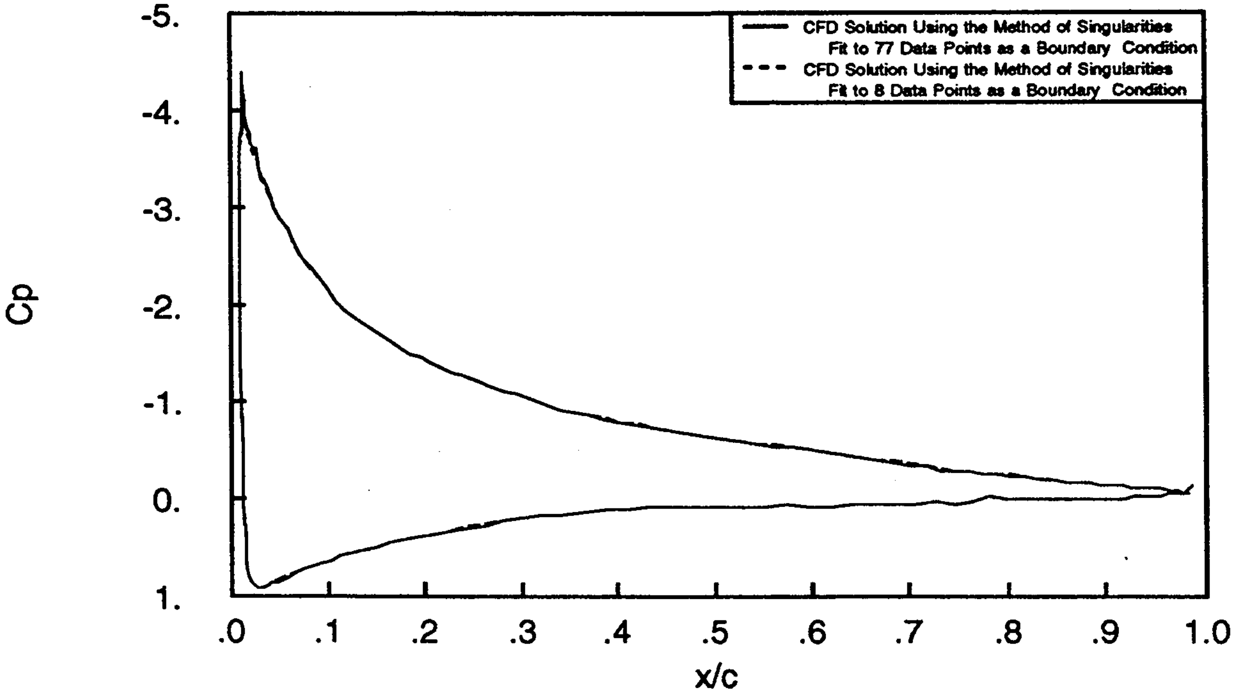

Figure 34b. Comparison of CFD airfoil pressure profiles obtained using the boundary conditions developed from sparse and fine data, shown in Figure 34a.

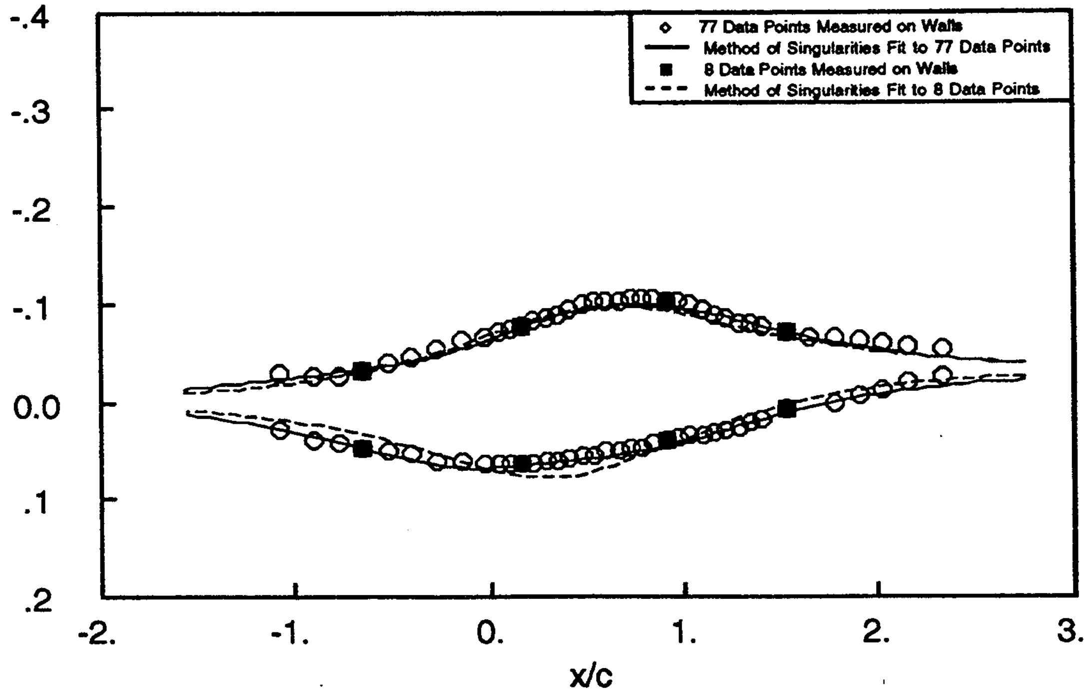

Figure 35a. Comparison of method of singularities fit to complete set of data and sparse data on the walls for porous wall test at $\alpha = 5$ degrees.

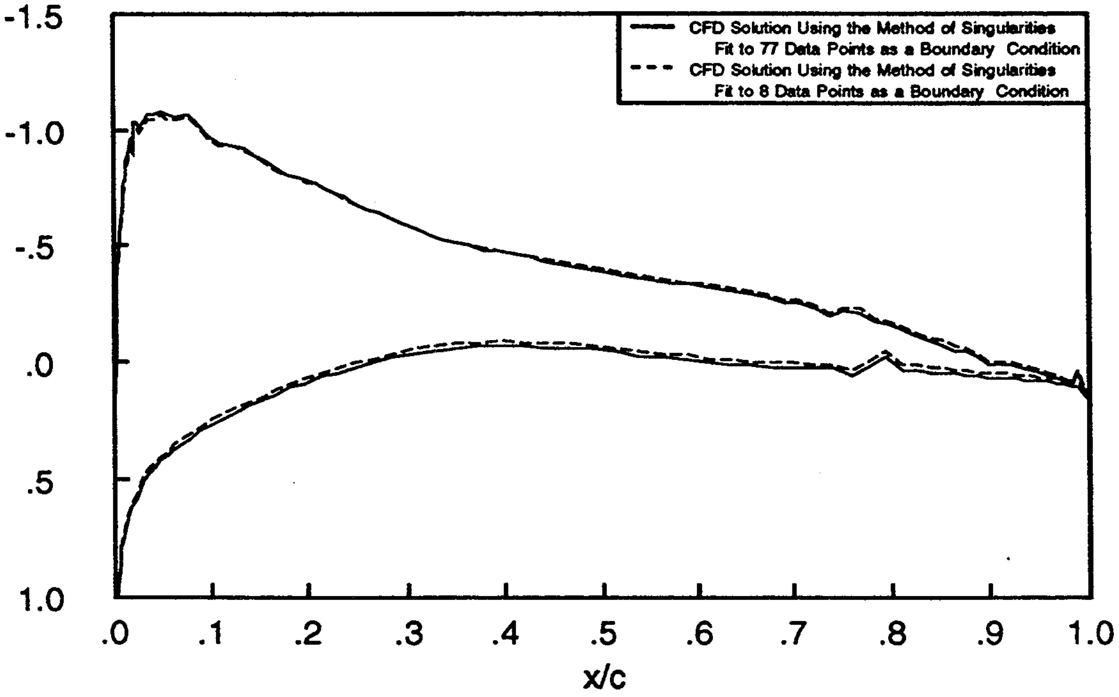

Figure 35b. Comparison of CFD airfoil pressure profiles obtained using the boundary conditions developed from sparse and fine data, shown in Figure 35a.

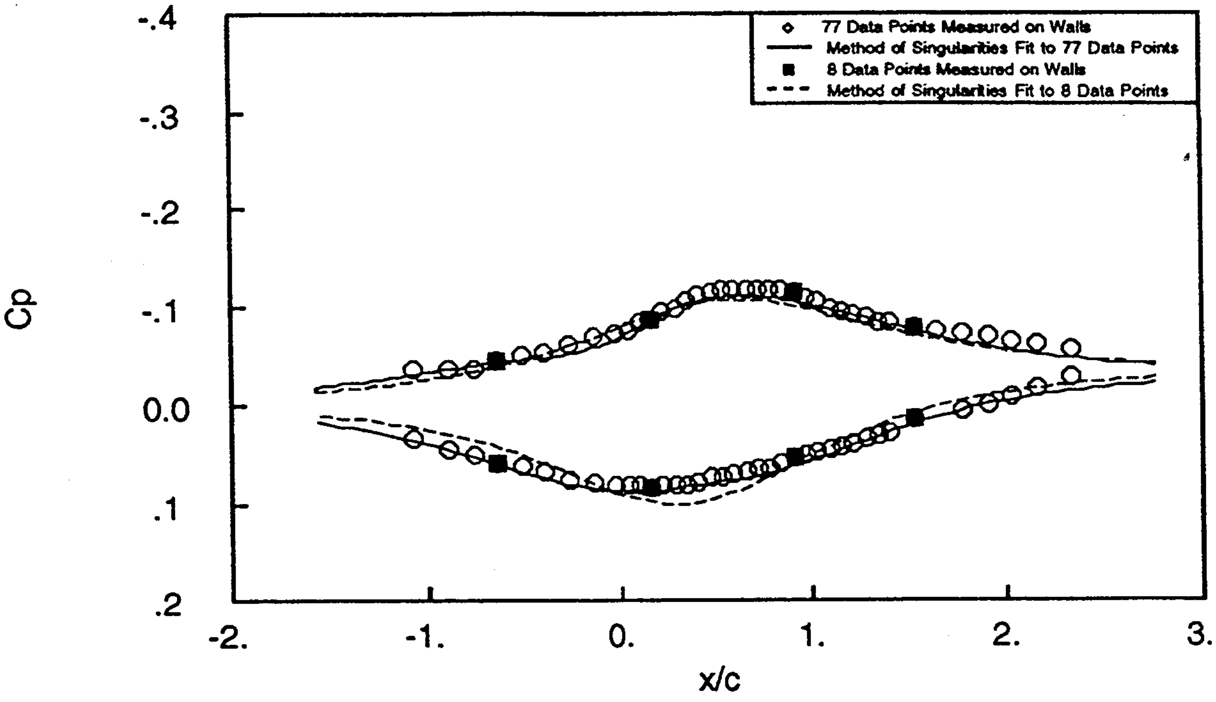

Figure 36a. Comparison of method of singularities fit to complete set of data and sparse data on the walls for porous wall test at $\alpha = 6$ degrees.

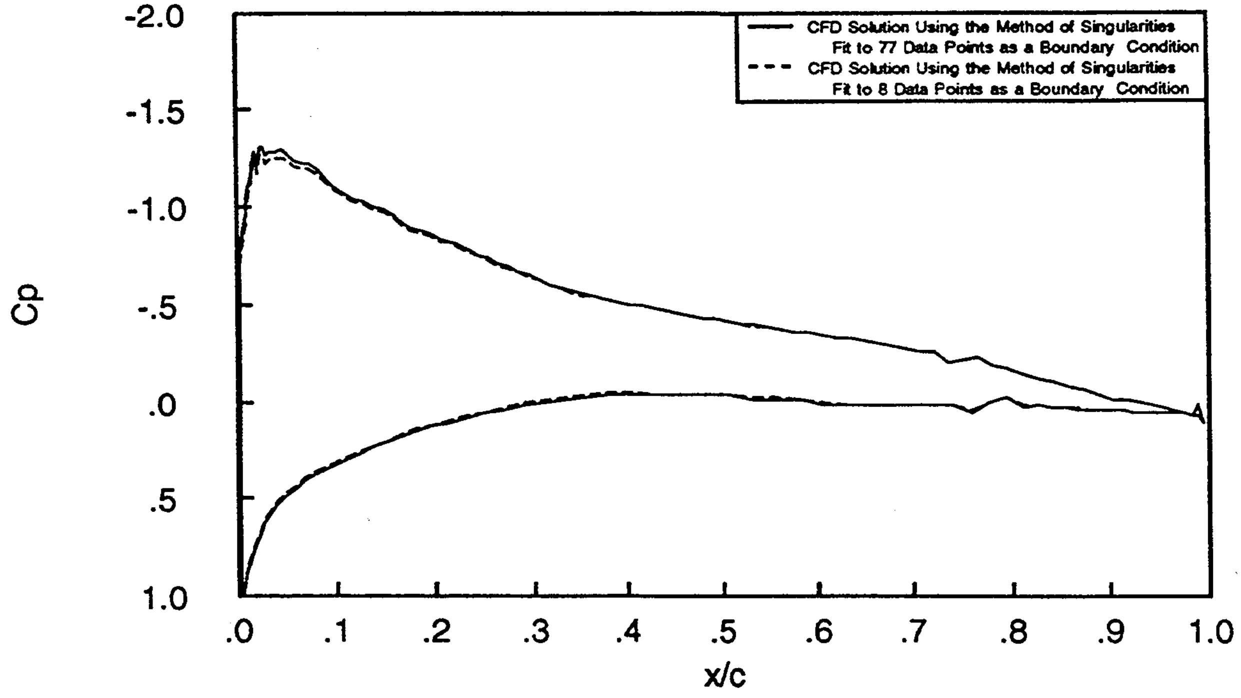

Figure 36b. Comparison of CFD airfoil pressure profiles obtained using the boundary conditions developed from sparse and fine data, shown in Figure 36a.

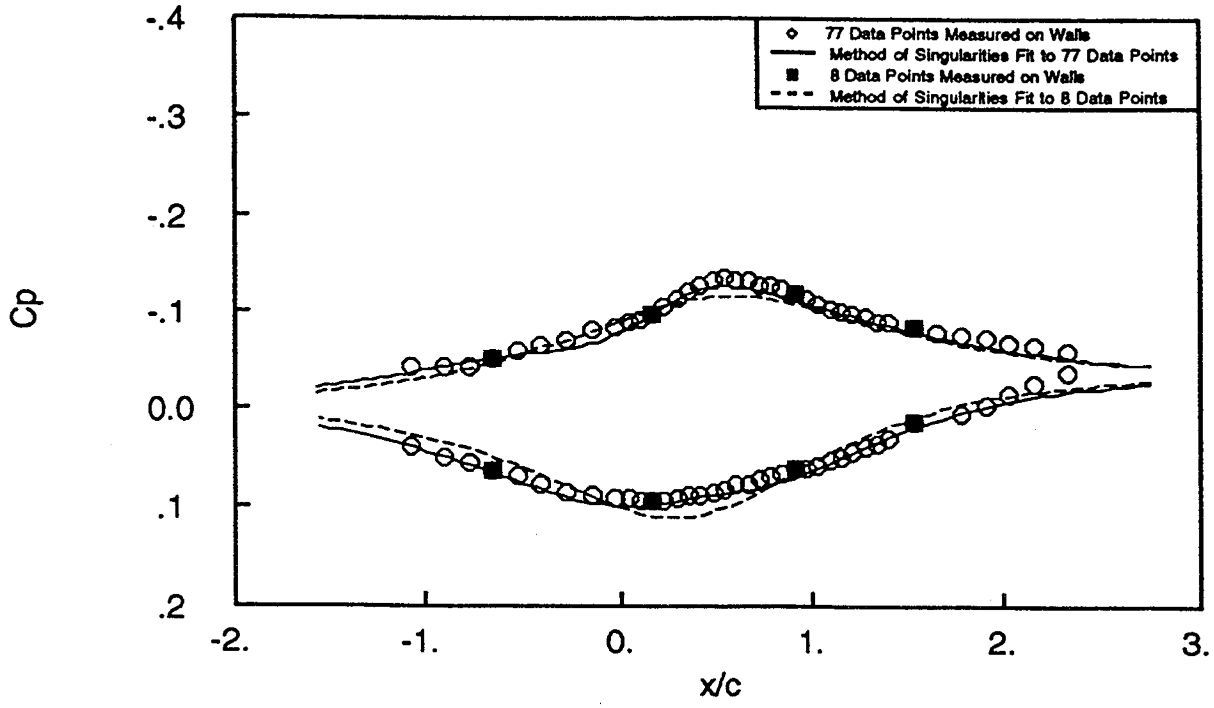

Figure 37a. Comparison of method of singularities fit to complete set of data and sparse data on the walls for porous wall test at $\alpha = 7$ degrees.

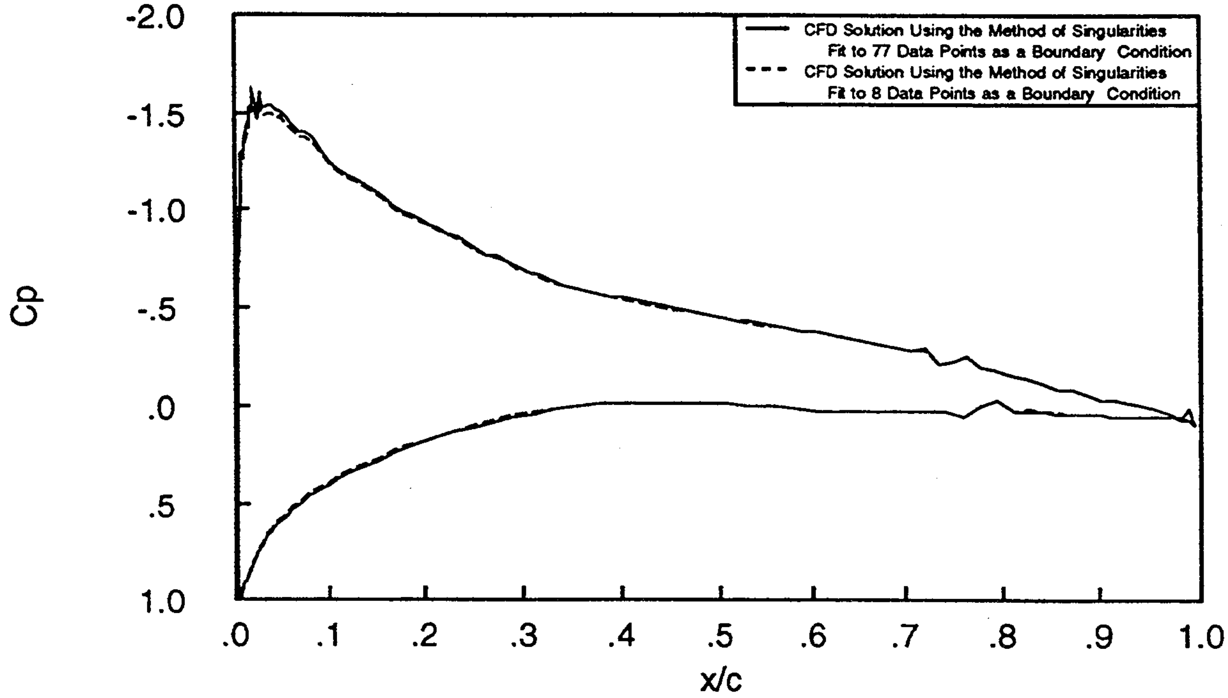

Figure 37b. Comparison of CFD airfoil pressure profiles obtained using the boundary conditions developed from sparse and fine data, shown in Figure 37a.

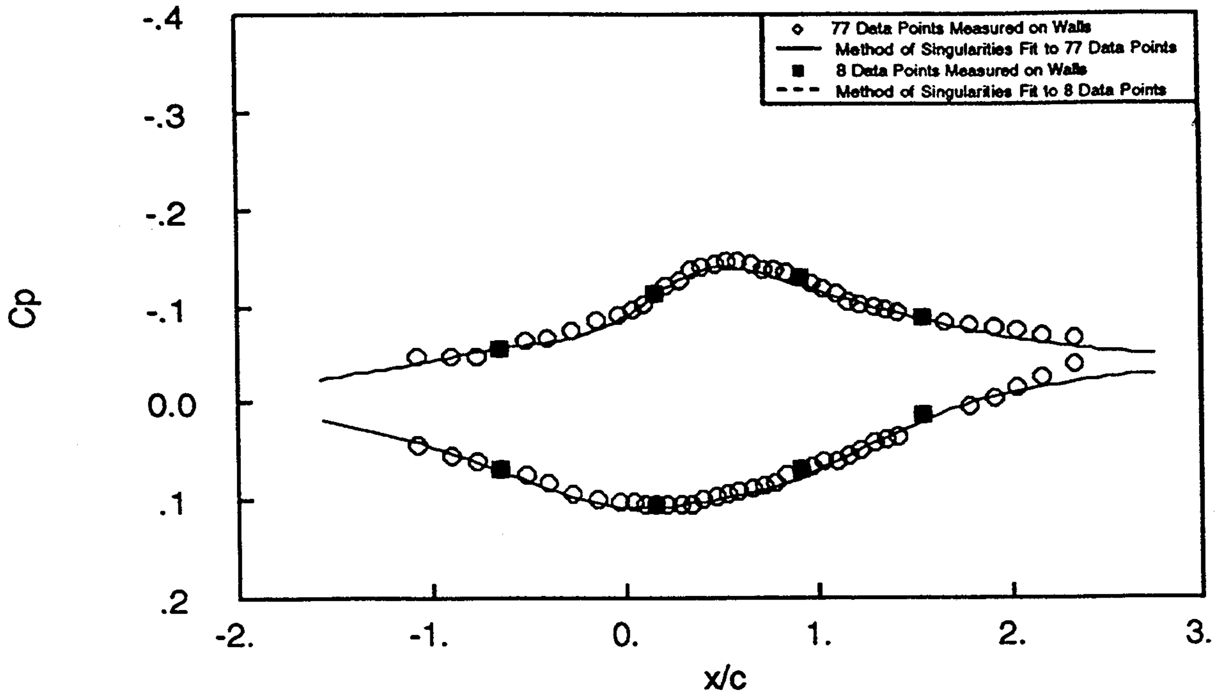

Figure 38a. Comparison of method of singularities fit to complete set of data and sparse data on the walls for porous wall test at $\alpha = 8$ degrees.

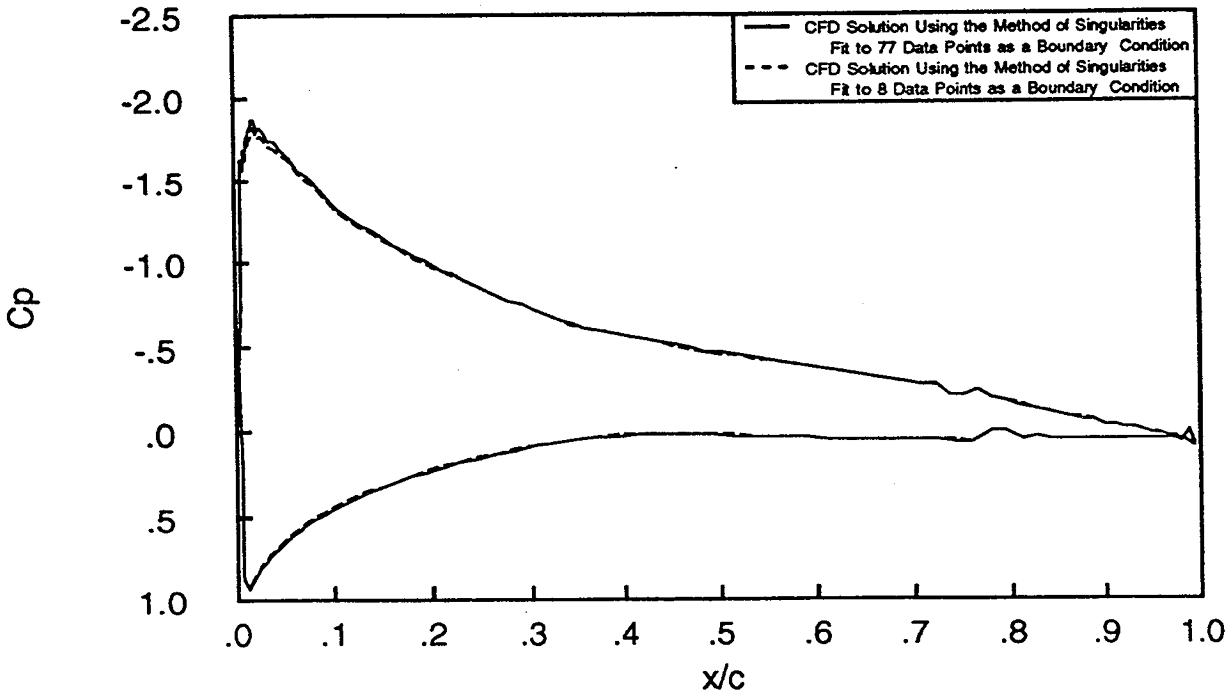

Figure 38b. Comparison of CFD airfoil pressure profiles obtained using the boundary conditions developed from sparse and fine data, shown in Figure 38a.

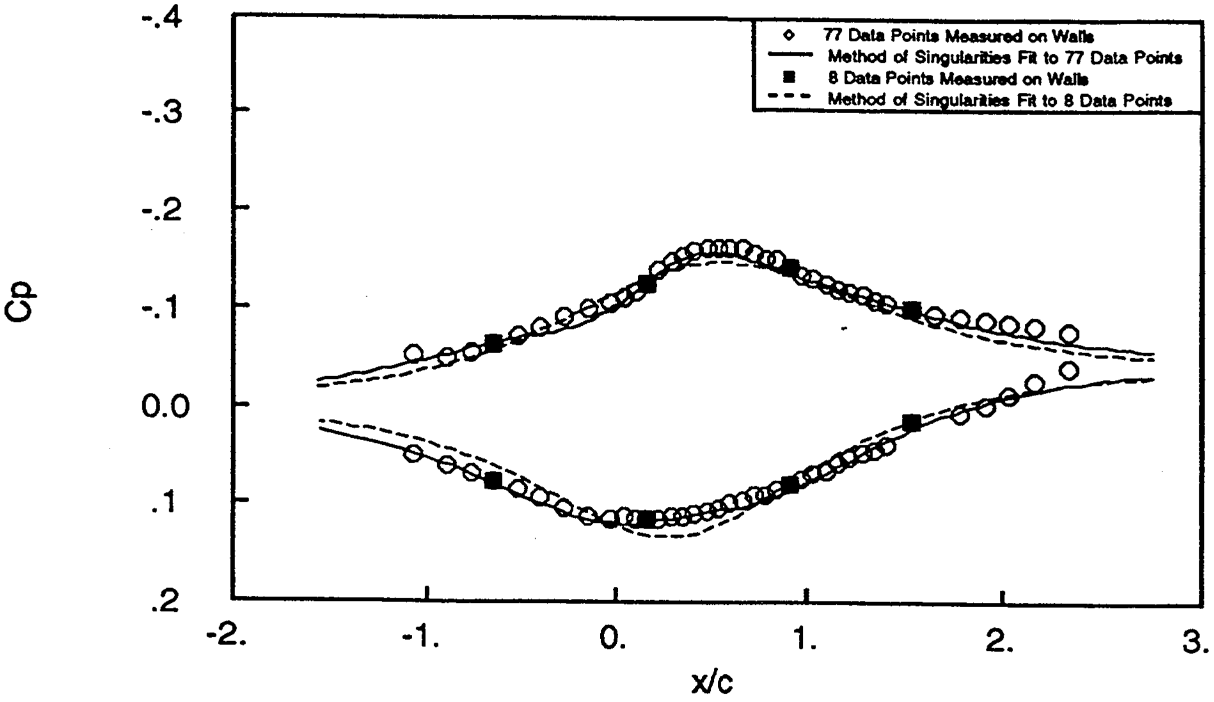

Figure 39a. Comparison of method of singularities fit to complete set of data and sparse data on the walls for porous wall test at α = 9 degrees.

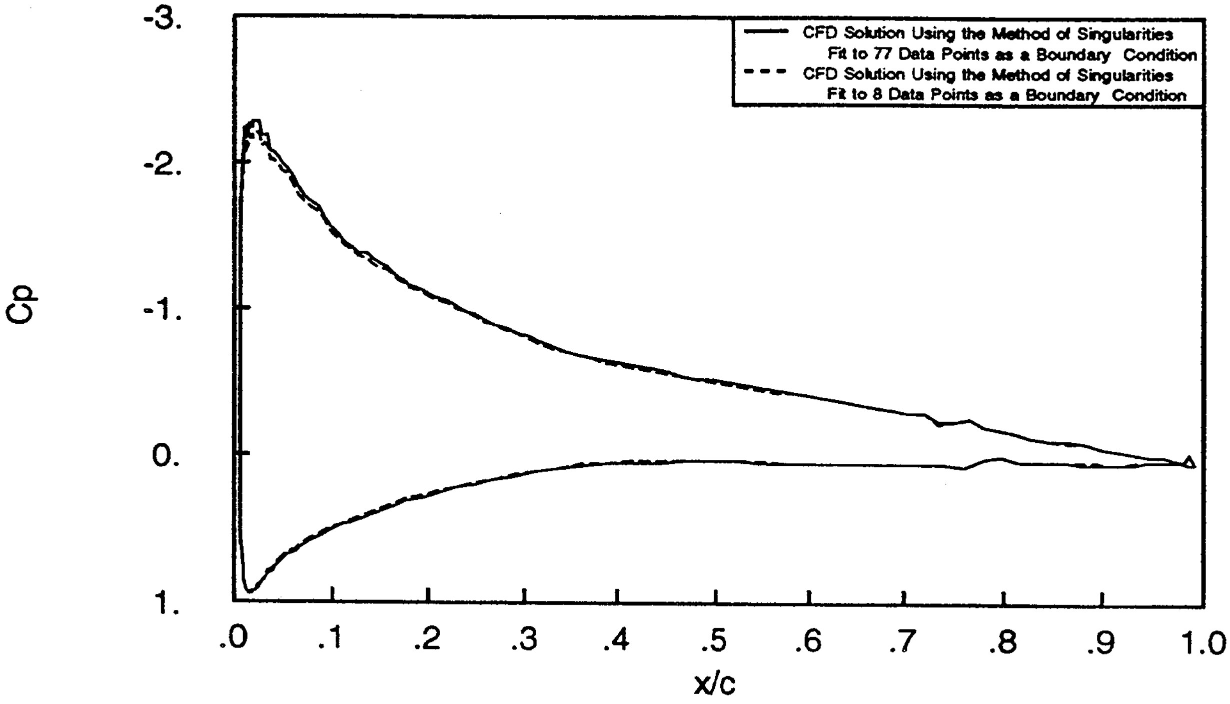

Figure 39b. Comparison of CFD airfoil pressure profiles obtained using the boundary conditions developed from sparse and fine data, shown in Figure 39a.

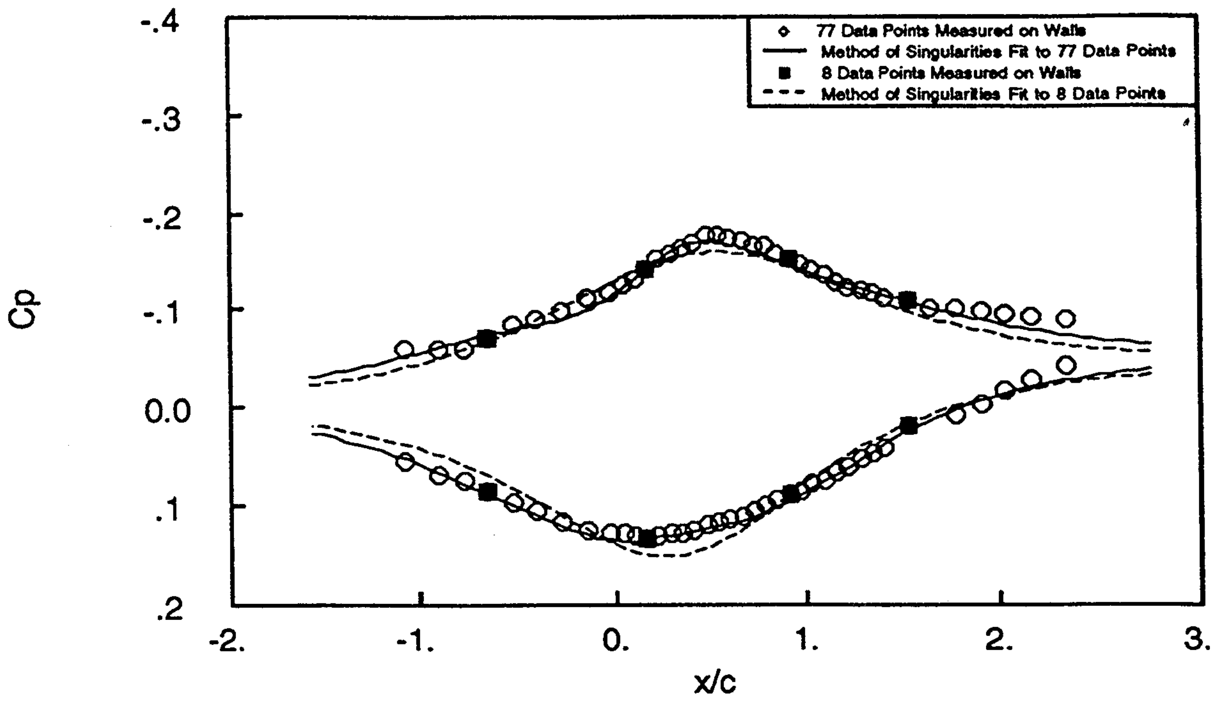

Figure 40a. Comparison of method of singularities fit to complete set of data and sparse data on the walls for porous wall test at $\alpha = 10$ degrees.

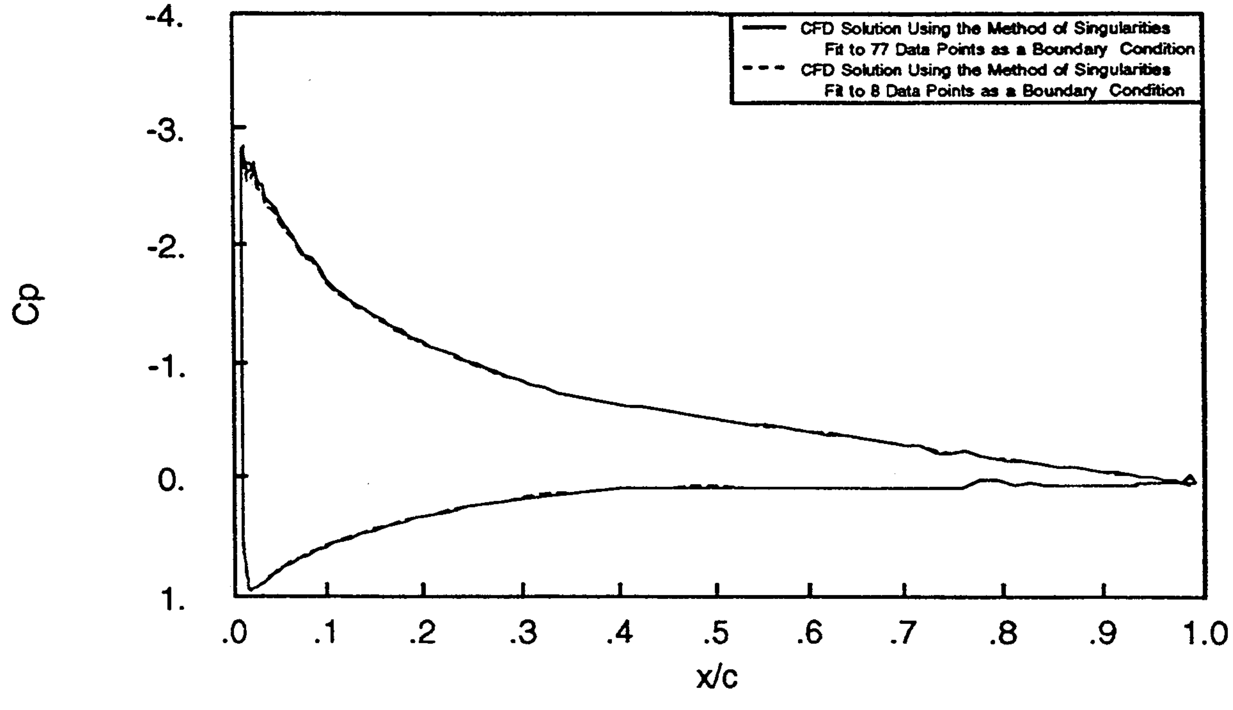

Figure 40b. Comparison of CFD airfoil pressure profiles obtained using the boundary conditions developed from sparse and fine data, shown in Figure 40a.

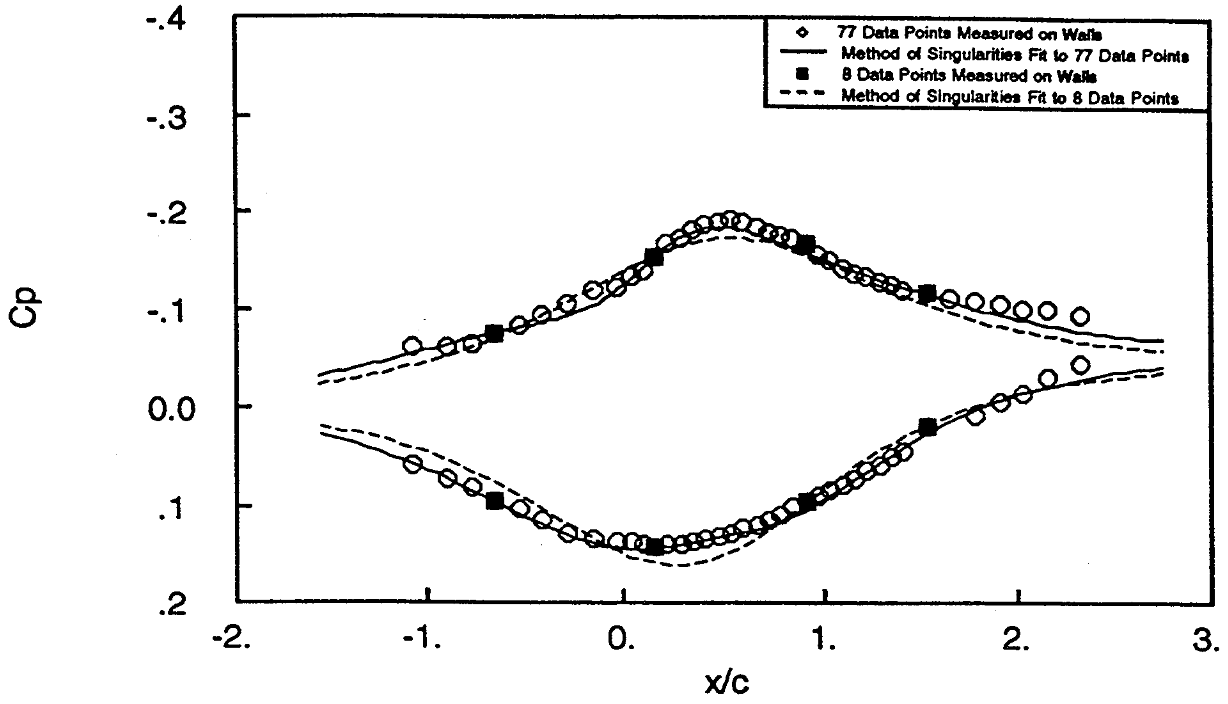

Figure 41a. Comparison of method of singularities fit to complete set of data and sparse data on the walls for porous wall test at α= 11 degrees.

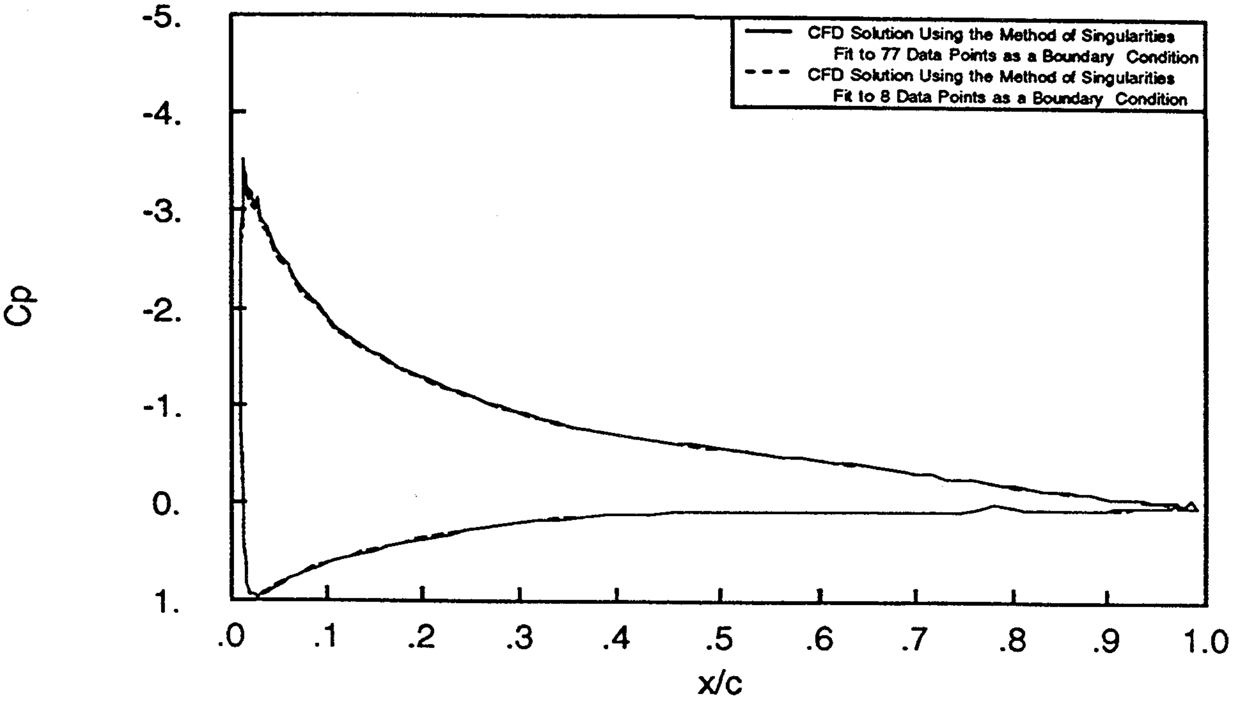

Figure 41b. Comparison of CFD airfoil pressure profiles obtained using the boundary conditions developed from sparse and fine data, shown in Figure 41a.

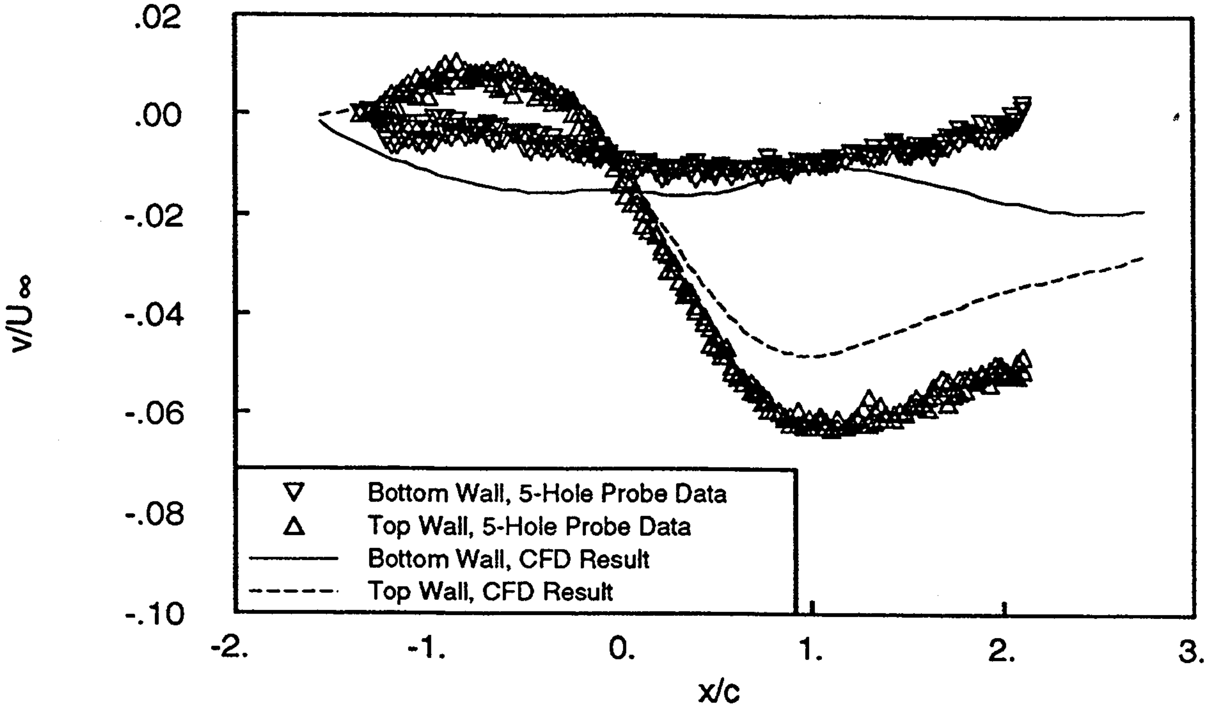

Figure 42. Normal velocities near the walls, as measured by five-hole probe and computed by CFD code. Porous wall tests, $\alpha = 5$ degrees.

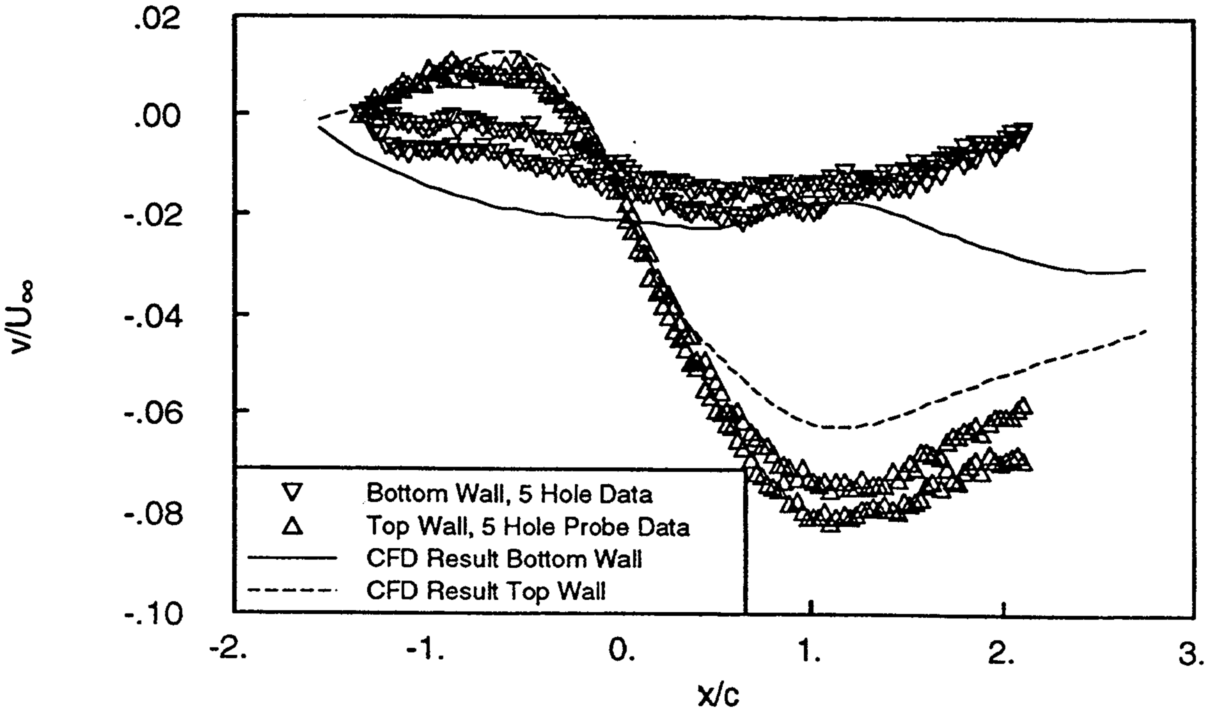

Figure 43. Normal velocities near the walls, as measured by five-hole probe and computed by CFD code. Porous wall tests, $\alpha = 8$ degrees.

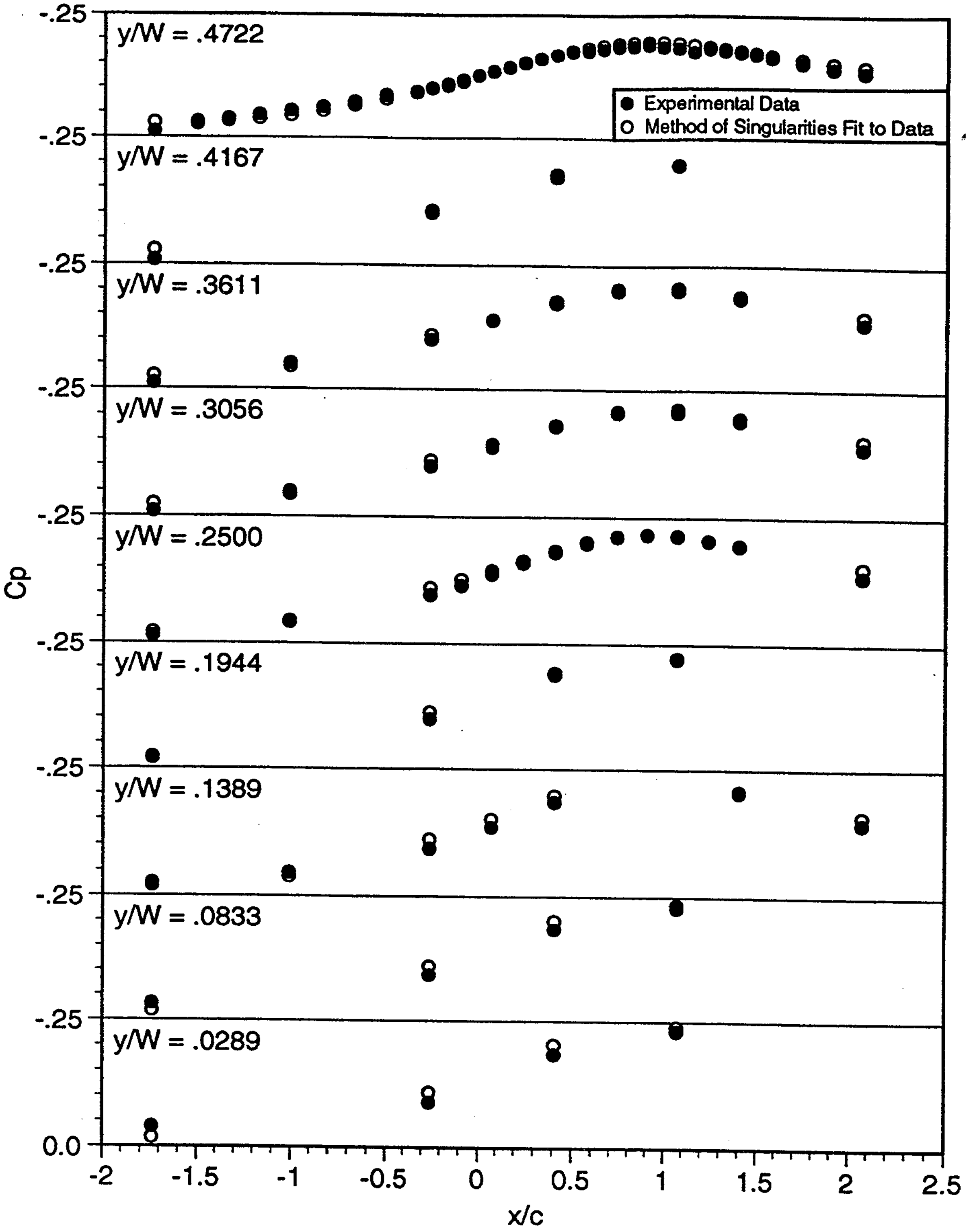

Figure 44a. Upper wall experimental data and method of singularities fit to the experimental data, using 16 singularities and 342 measurements to determine method of singularities solution. U_∞ = 24. m/s, Re = 2.4×10^5, h/c = 3.0, α = 20 degrees. Solid wall boundary condition.

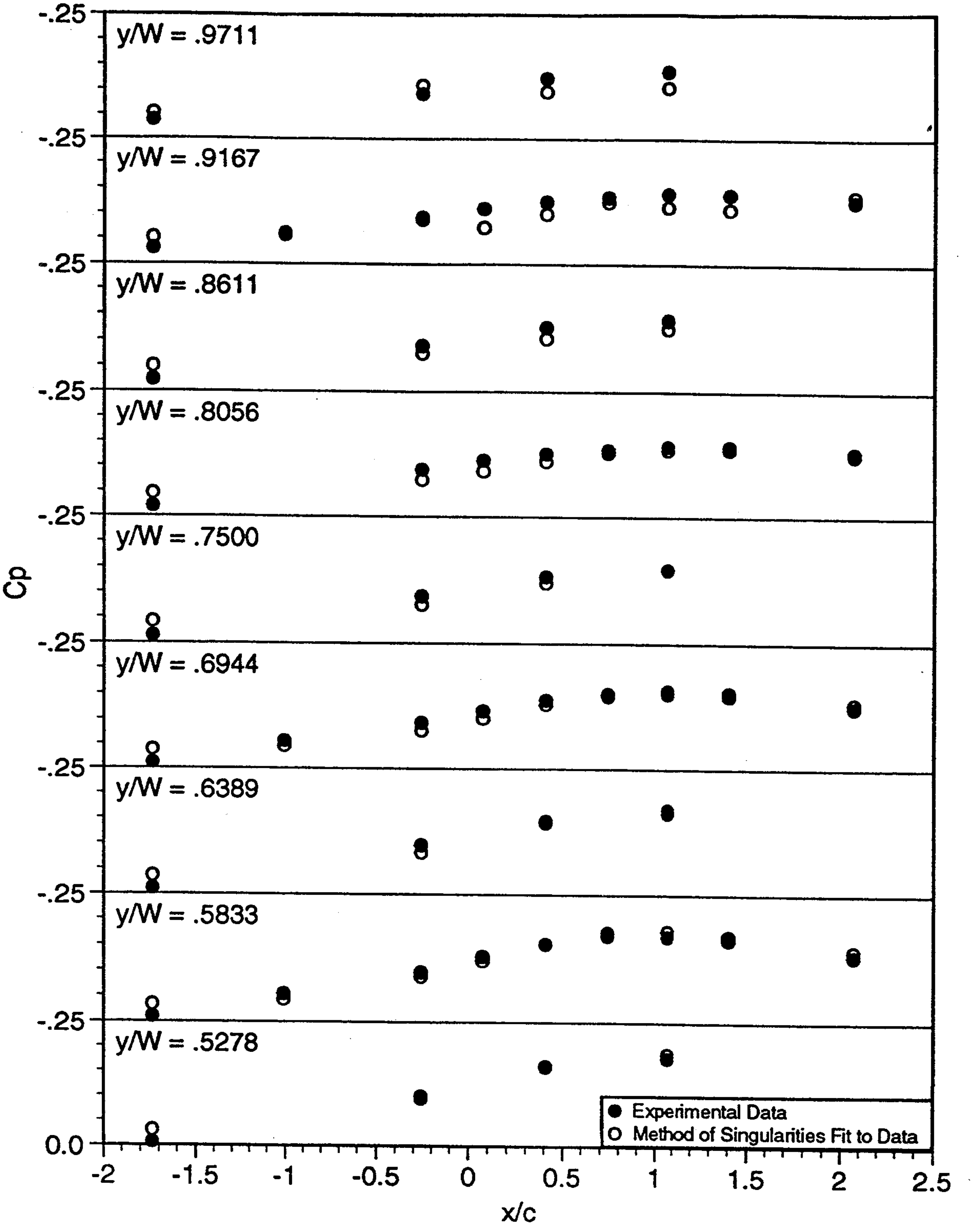

Figure 44b. Upper wall experimental data and method of singularities fit to the experimental data, using 16 singularities and 342 measurements to determine method of singularities solution. $U_\infty = 24.$ m/s, $Re = 2.4 \times 10^5$, $h/c = 3.0$, $\alpha = 20$ degrees. Solid wall boundary condition.

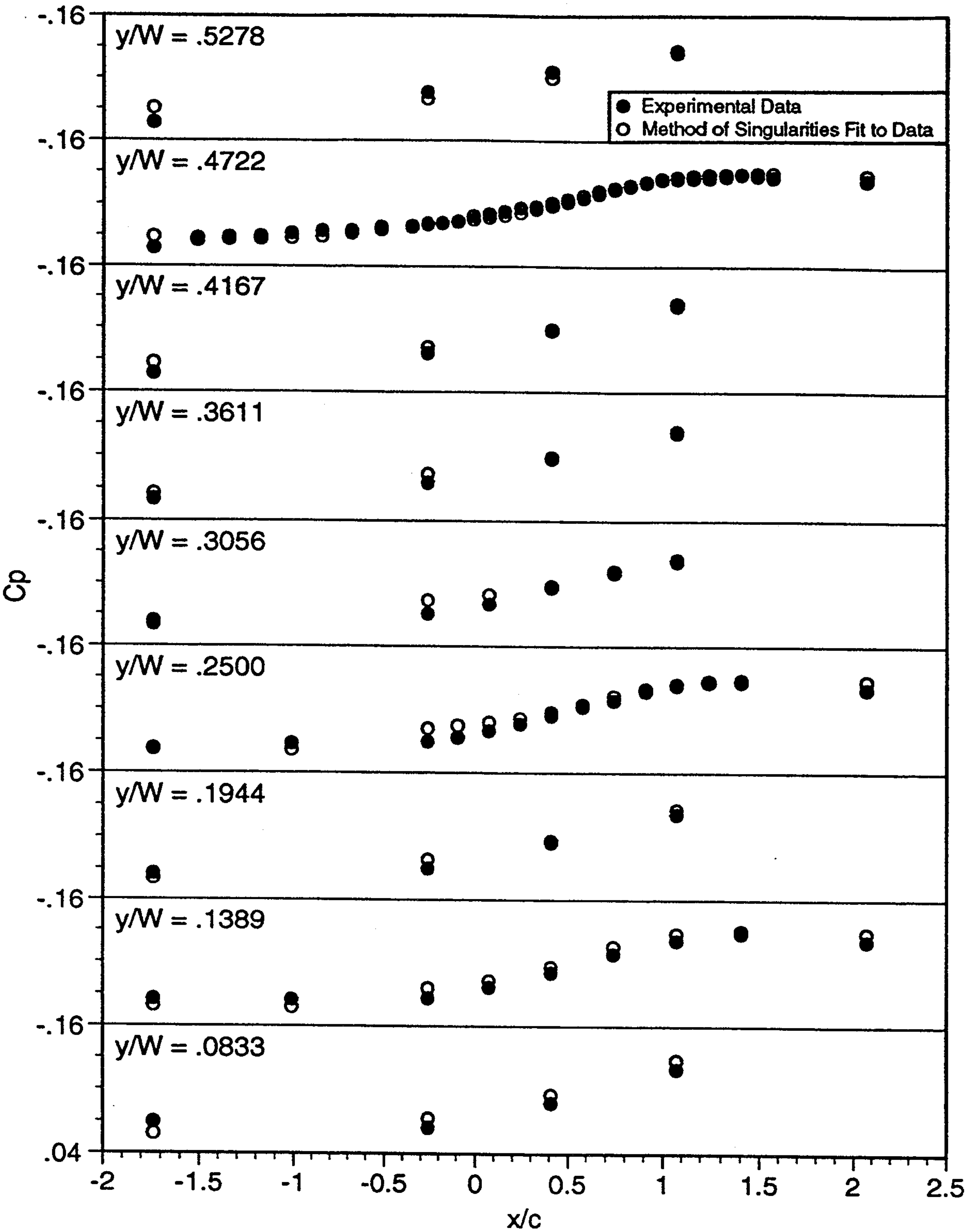

Figure 45a. Lower wall experimental data and method of singularities fit to the experimental data, using 16 singularities and 342 measurements to determine method of singularities solution. $U_\infty = 24.$ m/s, Re $= 2.4 \times 10^5$, h/c = 3.0, $\alpha = 20$ degrees. Solid wall boundary condition.

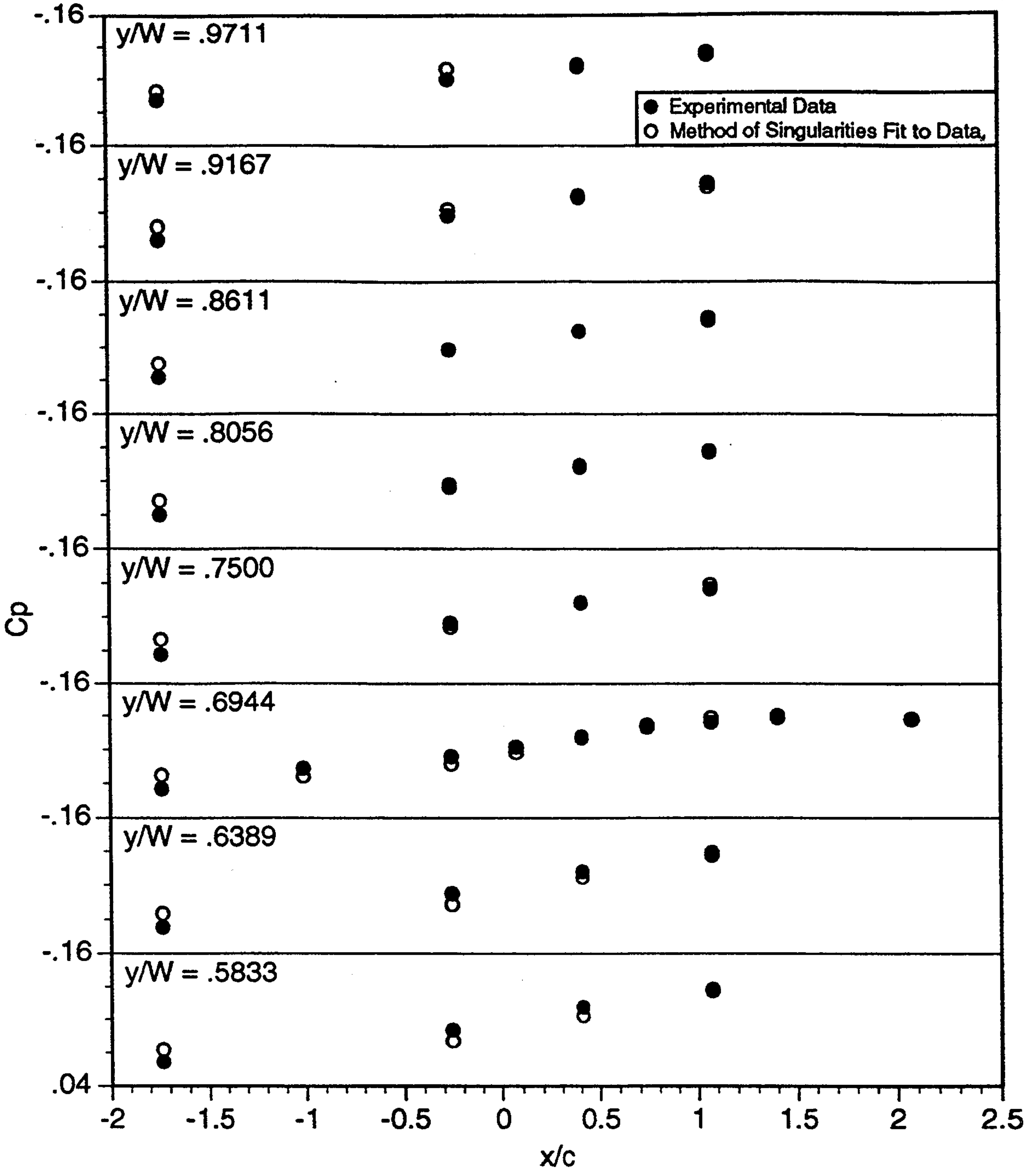

Figure 45b. Lower wall experimental data and method of singularities fit to the experimental data, using 16 singularities and 342 measurements to determine method of singularities solution. $U_\infty = 24.$ m/s, Re = 2.4×10^5, h/c = 3.0, $\alpha = 20$ degrees. Solid wall boundary condition.

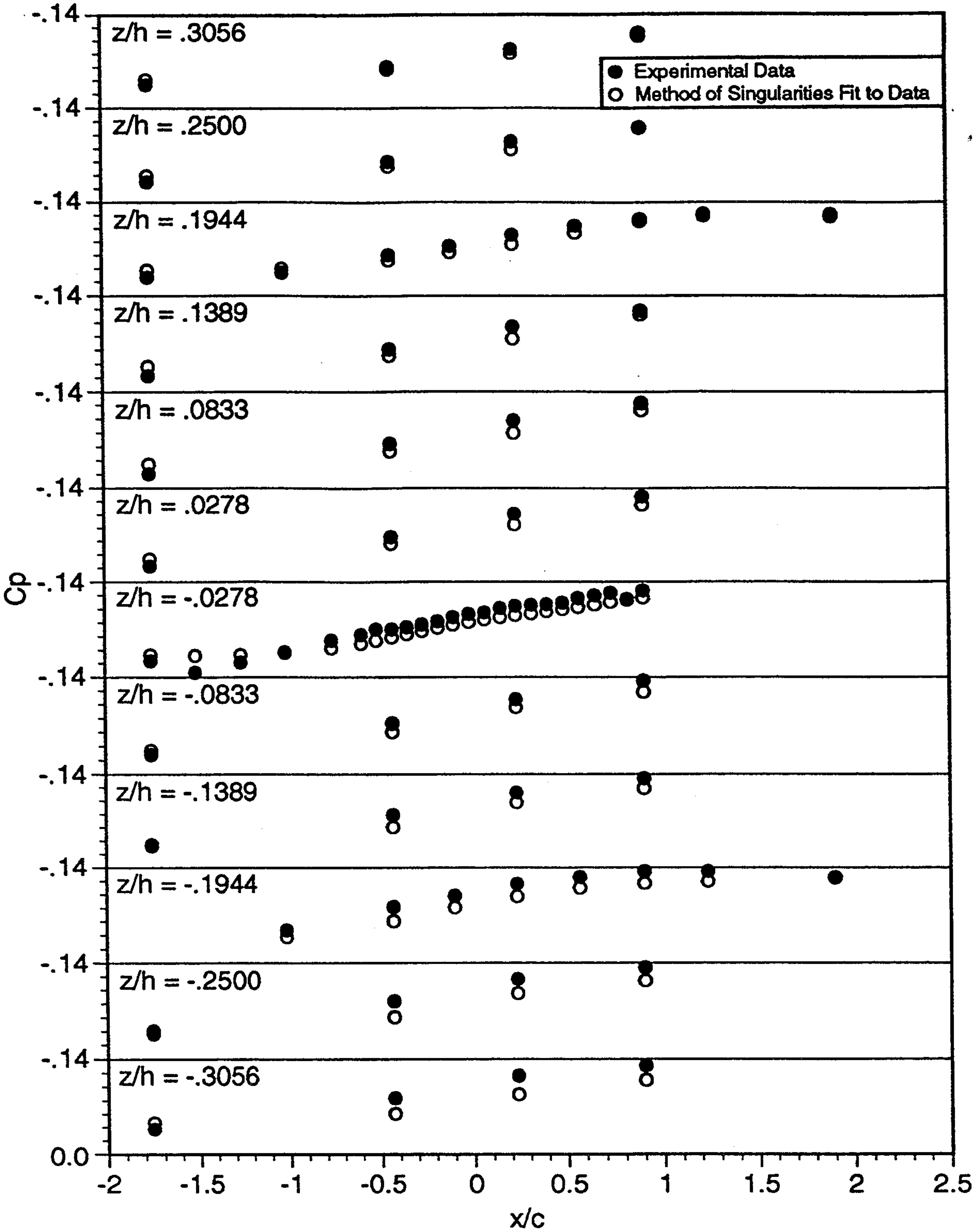

Figure 46. Side wall experimental data and method of singularities fit to the experimental data, using 16 singularities and 342 measurements to determine method of singularities solution. $U_\infty = 24.$ m/s, $Re = 2.4 \times 10^5$, $h/c = 3.0$, $\alpha = 20$ degrees. Solid wall boundary condition.

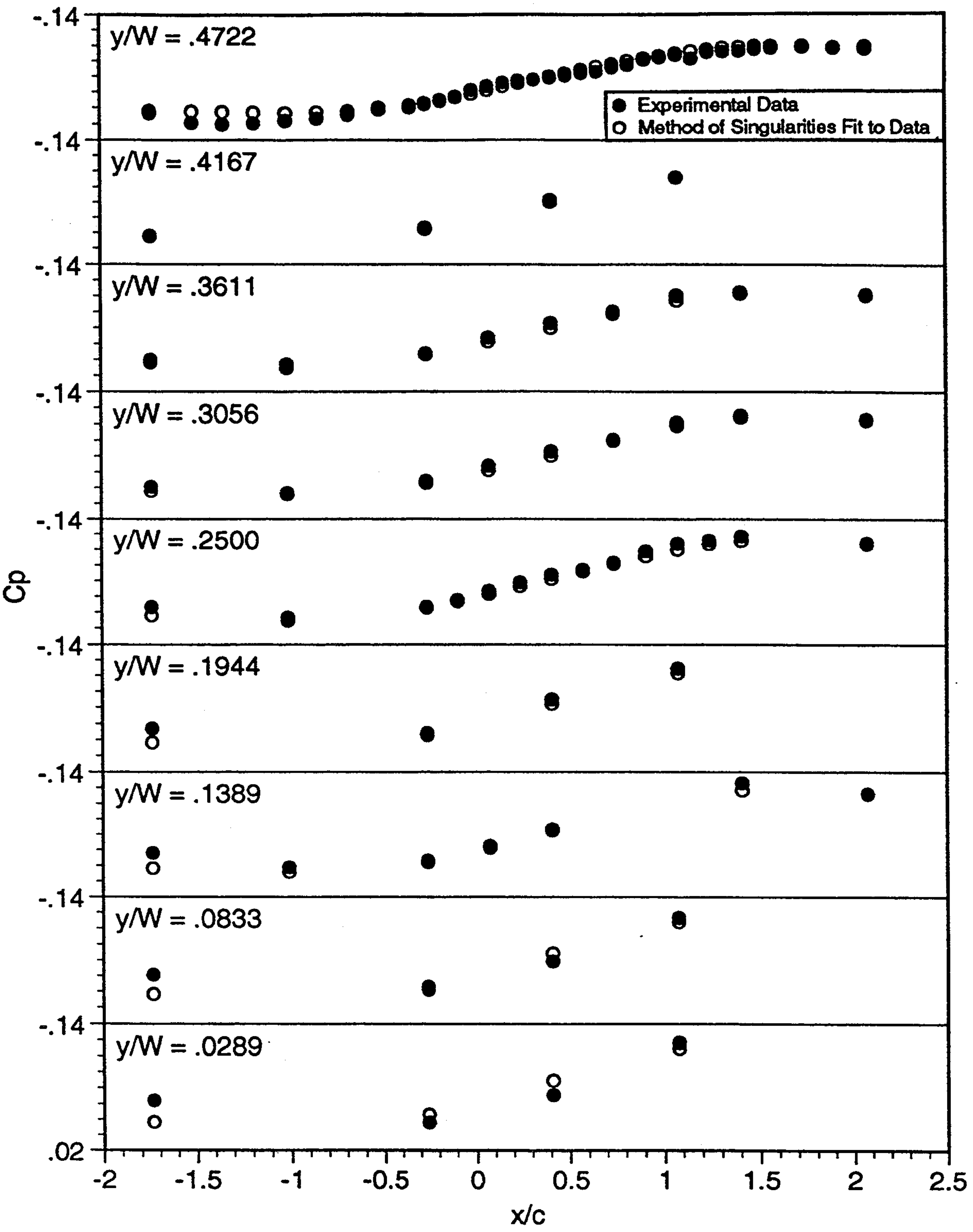

Figure 47a. Upper wall experimental data and method of singularities fit to the experimental data, using 16 singularities and 342 measurements to determine method of singularities solution. $U_\infty = 24.$ m/s, $Re = 2.4 \times 10^5$, $h/c = 3.0$, $\alpha = 20$ degrees. Porous wall boundary condition.

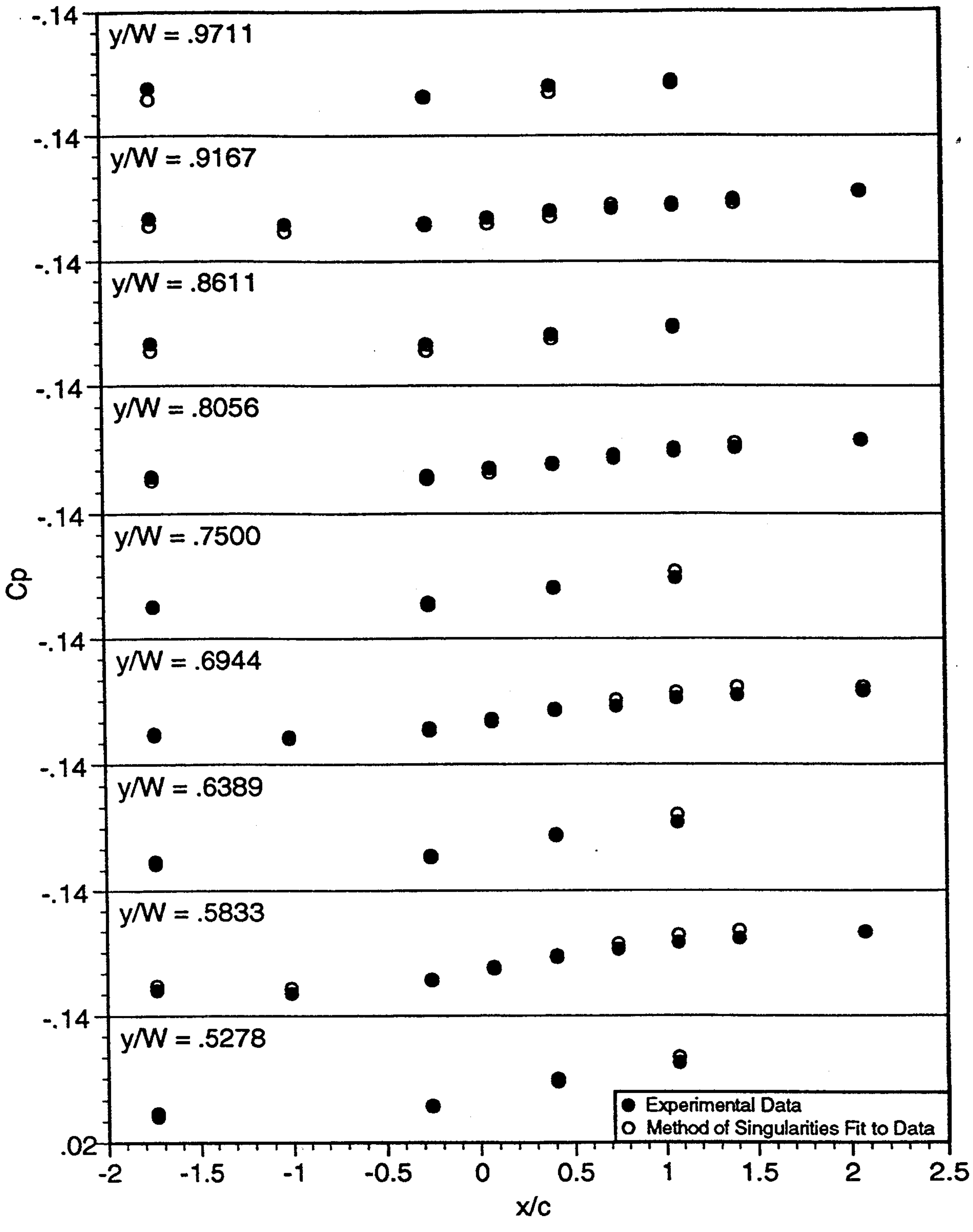

Figure 47b. Upper wall experimental data and method of singularities fit to the experimental data, using 16 singularities and 342 measurements to determine method of singularities solution. $U_\infty = 24.$ m/s, Re = 2.4×10^5, h/c = 3.0, $\alpha = 20$ degrees. Porous wall boundary condition.

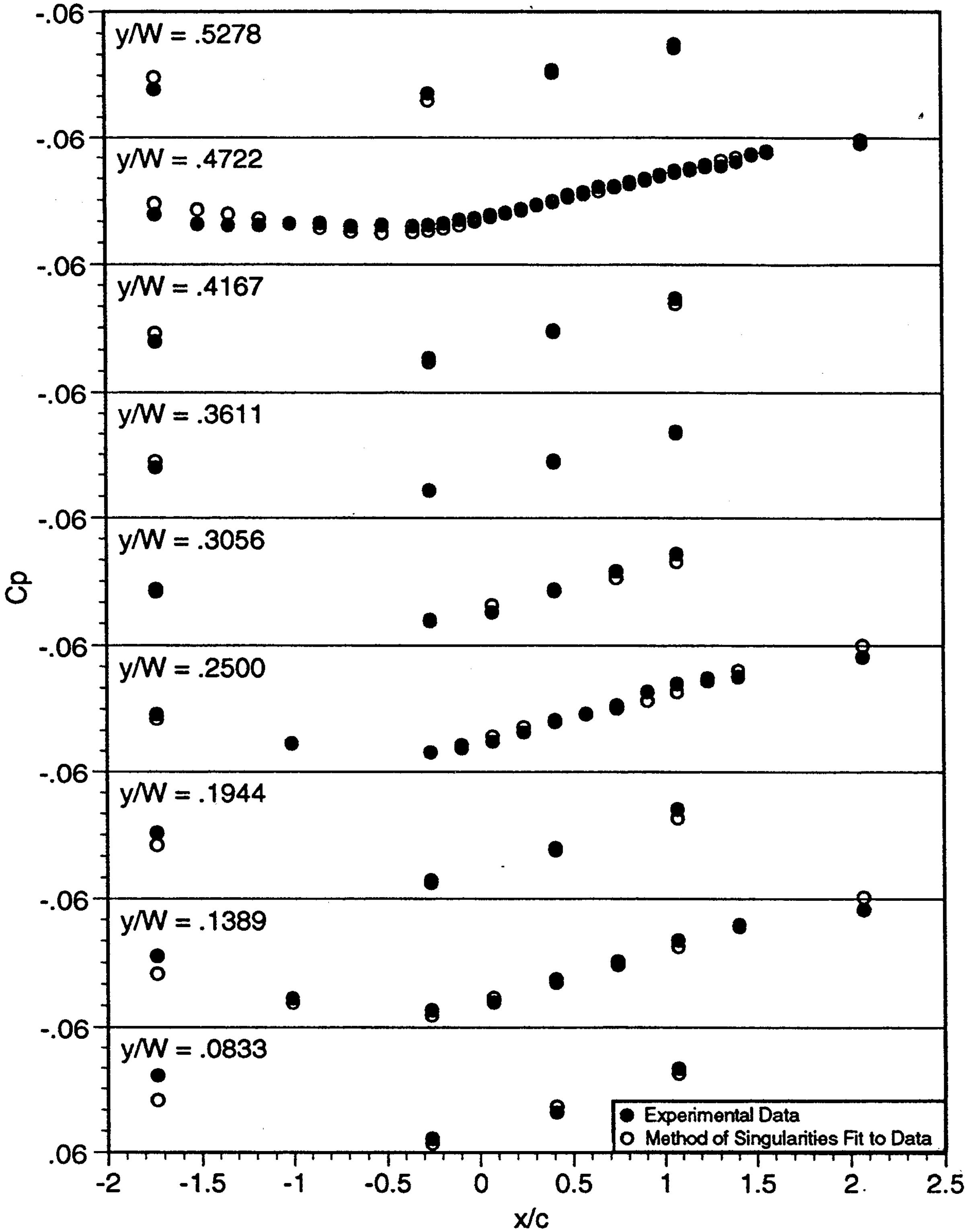

Figure 48a. Lower wall experimental data and method of singularities fit to the experimental data, using 16 singularities and 342 measurements to determine method of singularities solution. $U_\infty = 24.$ m/s, Re = 2.4 x 10^5, h/c = 3.0, $\alpha = 20$ degrees. Porous wall boundary condition.

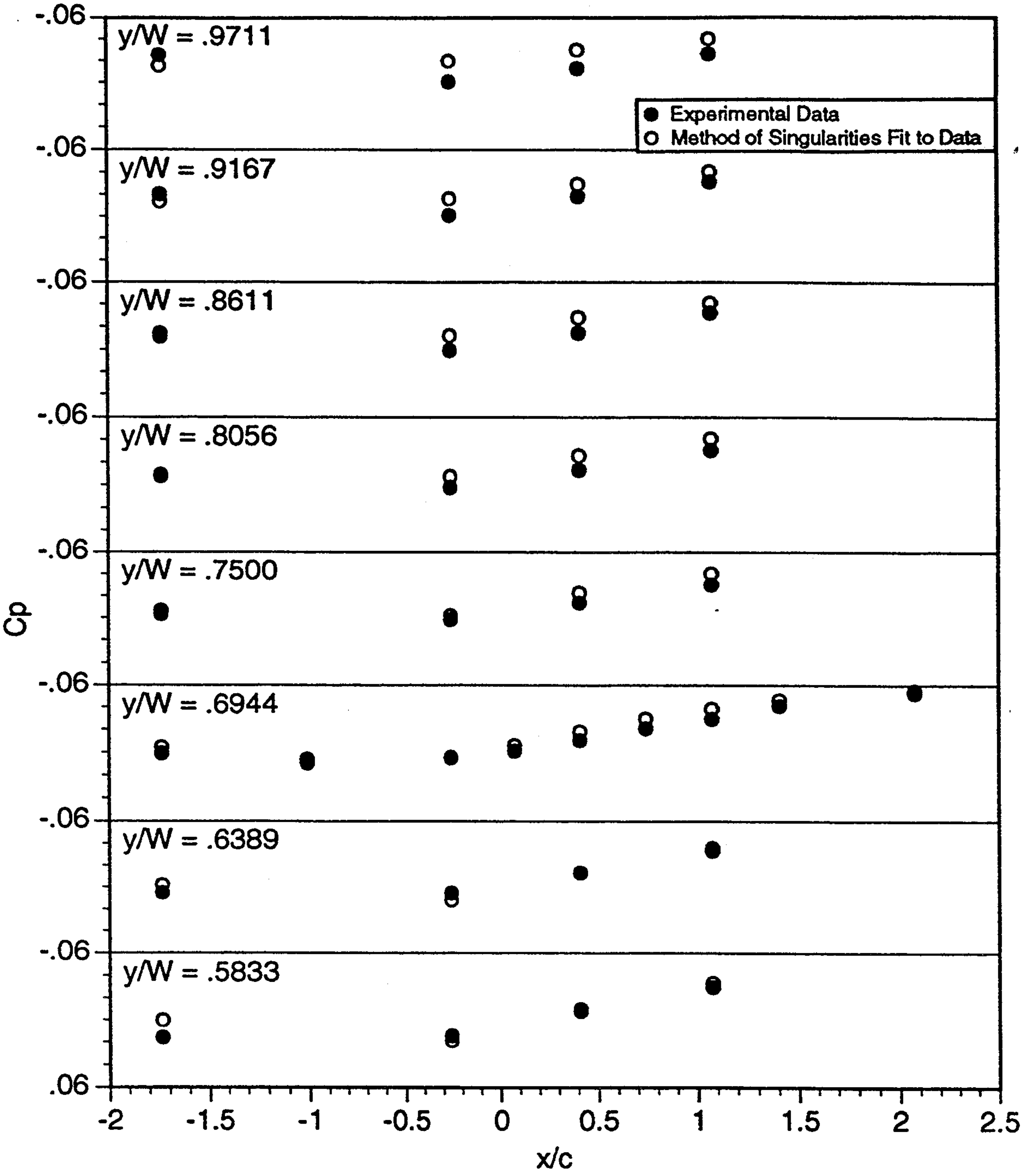

Figure 48b. Lower wall experimental data and method of singularities fit to the experimental data, using 16 singularities and 342 measurements to determine method of singularities solution. $U_\infty = 24.$ m/s, Re = 2.4×10^5, h/c = 3.0, $\alpha = 20$ degrees. Porous wall boundary condition.

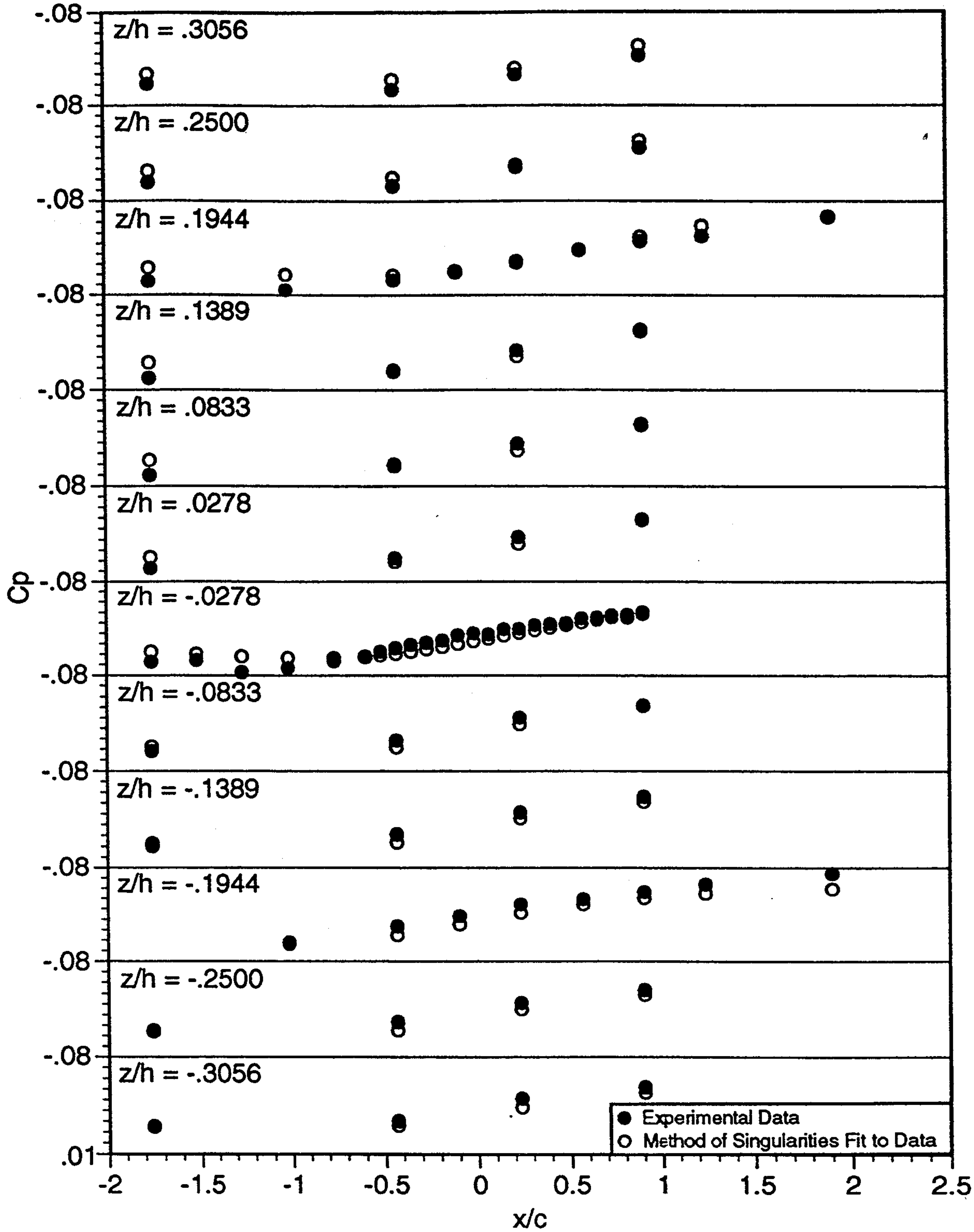

Figure 49. Side wall experimental data and method of singularities fit to the experimental data, using 16 singularities and 342 measurements to determine method of singularities solution. $U_\infty = 24.$ m/s, $Re = 2.4 \times 10^5$, $h/c = 3.0$, $\alpha = 20$ degrees. Porous wall boundary condition.

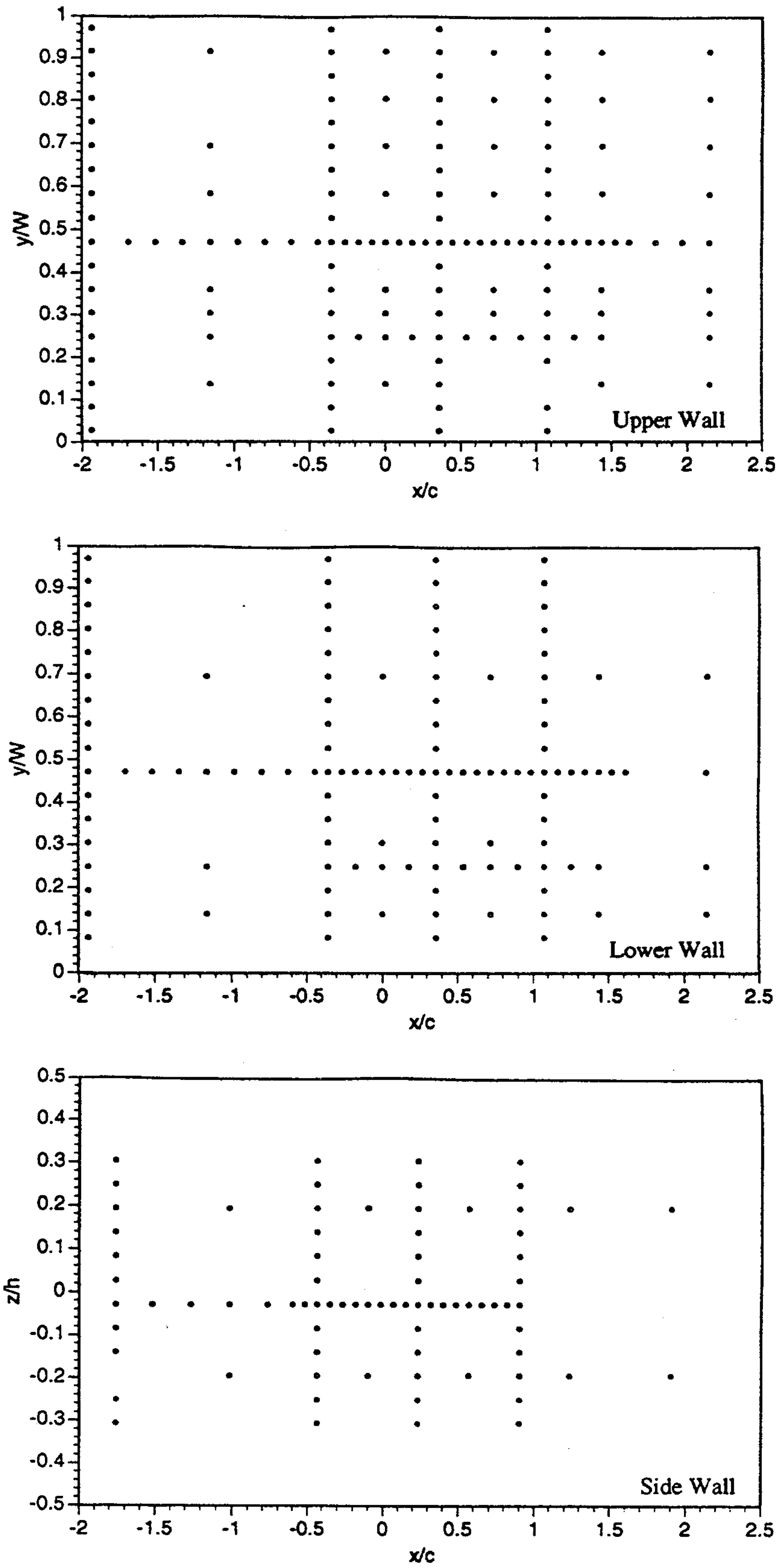

Figure 50a-c. Locations of the complete set of 342 measurements on the top, bottom and side walls.

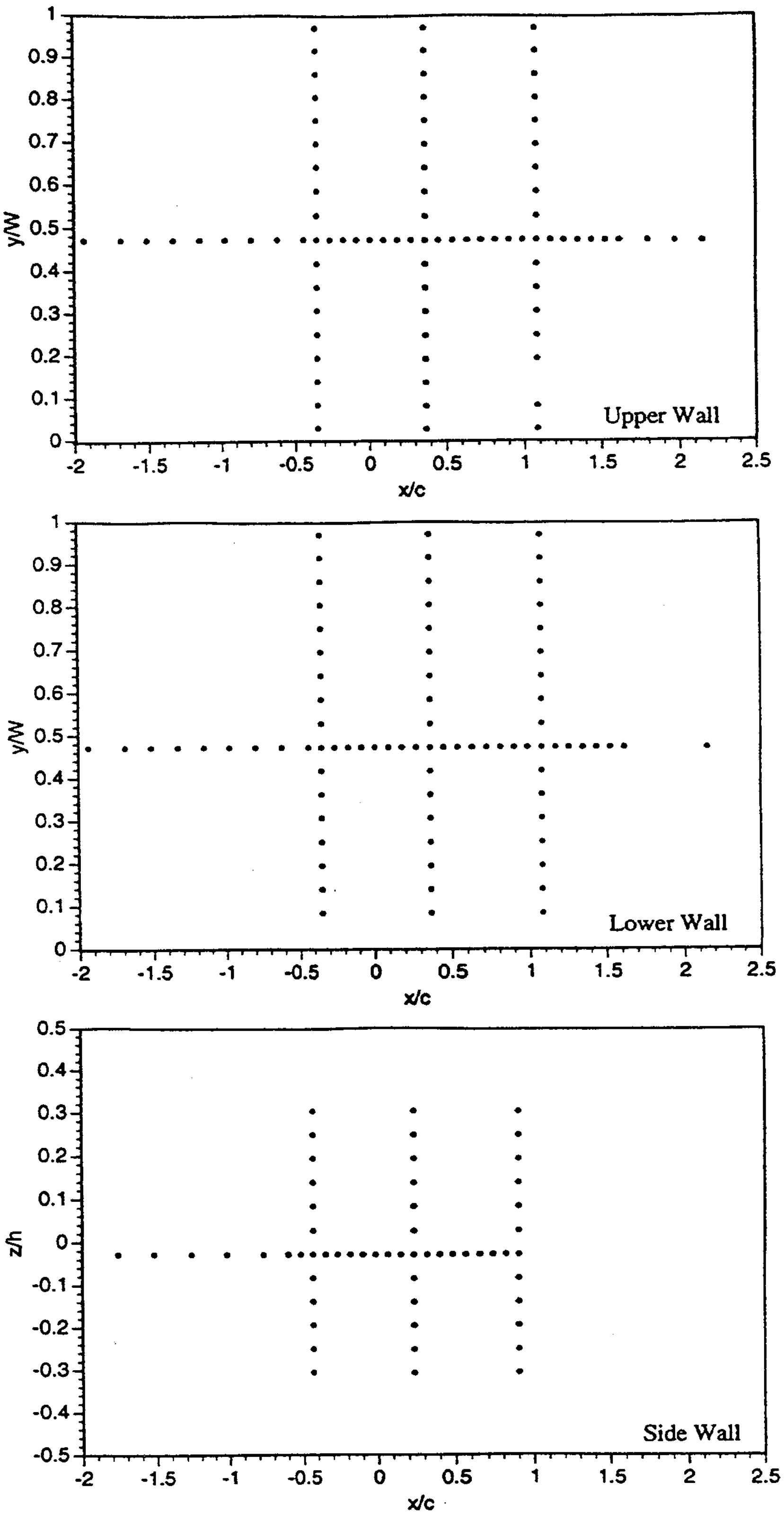

Figure 51a-c. Locations of the reduced set of 223 measurements on the top, bottom and side walls. Measurements are distributed along the centerlines of all three walls and 3 cross-planes.

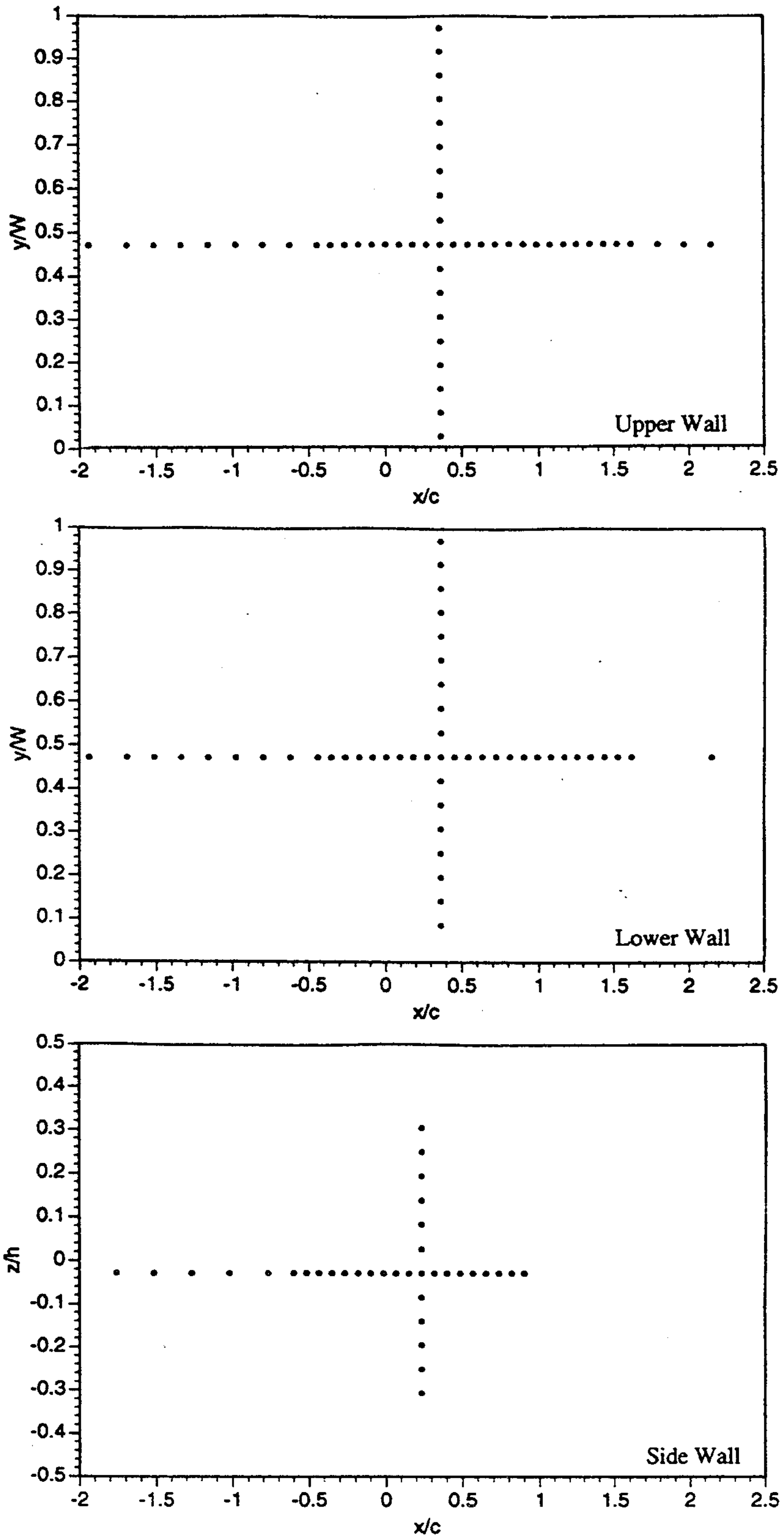

Figure 52a-c. Locations of the reduced set of 136 measurements on the top, bottom and side walls. Measurements are distributed along the centerlines of all three walls and 1 cross-plane.

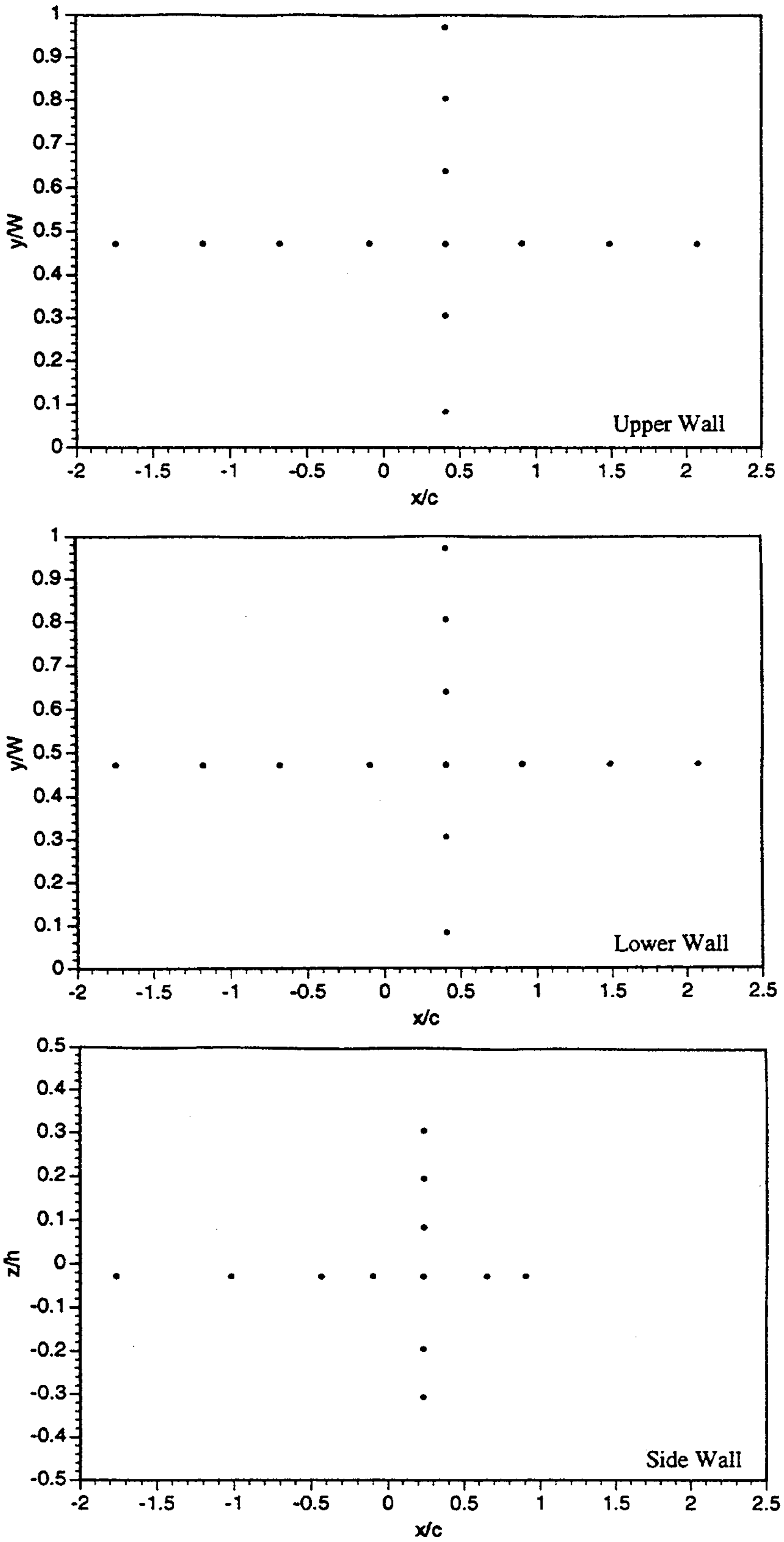

Figure 53a-c. Locations of the reduced set of 38 measurements on the top, bottom and side walls. Measurements are distributed along the centerlines of all three walls and 1 cross-plane.

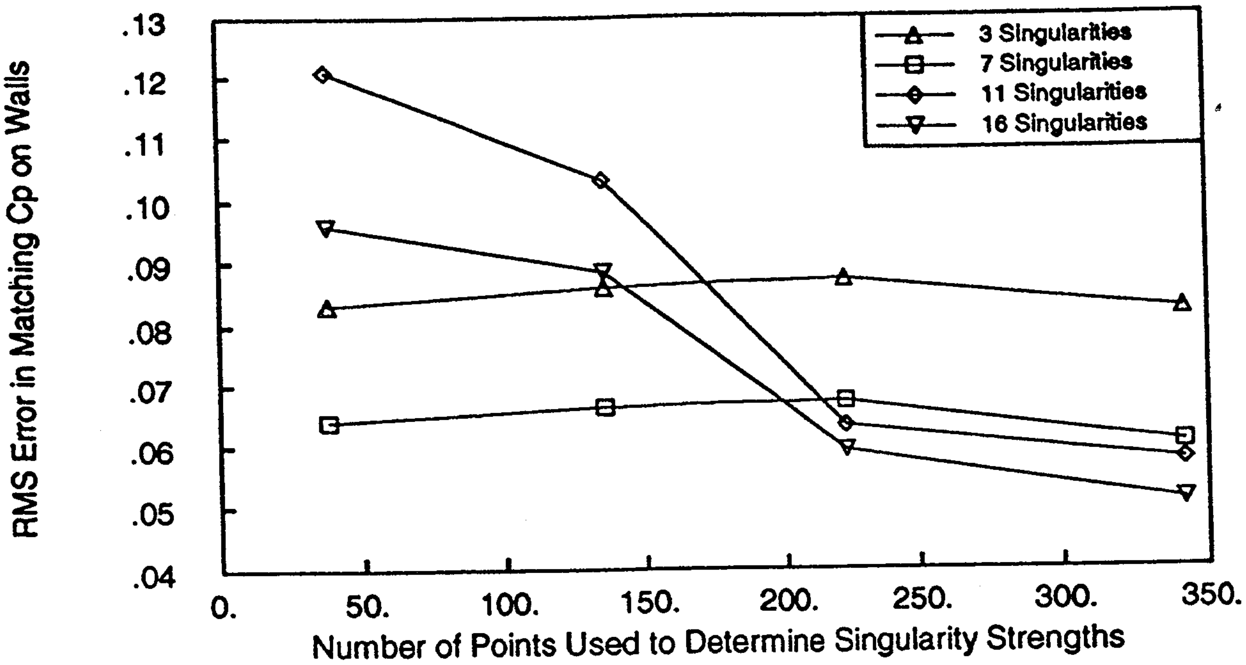

Figure 54. Effect on root-mean-square errors of using various numbers of singularities and various numbers of data points to develop method of singularities solutions. Results are shown for solid wall test at α = 20 degrees.

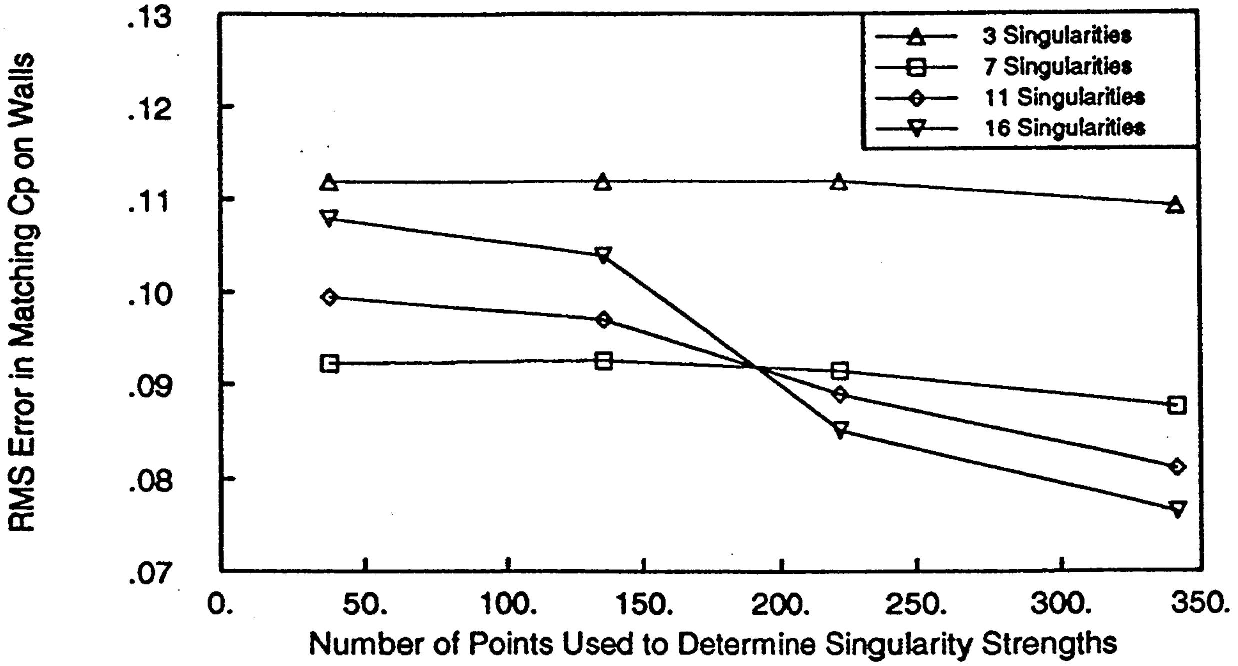

Figure 55. Effect on root-mean-square errors of using various numbers of singularities and various numbers of data points to develop method of singularities solutions. Results are shown for porous wall test at α = 20 degrees.

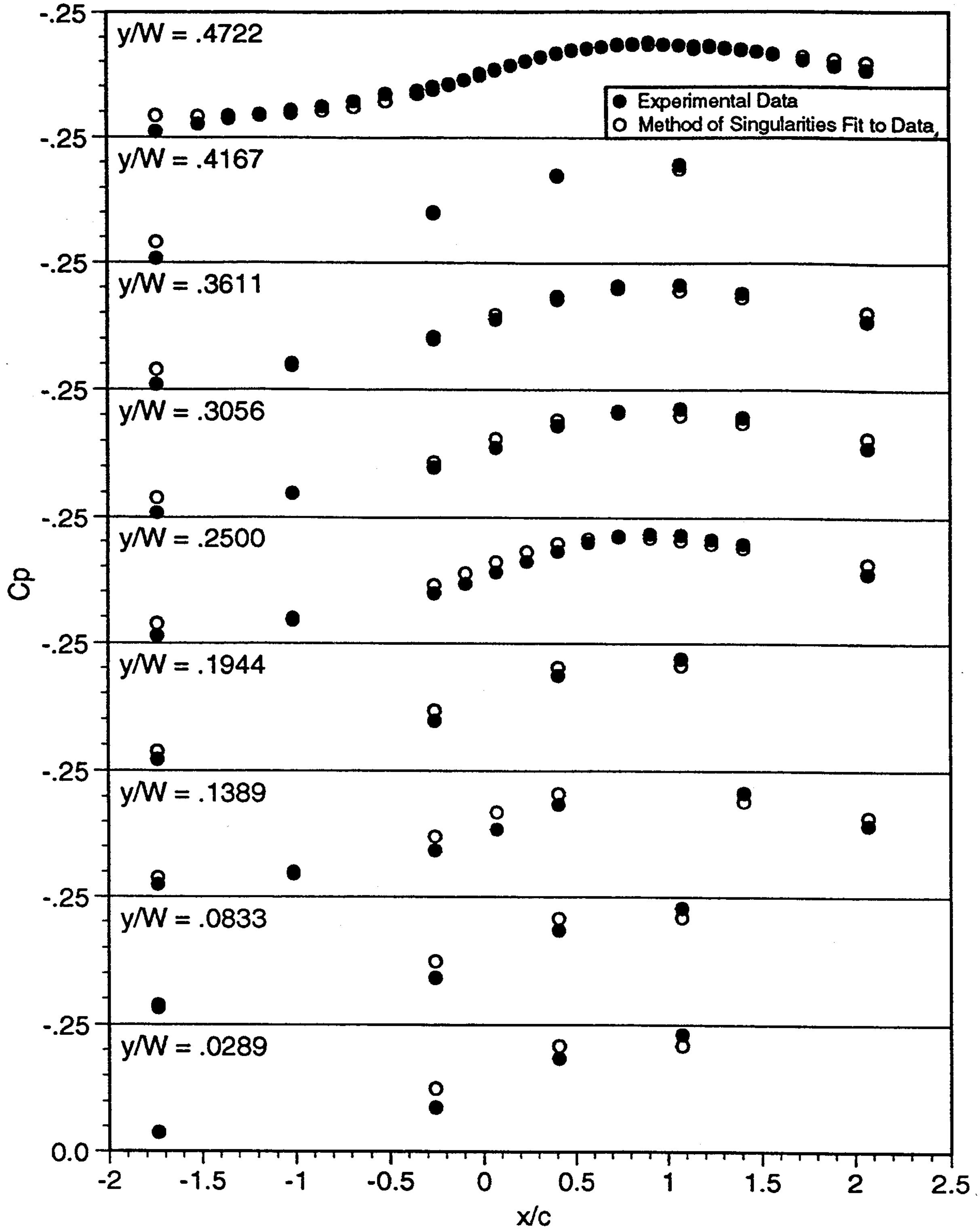

Figure 56a. Upper wall experimental data and method of singularities fit to the experimental data, using 7 singularities and 38 measurements to determine method of singularities solution. U_∞ = 24. m/s, Re = 2.4×10^5, h/c = 3.0, α = 20 degrees. Solid wall boundary condition.

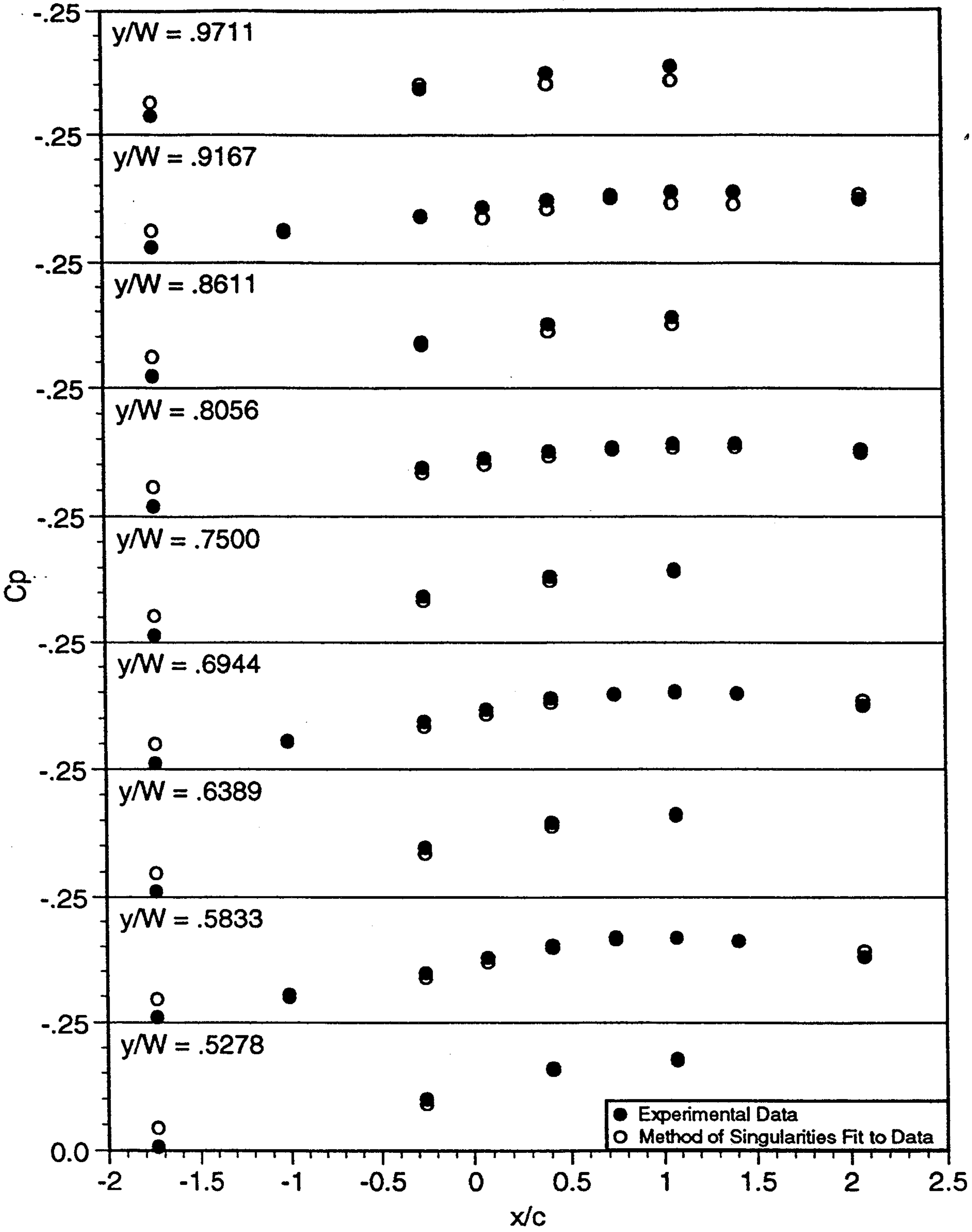

Figure 56b. Upper wall experimental data and method of singularities fit to the experimental data, using 7 singularities and 38 measurements to determine method of singularities solution. $U_\infty = 24.$ m/s, $Re = 2.4 \times 10^5$, $h/c = 3.0$, $\alpha = 20$ degrees. Solid wall boundary condition.

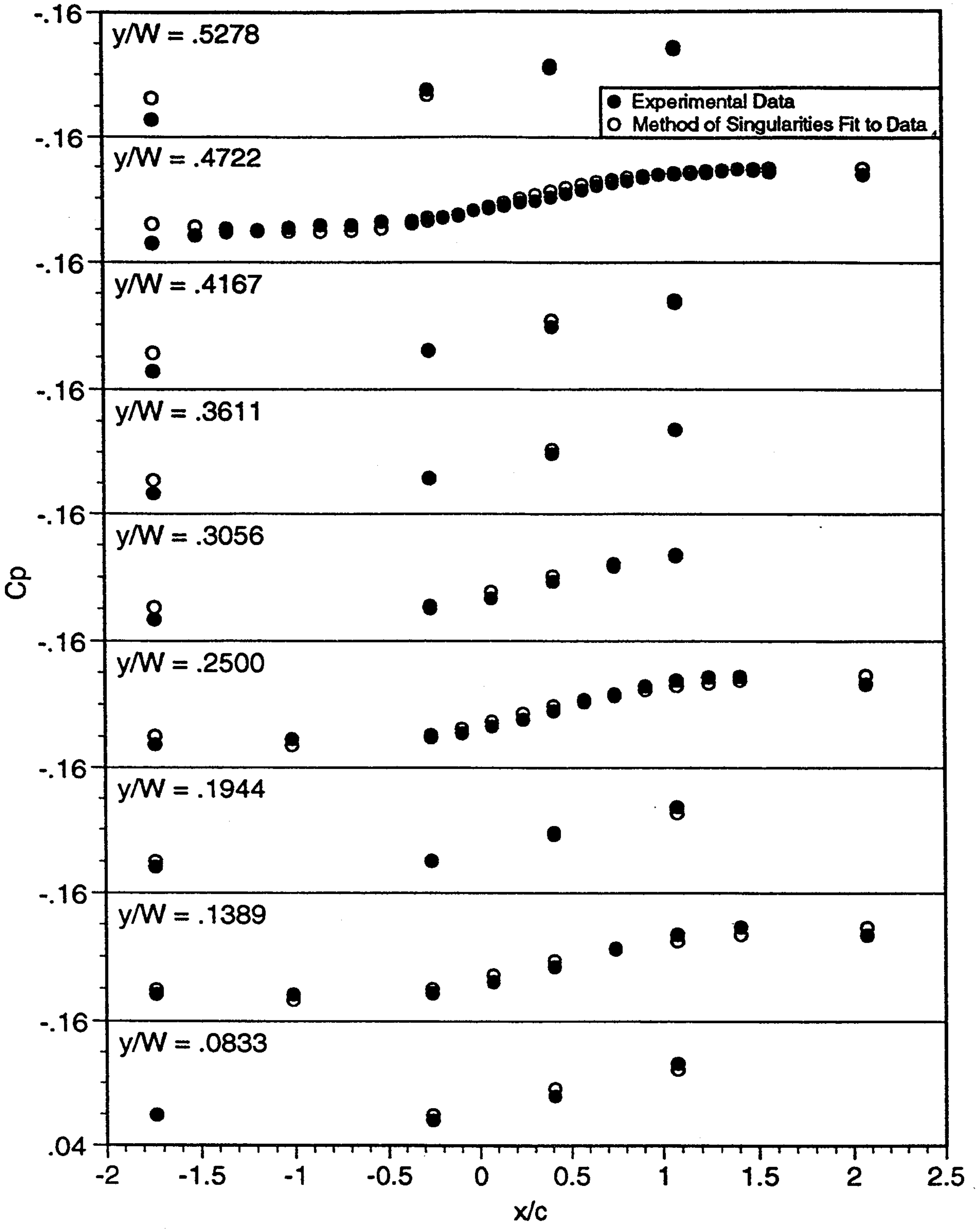

Figure 57a. Lower wall experimental data and method of singularities fit to the experimental data, using 7 singularities and 38 measurements to determine method of singularities solution. $U_\infty = 24.$ m/s, $Re = 2.4 \times 10^5$, $h/c = 3.0$, $\alpha = 20$ degrees. Solid wall boundary condition.

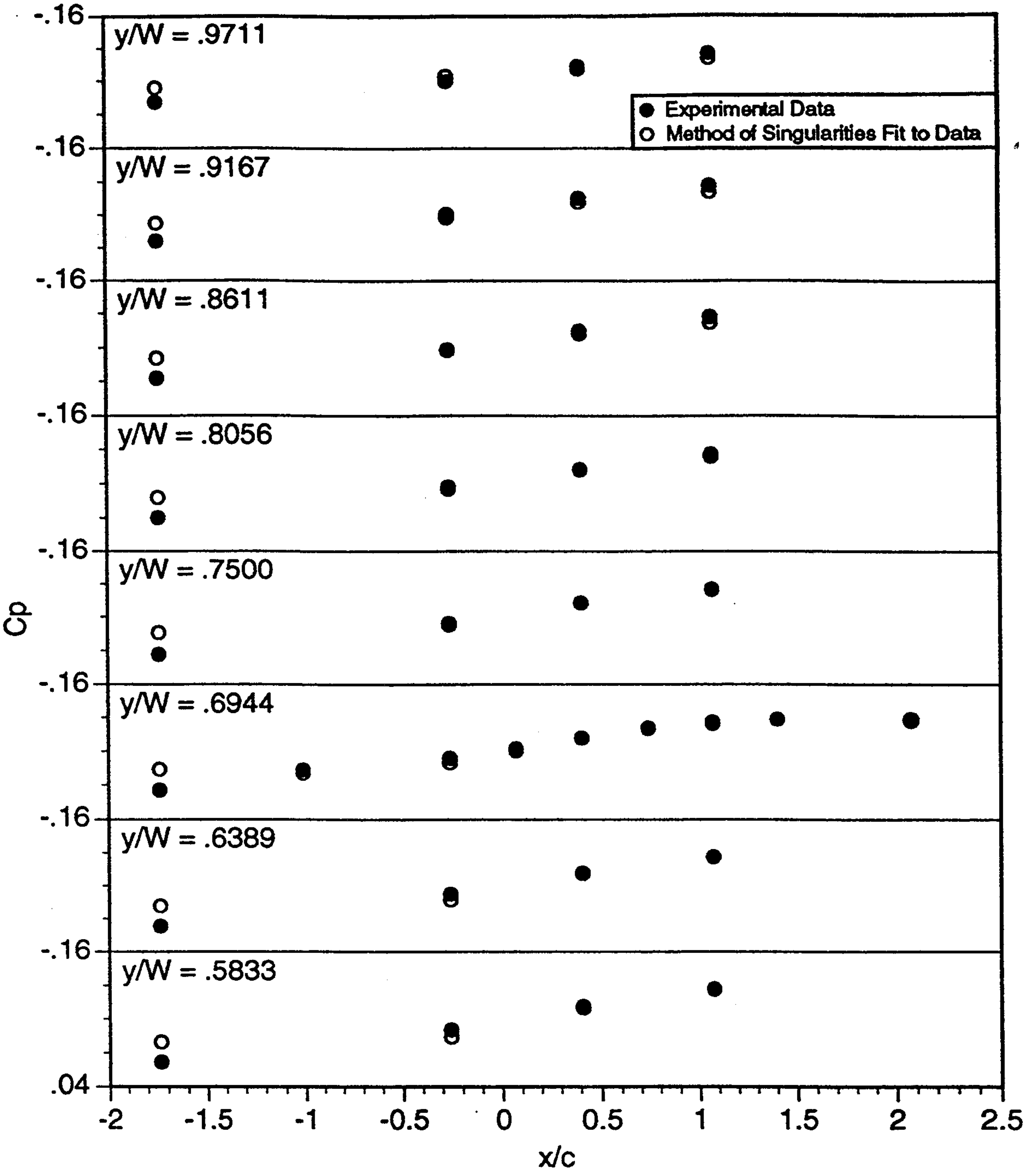

Figure 57b. Lower wall experimental data and method of singularities fit to the experimental data, using 7 singularities and 38 measurements to determine method of singularities solution. $U_\infty = 24.$ m/s, Re = 2.4×10^5, h/c = 3.0, $\alpha = 20$ degrees. Solid wall boundary condition.

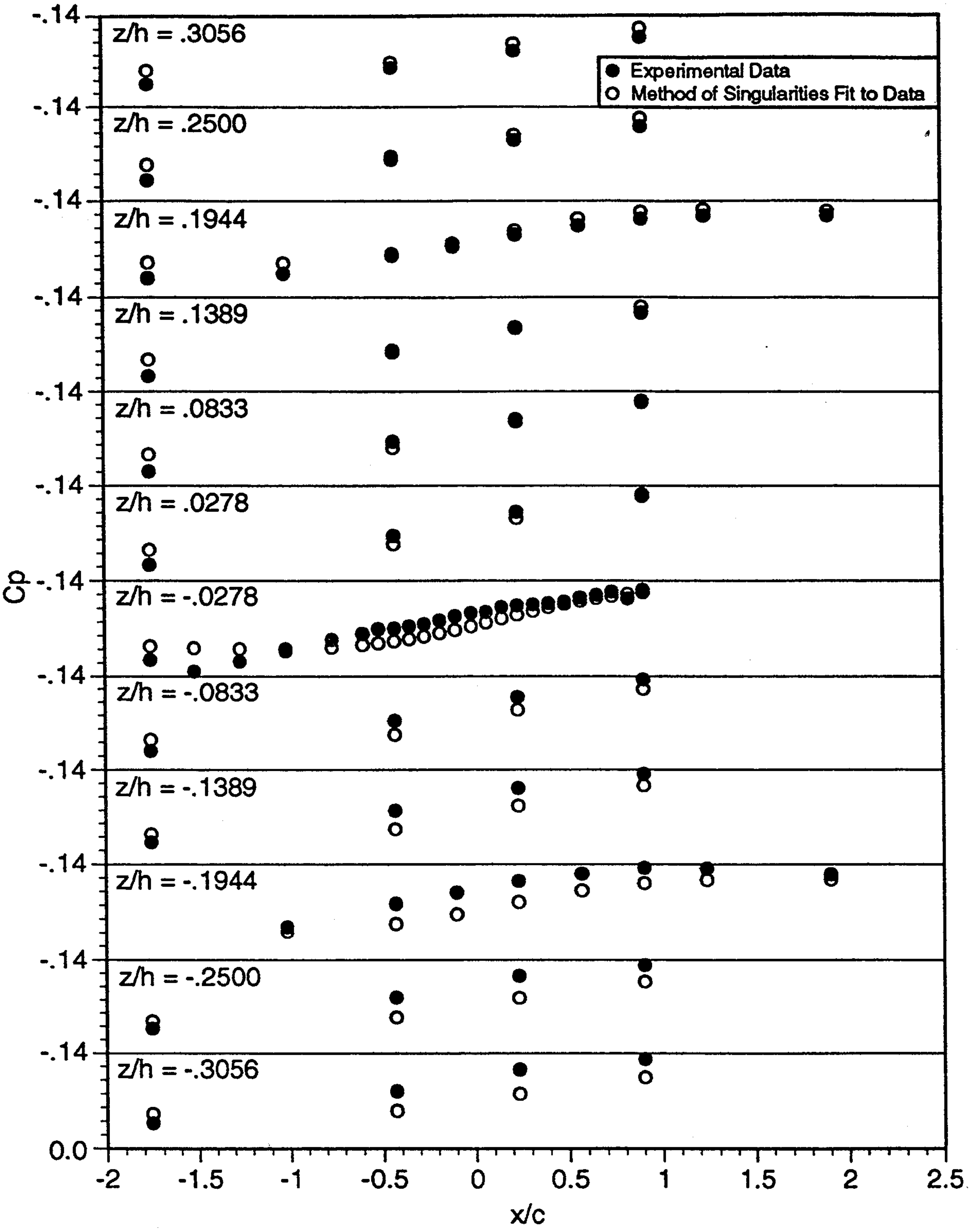

Figure 58. Side wall experimental data and method of singularities fit to the experimental data, using 7 singularities and 38 measurements to determine method of singularities solution. $U_\infty = 24.$ m/s, Re = 2.4×10^5, h/c = 3.0, $\alpha = 20$ degrees. Solid wall boundary condition.

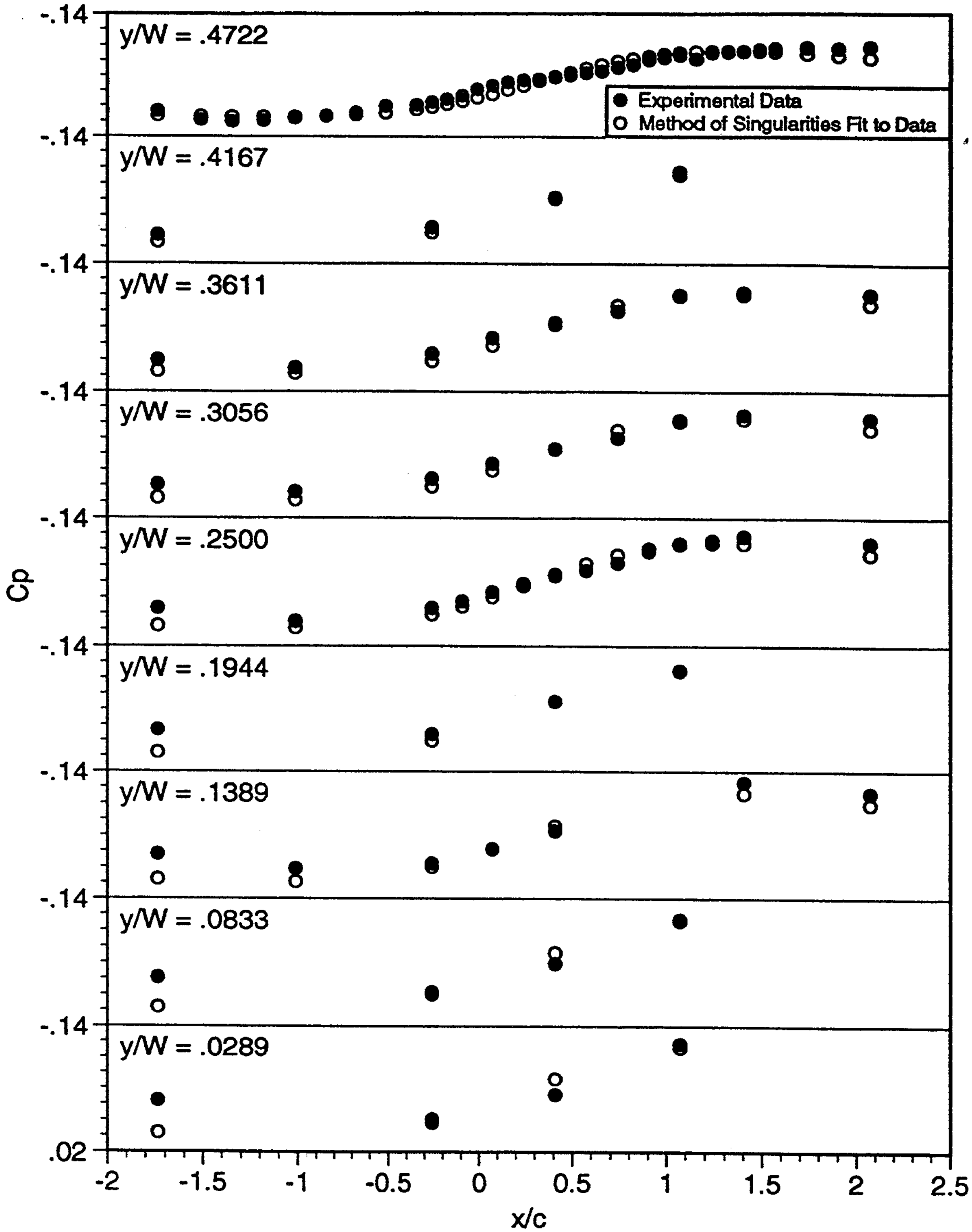

Figure 59a. Upper wall experimental data and method of singularities fit to the experimental data, using 7 singularities and 38 measurements to determine method of singularities solution. $U_\infty = 24.$ m/s, $Re = 2.4 \times 10^5$, $h/c = 3.0$, $\alpha = 20$ degrees. Porous wall boundary condition.

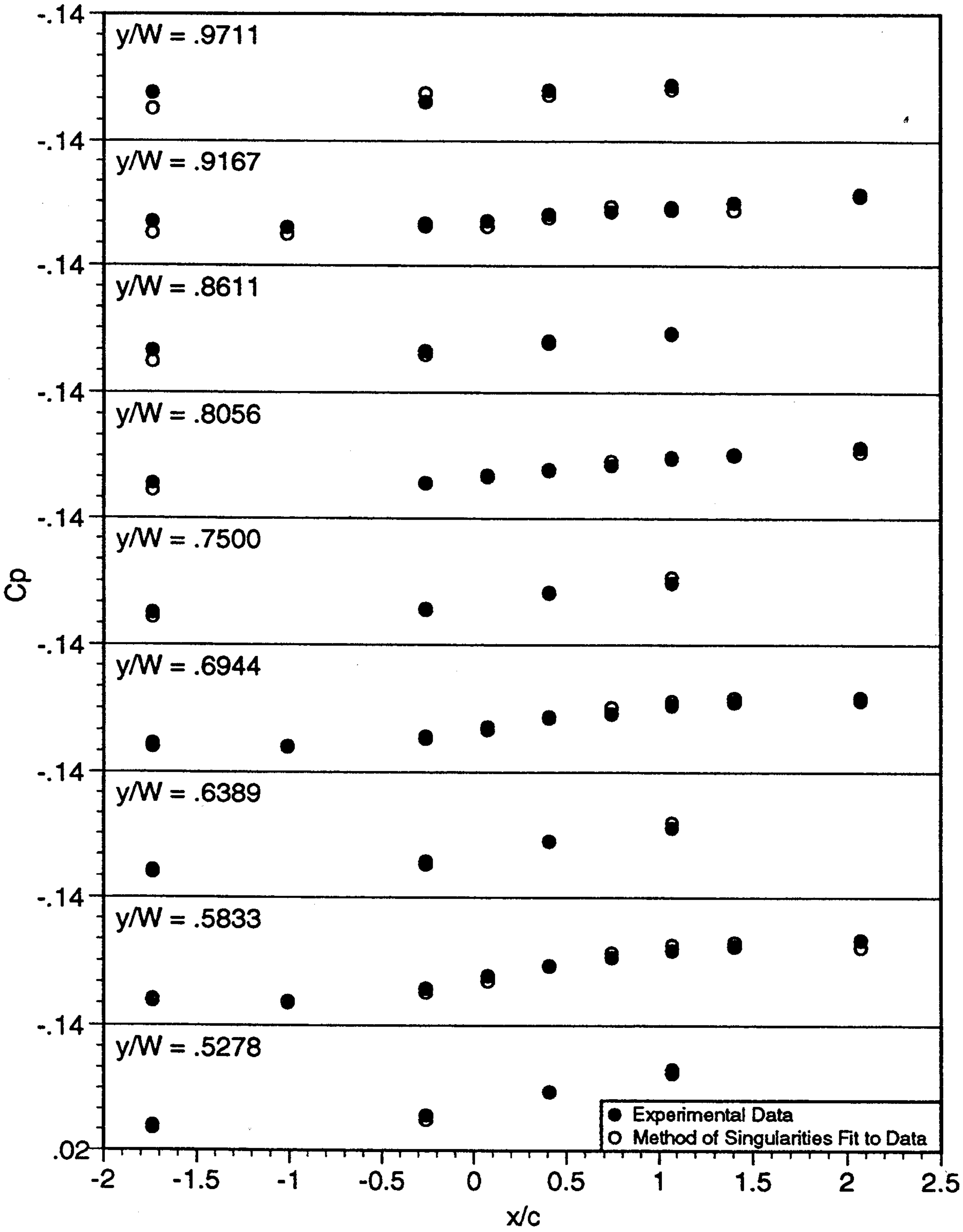

Figure 59b. Upper wall experimental data and method of singularities fit to the experimental data, using 7 singularities and 38 measurements to determine method of singularities solution. $U_\infty = 24.$ m/s, Re = 2.4×10^5, h/c = 3.0, $\alpha = 20$ degrees. Porous wall boundary condition.

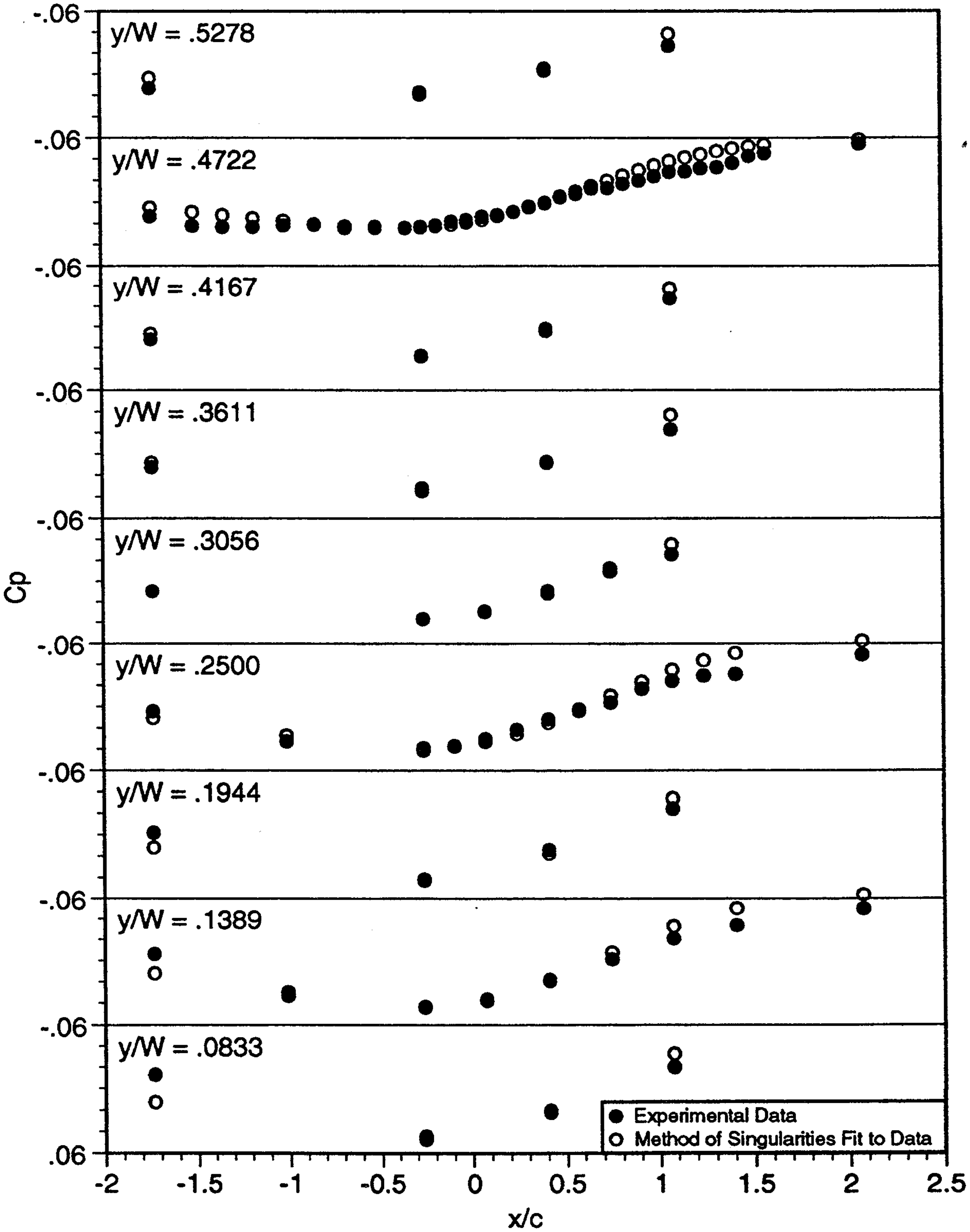

Figure 60a. Lower wall experimental data and method of singularities fit to the experimental data, using 7 singularities and 38 measurements to determine method of singularities solution. $U_\infty = 24.$ m/s, $Re = 2.4 \times 10^5$, $h/c = 3.0$, $\alpha = 20$ degrees. Porous wall boundary condition.

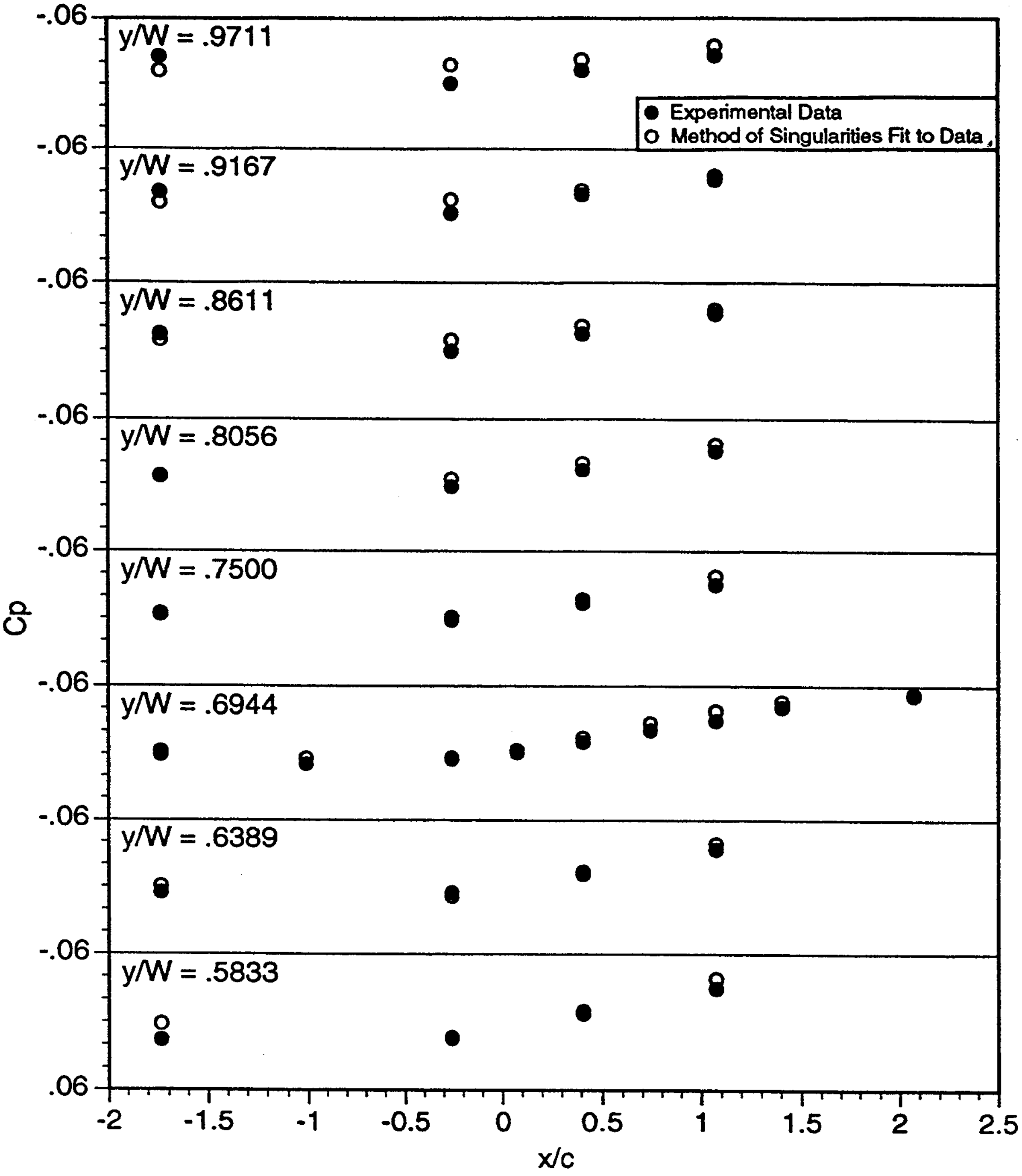

Figure 60b. Lower wall experimental data and method of singularities fit to the experimental data, using 7 singularities and 38 measurements to determine method of singularities solution. $U_\infty = 24.$ m/s, Re = 2.4×10^5, h/c = 3.0, $\alpha = 20$ degrees. Porous wall boundary condition.

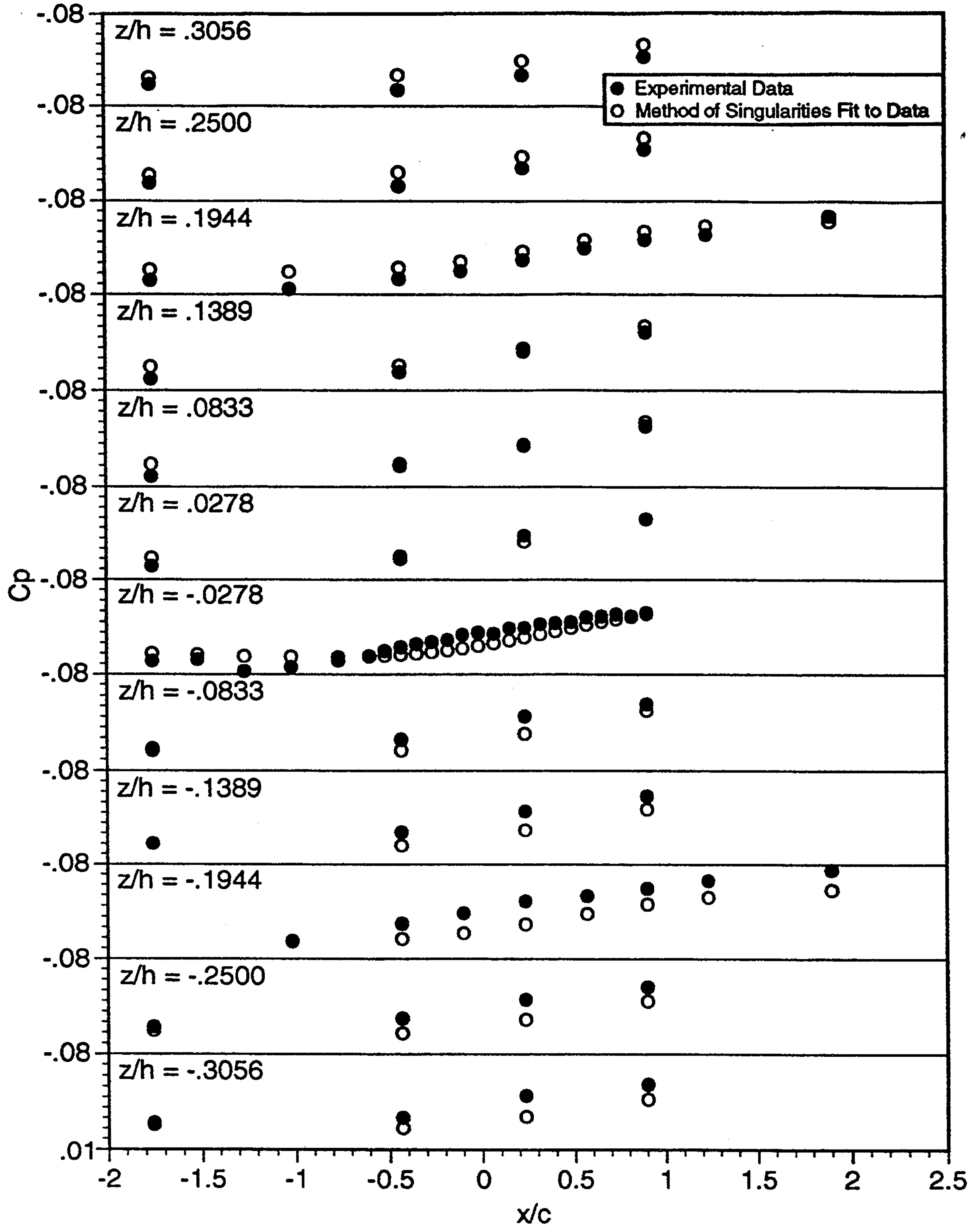

Figure 61. Side wall experimental data and method of singularities fit to the experimental data, using 7 singularities and 38 measurements to determine method of singularities solution. $U_\infty = 24.$ m/s, $Re = 2.4 \times 10^5$, $h/c = 3.0$, $\alpha = 20$ degrees. Porous wall boundary condition.

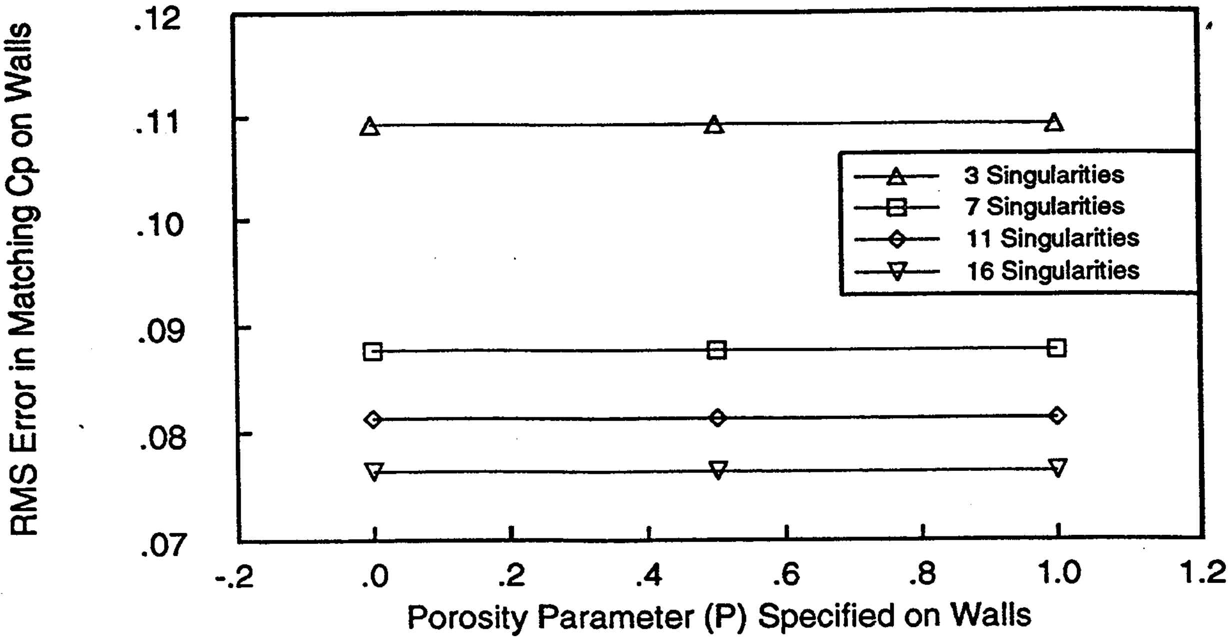

Figure 62 Root-mean-square errors as a function of the porosity specified in the method of singularities. Data shown is for $\alpha = 20$ degrees, porous wall test.

Chapter 6

Conclusion

A method for describing porous wall boundary conditions based on sparse, nonintrusive measurements of flow quantities at the wall boundary has been developed. This method utilized a potential flow solution based on least squares matching of singularity strengths to measured experimental data. The consistency of imposing a pressure boundary condition based on this method with other means of describing a wall boundary condition has been demonstrated in computational studies. This method has been shown to provide a good description of the entire wall boundary condition even when as few as 8 measurements were used to develop the method of singularities solution. The ability of this method to predict the effects of changing porosity in a wind tunnel test has been demonstrated by simulation of experiments performed in a variable porosity test section.

This method has been extended to three-dimensional porous wall testing. In three dimensions, the method of singularities allowed the porous wall boundary condition to be modelled without the need for normal velocity perturbation measurements and without the need for extensive calibrations of the wall. An experimental study has shown that the method was capable of capturing the trends in pressure profiles existing on the walls in three-dimensional porous and solid wall tests.

In low speed tests, the method of singularities has been found to be rather insensitive to the value of the porosity parameter specified. This allowed for the porosity parameter to be found by means of least squares matching. While changes in the porosity parameter did have a strong effect on the singularity strengths, the effect on the overall match to the pressure profile was minimal. Since the porosity parameter was not specified as a boundary condition in the CFD code, and no corrections were made to the wind tunnel data, this method eliminated many of the concerns associated with the classical linear porous wall boundary condition. This method also allowed for a simulation of the entire flow field and direct comparison of the flow field to wind tunnel data without the need for corrections to the experimental data.

References

1) Mokry, M., Chan, Y.Y., and Jones, D.J., "Two-Dimensional Wind Tunnel Wall Interference," AGARD Report AG-281, 1983.

2) Theodorsen, T., "The Theory of Wind-Tunnel Wall Interference," NACA Technical Report 410, 1931.

3) Wright, R.H. and Ward, V.G., "NACA Transonic Wind-Tunnel Test Sections," NACA Technical Report 1231, 1956.

4) Shujie, W., Yuan, R. and Ruiqin, C., "Investigation of Wall Interference at High Angle of Attack in a Low Speed Wind Tunnel with Slotted Wall," AIAA Paper 87-2611, 1987.

5) Ritchie, V.S. and Pearson, A.O., "Calibration of the Slotted Tests Section of the Langley 8-Foot Transonic Tunnel and Preliminary Experimental Investigation of Boundary Reflected Disturbances," NACA RM L51K14, July 7, 1952.

6) Baldwin, B.S., Turner, J.B., and Knechtel, E.D., "Wall Interference in Wind Tunnels with Slotted and Porous Boundaries at Subsonic Speeds," NACA TN 3176 May 1954.

7) Marvin, J.G., "Accuracy Requirements and Benchmark Experiments for CFD Validation," AGARD CP 437, May 1988.

8) Lan, C.E. and Thomas, J.P., "Application of Computational Aerodynamics to Assessment/Correction in Wind Tunnel Testing," KU-FRL-887-1, The University of Kansas Center for Research, Inc., Sept. 28, 1990.

9) Levy, L.L., "Experimental and Computational Steady and Unsteady Transonic Flows about a Thick Airfoil," AIAA Journal, Vol. 16, No. 6, June 1978.

10) Potsdam, M. and Roberts, L., "A Numerical Study of the Effects of Wind Tunnel Wall Proximity on an Airfoil Model," JIAA TR-99, Stanford University, Department of Aeronautics and Astronautics, Sept. 1990.

11) Lynch, F.T., "Experimental Necessities for Subsonic Transport Configuration Development," AIAA Paper 92-0158, January 1992.

12) Olson, L.E., "Future Experimental Needs in Low Speed Aerodynamics," AIAA Paper 92-0157, January 1992.

13) Agrell, N. and Pettersson, B., "Numerical Computations and Measurements of Transonic Flow in a Slotted-Wall Wind Tunnel," AIAA Paper 87-2610, 1987.

14) Al-Saadi, J.A., and DeJarnette, F.R., "Wall Interference Calculation in a Transonic Test Section Including Simulation of Discrete Slots," AIAA Paper 92-0032, Jan. 1992.

15) Rizk, M.H. and Lovell, D.R., "Euler Procedure for Correcting Two-Dimensional Transonic Wind-Tunnel Wall Interference," AIAA Journal, Vol. 26, No. 12, December 1988.

16) Gopinath, R., "Wall Interference Evaluation from Pressure Measurements on Control Surfaces," AIAA 82-4301, Journal of Aircraft, Vol 19, No. 12, pp. 1097-1098, December, 1982.

17) King, L.S. and Johnson, D.A., "Calculations of Transonic Flow About an Airfoil in a Wind Tunnel," AIAA Paper 80-1366, 1980.

18) King, L.S. and Johnson, D.A., "Transonic Airfoil Calculations Including Wind Tunnel Wall-Interference Effects," AIAA Journal, Vol 24, No. 8, August 1986.

19) Jacocks, J.L., "An Investigation of the Aerodynamic Characteristics of Ventilated Test Section Walls for Transonic Wind Tunnels," PhD Dissertation, The University of Tennessee, December 1976.

20) Crites, R. and Rueger, M., "Modelling the Ventilated Wind Tunnel Wall", AIAA Paper 92-0035, January 1992.

21) Rueger, M. and Crites, R., "Wind Tunnel Boundary Interference Prediction and Correction," AIAA Paper 92-0036, Jan. 1992.

22) Smith, J. "A Method for Determining 2D Wall Interference on an Aerofoil from Measured Pressure Distributions Near the Walls and on the Model," NLR TR 81016 U, January 1981.

23) Cooper, G.K. and Sirbaugh, J.R., "PARC Code: Theory and Usage," Arnold Engineering Development Center, AEDC-TR-89-15, December 1989.

24) Potsdam, M., and Beutner, T.J., Unpublished results using unstructured grid solver, 1990.

25) Shujie,W., Rongxi, Y., and Ruiqin, C., "Investigation of Wall Interference at High Angle of Attack in a Low Speed Wind Tunnel with Slotted Wall," AIAA Paper 87-2611, 1987.

26) Murman, E. M., "Computation of Wall Effects In Ventilated Transonic Wind Tunnels," AIAA Paper 72-1007, September, 1972.

27) Mokry, M., Peake, D.J. and Bowker, A.J., "Wall Interference on Two-Dimensional Supercritical Airfoils Using Wall Pressure Measurements to Determine the Porosity Factors for Tunnel Floor and Ceiling," LR-575, National Research Council Canada, Feb. 1974.

28) Mokry, M., "A Wake-Blockage Paradox in a Perforated Wall Wind Tunnel," AIAA Journal, Vol. 9, No. 12, pp 2462-2464, December 1971.

29) Slooff, J.W. and Piers, W.J., "The Effect of Finite Test Section Length on Wall Interference in 2-D Ventilated Windtunnels," AGARD CP 174, Paper 14, October 1975.

30) Katz, J., "Low Speed Aerodynamics From Wing Theory to Panel Methods, AE 620 class notes, San Diego State University, September, 1989.

31) Rogers, S.E., "Numerical Solution fo the Incompressible Navier-Stokes Equations," NASA TM 102199, Nov. 1990.

32) Beutner, T., Celik, Z., and Roberts, L., "Modelling of Solid/Porous Wall Boundary Conditions for the Validation of Computational Fluid Dynamics Codes," AIAA Paper 92-0033, January 1992.

33) Rogers, S.E., Wiltberger, N.L. and Kwak, D., "Efficient Simulation of Incompressible Viscous Flow Over Single and Multi-Element Airfoils," AIAA Paper 92-0405, January, 1992.

34) Baldwin, B. and Barth, T., "A One-Equation Turbulence Transport Model for High Reynolds Number Wall-Bounded Flows," NASA TM 102847, Aug. 1990.].

35) Peyret, R. and Taylor, T.D., "Computational Methods for Fluid Flow," © 1983, Springer-Verlag New York, Inc.

36) Roe, P.L., "Approximate Riemann Solvers, Parameter Vectors and Difference Schemes," Journal of Computational Physics, Vol. 43, pp357-372, 1981.

37) "The GRIDGEN 3D Multiple Block Grid Generation System, Vol. 1 and 2," WRDC-TR-90-3022, 1990.

38) Braslow, A.L. and Knox, E.C., "Simplified Method for Determination of Critical Height of Distributed Roughness Particles for Boundary-Layer Transition at Mach Numbers from 0 to 5," NACA TN 4363, Langley Aeronautical Laboratory, September 1958.

39) Braslow, A.L., Hicks, R.M., and Harris, R.V., "Use of Grit-Type Boundary-Layer-Transition Trips on Wind Tunnel Models," NASA TN D-3579, Washington, D.C., September 1966.

40) Beutner, T.J, Celik, Z.Z., and Roberts, L., " Determination of Solid/Porous Wall Boundary Conditions from Wind Tunnel Data for Computational Fluid Dynamics Codes," AIAA Paper 93-0530, January, 1993.

41) Beutner, T.J, Celik, Z.Z., and Roberts, L., "Determination of Solid/Porous Wall Boundary Conditions from Wind Tunnel Data for Computational Fluid Dynamics Codes," AGARD CP 535, Paper 16, October, 1993.

42) Rae, W.H., and Pope, A., "Low-Speed Wind Tunnel Testing, Second Edition," John Wiley & Sons, New York, 1984, pp 344-444.